STATISTICAL DOWNSCALING OF METHANE EMISSIONS FROM ABRUPT PERMAFROST THAWING OVER ALASKA

VASUDHA CHATURVEDI
June,2021

SUPERVISORS:
Dr. Frank.B.Osei
Dr. H. Aghababaei

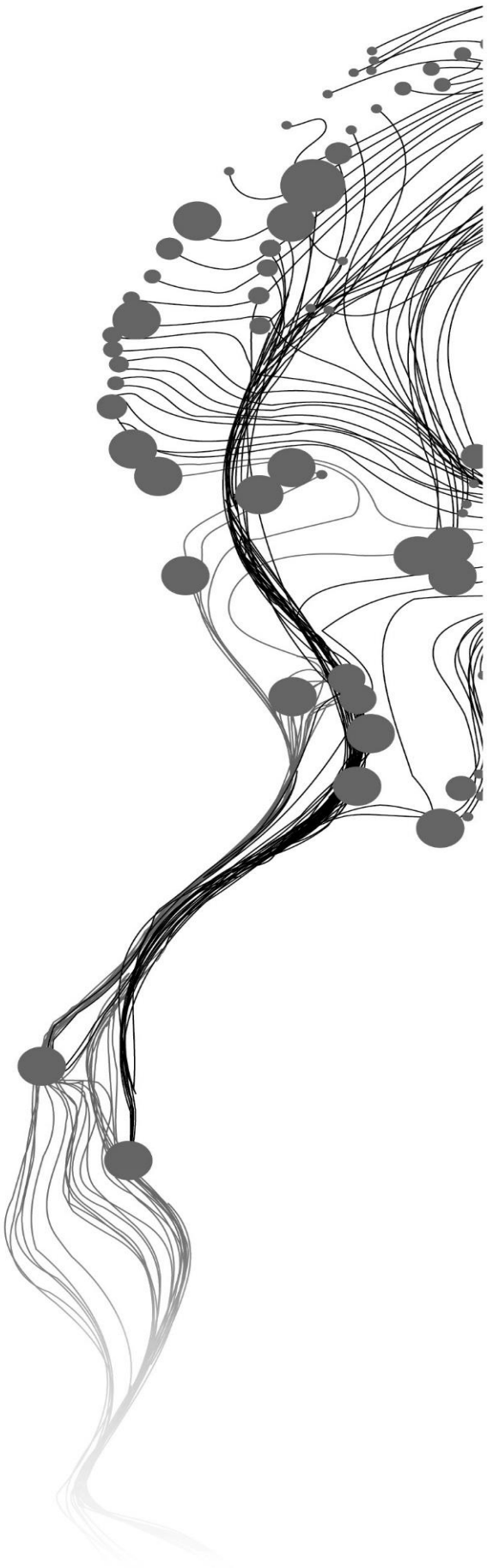

STATISTICAL DOWNSCALING OF METHANE EMISSIONS FROM ABRUPT PERMAFROST THAWING OVER ALASKA

VASUDHA CHATURVEDI
Enschede, The Netherlands, June,2021

Geo-Information Science and Earth Observation of the University of Twente in partial fulfilment of the requirements for the degree of Master of Science in Geo-information Science and Earth Observation.
Specialization: Geoinformatics

SUPERVISORS:
Dr. Frank.B.Osei
Dr. H. Aghababaei

THESIS ASSESSMENT BOARD:
Prof. Dr. Ir. A. Stein(Chair)
Dr V. van Zoest (External Examiner, Uppsala University, Sweden)

DISCLAIMER

This document describes work undertaken as part of a programme of study at the Faculty of Geo-Information Science and Earth Observation of the University of Twente. All views and opinions expressed therein remain the sole responsibility of the author, and do not necessarily represent those of the Faculty.

ABSTRACT

Permafrost regions are areas below the Earth's soil surface that stays permanently frozen for two consecutive years. The permafrost layer is highly rich in organic matter; with global warming and uprising temperatures, there is a severe threat of abrupt permafrost thawing leading to rapid bacterial degradation of organic carbon. As a result, a disproportionate amount of greenhouse gases such as CH_4 and CO_2 are released into the atmosphere. Methane, amongst all greenhouse gases, contributes more to global warming. UNFCCC recognizes various sources of methane emissions causing positive climate feedback, but emissions from abrupt permafrost thawing are the least understood feedback to the warming climate. In order to monitor, understand and record the changing emissions at the regional level, it is essential to obtain fine-resolution data. The development of spaceborne satellite-derived remote sensing methane data brought a rapid increase in homogeneous and global level data. However, these datasets are coarse in resolution limiting the information gained from these images. Therefore, there is a need to downscale these datasets to obtain maximum information and conduct regional-level studies. There is hardly any study on regional level monitoring of methane emissions from abrupt permafrost thawing using TROPOMI S5P downscaled data. Thus, this study firstly aims at recognizing variables contributing to rapid permafrost thawing leading to increased methane emissions. Secondly, comparing and estimate the downscaling technique which gives the best estimates of methane data. Thirdly, to monitor changes over methane emissions using the selected method for downscaling.

The study was conducted in four counties of Alaska, The United States of America. Estimating variables affecting the magnitude of methane emissions were obtained using the AIC index, stepwise regression, correlation coefficient, and multicollinearity. Due to the non-linear and linear relationship between auxiliary variables and dependent variables, various regression models were performed to estimate the model that explains the maximum variance. Three downscaling techniques of RK, ATAK, and ATARK were used for comparison. The three techniques accuracy was evaluated against the coarse resolution dataset using leave-one-out cross-validation (LOOCV) and six indices (mean, SD, variance, MAE, CC, CH). Lastly, to monitor changes in methane emissions, the selected technique is used for downscaling the recorded dataset over the years

The statistical analysis showed MODIS1 LSTDAY, MODIS2 LSTNIGHT, VIIRS NDVI, GMTED 2010 DEM, and VIIRS EVI as the chosen predictors against the TROPOMI S5P methane product as the dependent variable. These predictors showed a weak and statistically significant correlation values. The linear regression model was selected with the lowest RMSE (11.47), MAE (9.04), and highest R squares value (0.29). Amongst the three techniques, ATAK showed a slightly better performance with a CH value of 0.99, 0.99 for tile 17 and 21, and CC value of 0.98,0.99. Monitoring the downscaled images from August 2018-May 2021 did not produce much information about the rate of changes in methane emissions. However, what might be inferred is a spatial shift in methane emissions from South to North to South again which is due to seasonal changes.

ACKNOWLEDGEMENTS

I want to express my sincere appreciation to my supervisors: Dr. Frank.B.Osei, Dr. H. Aghababaei, for their patient guidance and suggestions. Dr. Maogui Hu, Dr. Yong Ge, Dr. Andrew Zammit Mangion, Dr. Eulogio Pardo-Igúzquiz for clearing my doubts and providing helpful information.

Many thanks extended to Prof. Dr. Ir. A. Stein and Drs. J.P.G. Bakx, for their advice during the proposal and mid-term presentation.

Most importantly, my sincere thanks to my friends for their advice and encouragement when I was struggling. Thanks to all the staff and management in ITC. A heartfelt thanks to my parents and pets without your support and encouragement, it would be next to impossible to cope with such tough times and finish my thesis.

TABLE OF CONTENTS

LIST OF FIGURES

LIST OF TABLES

LIST OF ACRONYMS

AIC	Akaike Information Criterion
ATAK	Area to Area Kriging
ATARK	Area to Area Regression Kriging
$C0_2$	Carbon-dioxide
CC	Correlation Coefficient
CH	Coherence Statistics
CH_4	Methane
CK	Cokriging
DEM	Digital Elevation Model
DN	Digital Number
DSCK	Downscaling Cokriging
EOS	Earth Observation system
EPSG	European Petroleum Survey Group
ESM	Earth system Models
EVI	Enhanced Vegetation Index
GCOS	Global Climate Observing System
GHG	Green House Gases
GLS	Generalized Least Squares
GMTED	Global Multi-resolution Terrain Elevation Data
GTN-P	Global Terrestrial Network for Permafrost
IAM	Integrated Assessment Models
IPA	International Permafrost Association
IPCC	Intergovernmental Panel on Climate Change
K	Kelvin
KED	Kriging with External Drift
LiDAR	Light Detection and Ranging
LOOCV	Leave One Out Cross-Validation
LST	Land Surface Temperature
MAE	Mean Absolute Error
MLR	Multiple Linear Regression
MODIS	Moderate Resolution Imaging Spectroradiometer
NASA	National Aeronautics and Space Administration's
NDVI	Normalized Difference Vegetation Index
NGA	National Geospatial-Intelligence Agency
NO_2	Nitrogen dioxide
OK	Ordinary Kriging
OLS	Ordinary Least Squares
PCF	Permafrost Carbon Feedback
PSF	Point Spread Function
QA	Data Quality
QC	Quality Indicator
R2	R squared
RAM	Random Access Memory

RK	Regression Kriging
RMSE	Root Mean Square Error
RS	Remote Sensing
S5P	Sentinel 5 Precursor
SCIAMACHY	Scanning Imaging Absorption Spectrometer for Atmospheric Chartography
SDG	Sustainable Development Goal
SDG	Standard Deviation
SK	Simple Kriging
SMI	Soil Moisture Index
S-NPP	Suomi National Polar-Orbiting Partnership
SWIR	Short Wave Infra Red
TOA	Top of Atmosphere
TROPOMI	TROPOspheric Monitoring Instrument
UAS	Unmanned Aircraft Systems
UNFCCC	United Nations Framework Convention on Climate Change
USGS	United States Geological Survey
UV	Ultra Violet
VIIRS	Visible Infrared Imaging Radiometer Suite
VNP	Vegetation Indices

1. INTRODUCTION

1.1. Background

Permafrost regions are areas below the Earth's soil surface that stays permanently frozen (Canadian Permafrost Association, 2021). Frozen ground is formed when water trapped in soil sediments, fissures, and crevices in rocks on the Earth's surface freezes (Denchak, 2018). Permafrost grounds form when these areas remain permanently frozen for at least two years to hundreds of years (National Snow and Ice Data Center, 2020). If the same ground freezes and thaws yearly or seasonally, it is considered as seasonally frozen ground. These regions take up nearly 9 million square miles of the Northern Hemisphere that include Alaska, Greenland, Siberia, Canada and, other parts of the world such as Tibet, South America, and New Zealand (Denchak, 2018; Yawitz, 2012).

The permafrost layer is highly rich in soil organic carbon matter (National Snow and Ice Data Center, 2020). This is because regions occupied by this layer were green areas with ecosystems flourishing during glacial times. Thousands of years ago, these plants and animals died and got locked in permafrost (Zimov, Schuur, & Chapin, 2006). Due to the presence of ice, their pace of decomposition reduced and resulted in carbon content (Welch, 2019). Study by Tamocai et al., (2009) estimate almost 1700 gigatons of carbon being stored in permafrost. This layer can extend from a few meters to a few km below the Earth's surface (Schaefer et al., 2014).

With global warming and uprising temperatures, there is a severe threat of abrupt thawing of permafrost regions, such as Alaska, Russia, and Canada (Jorgenson, Shur, & Pullman, 2006). Researches show a 10 percent less frozen ground than in the 1900s (Denchak, 2018). Higher temperatures lead to faster thawing of permafrost, making the organic carbon available for rapid bacterial degradation (González-Eguino, & Neumann, 2016). As a result, a disproportionate amount of methane (CH_4) and carbon dioxide (CO_2) is released into the atmosphere (Natali et al., 2021). These emissions do not take place over a continuous region. When permafrost thaws, the ground below subsidies and forms lakes structures called thermokarst lakes and thaw ponds. These emissions seep through pockets from the bottom of these lakes (Walter et al., 2006). The amount of these gases released depends upon the topographic condition, temperature, and organic matter present at the site (Kohnert et al., 2017). Emissions of these gases (CH_4 and CO_2) in small fractions result in positive carbon feedback from permafrost, affecting future climate (Schuur et al., 2008).

Amongst all greenhouse gases, methane has influenced 20% of global warming since pre-industrial times (Kirschke et al., 2013). Methane has 25 times higher potential than carbon dioxide in a changing climate and 80 times more potent in trapping heat (Yvon-Durocher et al., 2014). Therefore estimation of methane is inevitable to combat climate change. Estimation of methane changes requires combining various information such as air and soil temperature, soil moisture, vegetation, organic matter content and, permafrost thickness in permafrost rich regions (Christensen et al., 1995; Qingbai, & Yongzhi, 2004; Xue et al., 2009; Olefeldt et al., 2013; Gido et al., 2019).

1.2. Justification

Climate change is considered one of the biggest threats to humankind. In order to combat the issue after the Rio Earth Summit in 1992, United Nations Framework Convention on Climate Change (UNFCCC) was adopted that seeks to stabilize greenhouse gases (GHG's) emission (Katila et al., 2019). Another initiative

taken by UNFCCC was to maintain the global average temperature rise below 1.5 to 2 degrees Celsius as per the Paris agreement 2015 (UNFCCC, 2021a). Similarly, Sustainable Development Goal (SDG) 13.2, 13.3, and 13.b aim at reducing further warming of the climate by integrating policies, spreading awareness, adapting mechanisms at the national and global level (Katila et al., 2019). Despite multiple effort, the average global temperature tends to rise. Numerous sources of methane emissions causing positive climate feedbacks are recognized so far, such as plant biomass, extracting of fossil fuels, agriculture, and natural emissions. But there is still no clear research and documentation that the thawing of permafrost contributes significantly to the current carbon global budget (UNFCCC, 2021b; Sabine et al., 2014). As per Natali et al., (2021) permafrost carbon feedbacks are not yet accounted in the Earth system models (ESMs) and integrated assessment models (IAMs).

Permafrost carbon-climate feedback is one of the most important and least understood atmospheres feedback of warming climate (Pachauri et al., 2014). Therefore, it is of utmost importance to monitor abrupt permafrost thawing to study changes in methane emissions. Analyzing temporal changes of CH_4 emissions will help understand its contribution to climate feedback and assessing the impacts of climate change on growing emissions (Olefeldt et al., 2013). Monitoring changes in the emissions can help plan additional efforts to minimize abrupt thawing, which will help reduce global warming even more (Isaksen et al., 2014; Zhang et al., 2017)

1.3. Research problem

In order to estimate varying spatial and temporal scales of methane emissions, ground techniques such as the static chamber, bubble trap, soil characteristics have been utilized (Christensen, 2004; Wei et al., 2018). Airborne techniques, for example, Unmanned aircraft systems (UAS) and spaceborne using coarse resolution images, have been used (Christensen, 2004). But the techniques using ground-based and airborne data are cost-inefficient, labor-intensive, have limited sampling frequency, large scale, and time-consuming (Reuder et al., 2012; Olefeldt et al., 2013; Oberle et al., 2019). The development of satellite-derived remote sensing (RS) data has reduced these limitations (Guo et al., 2015; Jin et al., 2018). Over the last few decades, there has been a rapid increase in the number of images taken through satellites (Atkinson, 2013; Guo et al., 2015). Remote sensing satellites provides homogeneous and global coverage data (Frankenberg et al., 2005). These data, such as Moderate Resolution Imaging Spectroradiometer (MODIS), are freely available, provide near real-time and daily frequency coverage for global monitoring (Wang et al., 2015). Hence, this study focuses on spaceborne satellite-derived methane data to detect and monitor methane emissions at the local level for a small-scale study. However, the issue faced with this data is its coarse spatial resolution, limiting the information gained from these images (Atkinson, 2013; Jin et al., 2018). Therefore, growing research to downscale (greater detail) such images to attain maximum information (Atkinson, 2013; Wang et al., 2015).

There are various interpolation techniques to obtain fine resolution images from coarse resolution, but spatial dependency is often ignored in most interpolation techniques (Piazza et al., 2015; Kumari et al., 2017). Thus, geostatistical approaches were introduced, which accounts for spatial variability and spatial autocorrelation in data (Zhang, Li, & Travis, 2007). The process of statistical downscaling using geostatistical techniques refers to obtaining fine resolution images from coarse resolution using the geostatistical interpolation technique (Rasmus, & Chen, 2008; Wolf et al., 2017). So far, studies have been conducted using this technique to estimate methane emissions from livestock, agriculture and interpolating missing data (van der Gon et al., 2000; Zhang et al., 2012). However, this method has not been proven to identify hotspots and track changes in methane emissions induced by permafrost thawing.

2. RESEARCH OBJECTIVES/RESEARCH QUESTIONS

2.1. General Objective

The main objective of this study is to determine which statistical downscaling technique best estimates TROPOspheric Monitoring Instrument (TROPOMI) methane data, which is then used to monitor changes over methane emissions. These objectives are met by first selecting which environment variables affect the pace of thawing. Second, evaluate the results of downscaled images using different downscaling interpolation techniques. Thirdly, generating temporal maps using the selected method for recording the changes in methane emissions.

2.2. Sub Objectives

1. Evaluate different factors driving the magnitude of methane emissions from abrupt permafrost thawing.
2. Identify which spatial downscaling technique is suitable for local analysis of methane emissions assuming a non-stationary mean.
3. Assess and monitor the changes in methane emissions at the local level.

2.3. Research questions

1. What factors affect methane emissions change due to abrupt permafrost thawing through literature review and statistical relationships?
2. Which among the three statistical downscaling techniques (RK, ATAK, ATARK) is suitable for depicting methane emissions at the local level for small-scale study?
3. What is the temporal variation in the magnitude of methane emissions?

3. LITERATURE REVIEW

Methane emissions over permafrost locations have been observed using a variety of approaches, including ground-based, airborne, and space-borne technologies in different studies. The 1995 report of the Intergovernmental Panel on Climate Change (IPCC) addressed concerns regarding emissions over China, Alaska, Russia, and Canada (Yawitz, 2012). Concerns regarding these emissions led to establishing the Global Terrestrial Network for Permafrost (GTN-P), a borehole monitoring system. It was created under the Global Climate Observing System (GCOS) and the Global Terrestrial Observation System (GTOS) with the assistance of the International Permafrost Association (IPA) (Romanovsky et al., 2002). This system uses boreholes measurements at numerous international sites to measure permafrost temperature and thickness, identified as crucial variables for emissions (Romanovsky et al., 2002). The closed chamber ground technique (Bubier et al., 1995), floating bubble traps over lakes (Walter et al., 2006), and soil techniques (Wei et al., 2018) are few examples of the ground-based technique. These observations are real-time observations, ground verified, and thus they do not require validation. However, the disadvantages of these techniques are the coverage is sparse, time-intensive, and a larger workforce is required. These techniques use site-specified observation, have measurement bias, and are cost-inefficient (Kohnert et al., 2017; Oberle et al., 2019).

Airborne techniques such as aerial photographs, Unmanned Aerial Systems (UAS), and Light Detection and Ranging (LiDAR) are well suited for local coverage for methane emissions (Christensen, 2004; Rashid et al., 2020; Elder et al., 2020). They are more accurate in predicting methane emissions near-surface than satellite-derived data (Thorpe et al., 2013). However, they are not cost-effective for small-scale studies since they have a high cost per unit area coverage overground. In addition, they are unable to cover vast areas because of their narrow swath width. Airplane-based measurements can be carried at a height of approximately 100 meters (Oberle et al., 2019). Analyzing small study areas requires many flight plans, limited spatial coverage, flight time, aviation policy, and cost constraint (Reuder et al., 2012; Villa et al., 2016).

Techniques using satellite-derived data are beneficial when a large area is used for the study (Takeuchi et al., 2003; Turner et al., 2016). They provide precise and accurate information for the observations of methane emissions (Schneising et al., 2011). Over the last few decades, the growing number of images taken by remote sensors has reduced the spatial extent and provided complete global coverage. However, these satellite-derived data are coarser in resolution and obstruct extracting maximum information from satellite images. With the aim to maximize the information derived from satellite data providing global coverage drove many researches (Wang et al., 2015). The downscaling technique was introduced to overcome this barrier (Atkinson, & Tate, 2000). Downscaling/scaling down refers to increasing the spatial resolution of coarse imagery (Atkinson, 2013). Downscaling images using interpolation is a growing technique to produce fine resolution images from coarse resolution (Kyriakidis, & Yoo, 2005; Zhang et al., 2012).

Downscaling of images can be done through a deterministic or geostatistical interpolation approach (Piazza et al., 2015). A deterministic interpolation approach such as bilinear interpolation and inverse distance weighting is inappropriate for local interpolation as the kernel size for interpolation uses infinite size (Chen, & Wang, 2010). These interpolation techniques make predictions without accounting for uncertainty related to the data. It does not account for spatial dependency concerning spectral information required for an accurate image interpolation (Kumari et al., 2017). Understanding spatial variability is necessary as the digital number (DN) value varies across satellite images (Rossi et al., 1994; Zhang et al., 2012).

In comparison, geostatistical approaches account for spatial variability and spatial autocorrelation in data. Kriging is a geostatistical spatial statistics technique that accounts for spatial dependence while estimating values at unsampled locations and assigns confidence and probability of uncertainty to predicted. The technique ensures minimum-error variance and follows the law of spatial correlation that places closer to each other are more similar than distant locations (Zhang et al., 2007). Furthermore, geostatistical approaches of image fusion for downscaling satellite images are progressively used as they retain the spectral property of the coarse resolution image (Wang et al., 2015). Image fusion is a spatio-spectral technique to combine fine spatial resolution images with a coarse resolution to produce a fine spatial resolution image (Atkinson et al., 2008; Zhang et al., 2012; Wang et al., 2015). There are two ways of downscaling based on data availability: first using ground-based measurements and second without ground-based measurements using spatial correlation information through fine-scale auxiliary variables (Park, 2013).

Geostatistical methods are grouped into: univariate when the primary data is adequate for predictions and multivariate when covariates contribute to model the dependent variable (Zarei, Masihi, & Salahshoor, 2011). The univariate approach tends to smooth predictions and cannot produce accurate interpolated results of the variable such as Ordinary Kriging (OK) and Simple Kriging (SK). Thus, multiple regression kriging approaches (considering one or more variables) using methods such as regression kriging (RK), kriging with external drift (KED), (ATAK) area to area kriging and, (ATARK) area to area regression kriging were established (Rata et al., 2020).

However, there are advantages and limitations to these techniques. Cokriging (CK) gives an unbiased predictor, minimizes variance, incorporates sparse data, but it does not consider spatial variability of pixel sizes (Memarsadeghi et al., 2005; Pardo-Igúzquiza et al., 2006). Thus, a sturdier method of Downscaling Cokriging (DSCK) was proposed. It is a one-step approach, like CK it is unbiased and minimizes prediction variance. Also, it accounts for pixel sizes, cross-correlation, correlation, and point spread function (PSF). However, it requires complex modeling of auto-semi-variogram and cross-semi-variogram, making it challenging to automate (Pardo-Igúzquiza et al., 2006; Atkinson et al., 2008; Wang et al., 2015). KED is another technique easy to implement than CK as it requires estimating a direct variogram and is easily operational (Ribeiro Sales, Souza, & Kyriakidis, 2013). On the other hand, KED is computationally intensive, calculates weights for each pixel, and most importantly, it assumes PSF is constant along with all the bands/images, covariate vary smoothly across space (Hengl et al., 2003; Ribeiro Sales et al., 2013; Wang et al., 2015; Wang, Shi, & Atkinson, 2016).

RK uses regression on additional variables for prediction and kriging on residuals using the regression model (Hengl et al., 2007). ATAK is used more for areal data as it considers the size of the covariates data to predict the variable as area (Kyriakidis, 2004; Kyriakidis, & Yoo, 2005). But RK, despite its advantages, is insufficient for downscaling as it cannot reproduce the spectral properties of coarse data and assumes the residuals are uncorrelated and independent spatially. Whereas residuals should not be discarded when regression analysis fails to produce sufficient information on prediction patterns (Park, 2013). As for ATAK, if applied alone, it cannot restore high-frequency values present in the fine resolution image. Thus, a new approach called area to area regression kriging (ATARK) was formed, which utilizes the benefits of RK and ATAK (Wang et al., 2015). The advantage of ATARK is its ability to preserve coherence property, meaning the fine-scale predictions are identical to the original data value when upscaled. It accounts for spatial correlation of residuals (Park, 2013; Wang et al., 2015). But these conclusions are made based on their study of work, they will be tested for this research.

4. MATERIALS

4.1. Study Area

Alaska occupies the northwestern part of North America with a geographic center at 63°50' N 152°00' W. Alaska is divided into 30 counties consisting of 18 organized boroughs and one unorganized borough divided into 11 census areas (Alaskan Municipal League, 2021). It has an elevation of 0 to 20,320 feet from sea level (Eastern Region Geography, 2005) and a geographical extent of 375 million acres (Hull, & Leask, 2007). The mean annual precipitation ranges from 200 – 5000 mm (Northwest Alliance for Computational Science and Engineering, 2021) and average temperatures of 31.5 degrees Fahrenheit (F) with higher averages of 39.5 and lower averages of 23.5 F (Weatherbase, 2021). Alaska has more than 5,000 glaciers, over 3,000 rivers, 3 million lakes, and two of the largest national forest, each covering about 16.8 million and 4.8 million acres (Fairbanks, 2004). Most of the Alaskan region lies above permafrost, consisting of 29% of continuous permafrost, 35% discontinuous permafrost, 8% sporadic permafrost, and 8% isolated permafrost (Yoshikawa et al., 2008). The dominant soil type in the region is Tanana, a poorly drained soil type if left untilled and contains permafrost near the surface. This soil is present on alluvial land types and supports the plant community of aspen, spruce (Rieger, Schoephorster, & Furbush, 1979; USDA Natural Resources Conservation Service, 2021). The study area consists of four counties/ boroughs within Alaska named Fairbanks north star, southeast Fairbanks, parts of Yukon-Koyukuk, and Denali, stretching over approximately 493,059 km^2 area (National Association of Counties, 2013). The study area as shown in Figure 1 was chosen due to the following reasons:

- The study area lies under three different extents of permafrost, namely continuous, discontinuous and sporadic.
- Presence of peats, bogs, fens, pingos, and thermokarst formation that emerged as a result of rapid permafrost thawing.
- A vast area had to be investigated in order to examine how to account for non-stationarity in the study area, which is expected to reveal non-stationary circumstances (Meul, & Van Meirvenne, 2003).

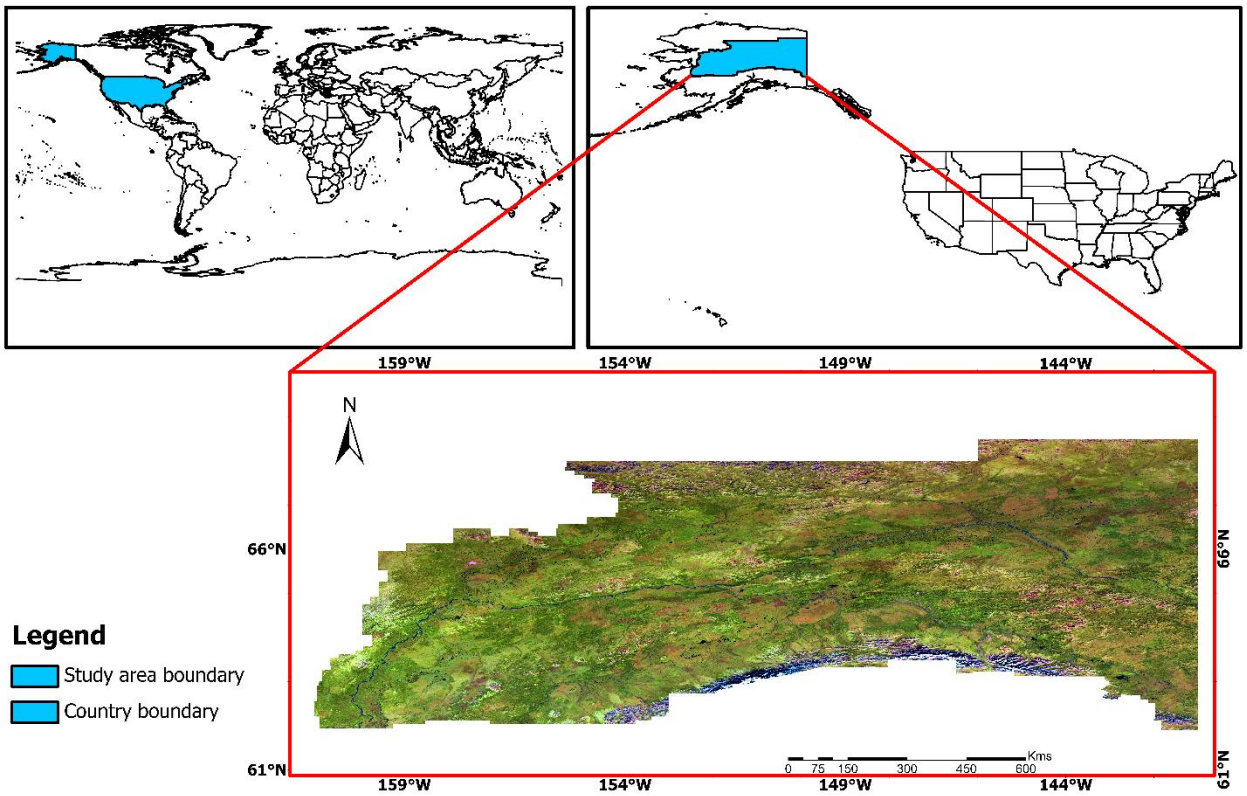

Figure 1: Study area map
Source: Google Earth Engine open source Landsat8 (500 m)

4.2. Spatial data products and description

The following subsections describe the data products used before carrying out the analysis. The list of data is shown in *Appendix 1*.

A. Dependent variable-

1. **Sentinel 5 precursor (S5P) Tropospheric Monitoring Instrument TROPOMI Level 2 CH_4** - TROPOMI level 2 data product of CH_4 total column was used for this study. This instrument is a spaceborne, nadir-viewing, imaging spectrometer covering wavelength bands between the ultraviolet and the shortwave infrared. This single payload instrument of the Sentinel-5P (S5P) spacecraft uses passive remote sensing techniques to attain its objective of three environmental themes: Air Quality, Stratospheric Ozone Layer, Climate Change Monitoring, and Forecasting (Landgraf et al., 2021). It uses Top of Atmosphere (TOA), the solar radiation reflected and radiated from the Earth to address the environmental issues. The instrument operates in a push-broom manner with a swath width of ~2600 km of the Earth's surface. The typical pixel size, which is near nadir, was 7 * 3.5 km^2 for all spectral bands till 6th August 2019, after which the flight direction remained 3.5 km^2, but the perpendicular direction of nadir reduced to 5.5 km^2 except for the UV1 band (7 * 28 km^2) and SWIR bands (7 * 7 km^2) (Landgraf et al., 2021; Apituley et al., 2021). It has a revisit time of less than one day, a global spatial coverage, and data available starting from April 2018 (Landgraf et al., 2021). S5P methane product was downloaded via sentinel hub requests using API https://apps.sentinel-hub.com/requests-builder/. A large portion of the study area does not have any pixel recording due to clouds. This dataset is suitable for clear sky scenes, and the cloudy scenes are pre-filtered (cloud fraction higher than 0.02) to reduce the processing time. Where there are no emissions, the data is retrieved with no values, but the

lifetime of CH_4 in the atmosphere is 12 years, so there is no zero-density of methane as this dataset is concentrations of CH_4 along the complete column of air which is different from surface mixing ratio.

B. Auxiliary variables to be used as a covariate-

1. **Normalized Difference Vegetation Index (NDVI) and Enhanced Vegetation Index (EVI) (auxiliary variable) -** The Suomi National Polar-Orbiting Partnership (S-NPP) National Aeronautics and Space Administration's (NASA) Visible Infrared Imaging Radiometer Suite (VIIRS) Vegetation Indices (VNP13A1) was designed to continue the Earth Observation system Mission (EOS) after Moderate Resolution Imaging Spectroradiometer (MODIS) Terra and Aqua Vegetation Indices. It was launched on 28th October 2011 as a continuation EOS satellite to extend the data records and is playing a vital role in supporting the monitoring, detection, quantification of global land vegetation properties and their change over time and space. The VNP13 has a temporal resolution of 16 days, a spatial resolution of 500 meters and provides the vegetation indices by selecting the best available pixel on a 16-day basis. It has three vegetation indices: (1) Normalized Difference Vegetation Index (NDVI), (2) the Enhanced Vegetation Index (EVI), and (3) Enhanced Vegetation Index-2 (EVI2) (Didan et al., 2018). NDVI and EVI1 were selected from the period after April 2018, which needs to be consistent with TROPOMI methane data. The dataset was obtained using Google Earth Engine https://code.earthengine.google.com/.

2. **Land Surface Temperature (LST) DAY (auxiliary variable) -** The MOD11A1 V6 is a daily level 3 composite dataset for land surface temperature acquired by the NASA EOS. It has a resolution of 1000 meters developed to monitor changes and trends in surface temperature. It is gridded in the Integerized Sinusoidal projection (in V3) or the Sinusoidal projection (in V4). A tile contains grids with 1200 rows and 1200 columns. As latitude increases beyond 30 degrees, the LST value at some grids is the average value of LSTs retrieved from multiple MODIS observations at day and night during clear-sky conditions (Wan, 2013). LST_Day_1km from MOD11A1 was used in the study. This dataset was used after April 2018 for the similar mentioned above and was downloaded using Google Earth Engine https://code.earthengine.google.com/.

3. **Land Surface Temperature (LST) NIGHT (auxiliary variable) -** The MOD11A2 V6 product is an 8-day average dataset for land surface temperature (LST) of spatial resolution of 1000 m. It covers 1200 * 1200 km in a grid. Each pixel value in MOD11A2 is an average of all the corresponding MOD11A1 LST pixels collected over 8 days. Along with both the day- and night-time surface temperature bands, their quality indicator (QC) layers are also provided with this dataset (Wan, 2013). LST_Night_1km dataset was used from this product for the period after April 2018 for parallel reasons, as discussed above. The product was downloaded using Google Earth Engine https://code.earthengine.google.com/.

4. **Digital Elevation Model (DEM) (auxiliary variable) -** The Global Multi-resolution Terrain Elevation Data (GMTED) 2010 was developed by a collaboration of the National Geospatial-Intelligence Agency (NGA) and the U.S. Geological Survey (USGS) for global topographic elevation at three different horizontal resolutions of 1000, 500, and 250 m for the entire Earth. It is designed to support various climatological, hydrological, military, and geomorphological applications at regional, continental, and global scale levels (Danielson, & Gesch, 2011). This dataset was downloaded using Google Earth Engine https://code.earthengine.google.com/.

5. RESEARCH METHODOLOGY

5.1. Research design

This chapter summarizes the methodology used for this study, as shown in Figure 2. With the aim to understand the influence of abrupt permafrost thawing on methane emissions and the importance of permafrost carbon feedback (PCF) as a contributor to warmer temperatures, satellite-derived methane data was used. This dataset is of coarse resolution. Thus, geostatistical interpolation techniques were used for downscaling to fine resolution. Permafrost thawing leads to land surface features such as thaw ponds and lakes which are hotspots for carbon emissions. The size of these lakes can vary from few meters to thousands of meters. In my study, I considered a downscale resolution of 500 m because of two reasons. Firstly, the recorded data shows that small and shallow ponds have a higher potential to release methane emissions (Wik et al., 2016; Serikova et al., 2019). Secondly, the finest resolution present among the covariates was 500 m (Park, 2013). For my study, techniques such as Regression kriging (RK), Area to area kriging (ATAK) and, Area to area regression kriging (ATARK) (Park, 2013; Mukherjee, Joshi, & Garg, 2015; Wang et al., 2015; Wang, Shi, & Atkinson, 2016; Hu, & Huang, 2020) were chosen.

The methodology followed to complete the study includes four sections:

1. Data collection and preparation,
2. Variable selection,
3. Technique selection
4. Monitoring changing trends in methane emissions.

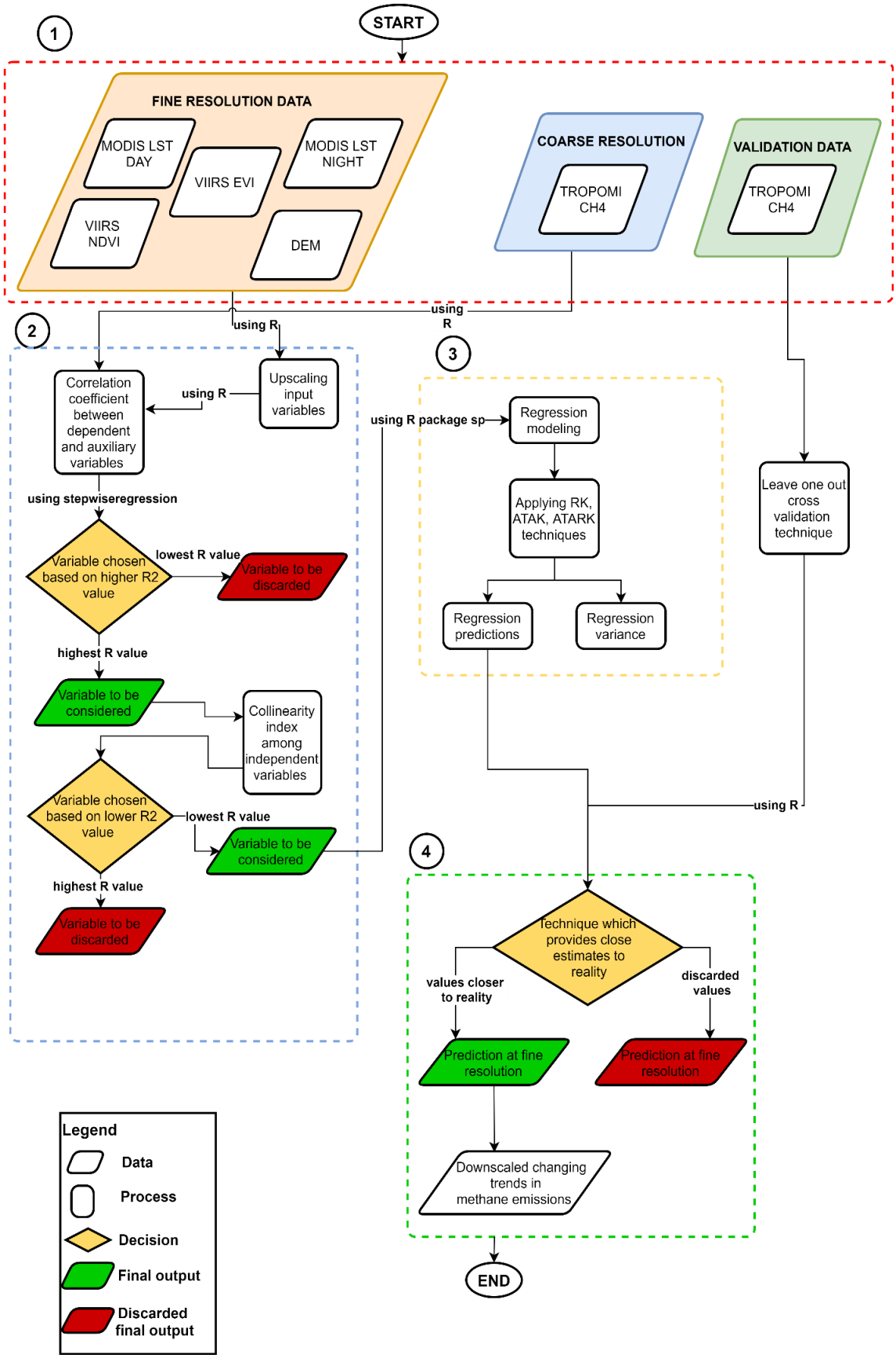

Figure 2: Flow chart of the research method

5.2. Data pre-processing

The study area consists of four counties covering 500078 km². For each dataset, the extent was clipped to the study area boundary with a projection of (EPSG:3857). Methane emissions are not recorded for the complete study area but varying parts on a monthly basis. Thus, overlapping grids of 2000 m were created to solve the following issues:

- Rather than considering the entire research region, constructing grids and picking specific grids where emissions are recorded can help evaluate those places with methane emissions. It will help remove the areas where there is no recording which might lead to higher variance.
- To reduce the issue of a large dataset which would cause problems during computation of inverting the covariance matrix.
- To maintain the continuity of interpolated downscaled emissions and to capture local heterogeneity of emissions.

All covariates were resampled to 500 m resolution, which is the pixel resolution decided for downscaled images. Next, the covariates and methane emissions were clipped according to the grid size. Each grid covered an area of 257 by 323 km². Thus, for methane data, the pixel count was 47 * 75 and for covariates was 650 * 520.

5.2.1. Pre-processing of the response variable

S5P is flagged with quality values for all the bands with minimum data quality (QA), which refers to minimum (min) pixel quality to be displayed in percent. Every band except for nitrogen oxide (NO_2) has a min QA of 50, and for NO_2 it is 75. Since this research required monthly averages, the daily data and min QA of 50 percent were downloaded for the months showing emissions (Landgraf et al., 2021). The drawback of using min QA is the number of pixels showing monthly average methane emissions reduced within the study area, which initially had a large number of pixels, but those are the pixels with poor recorded quality.

5.2.2. Pre-processing of covariates (NDVI and EVI)

The 16 days NDVI_VIIRS dataset was converted to a monthly mean average. Vegetation values between -1.0 to 1.0 with a scale factor of 0.0001 were derived, and a shapefile of the study area was used to provide the extent for extracting the area of interest. Similarly, a scale factor of 0.0001 was also used for EVI.

5.2.3. Pre-processing of covariates (LST DAY and LST NIGHT)

MODIS provides daily datasets which were converted to mean monthly averages, multiplied with a scale factor of 0.02. Temperatures are recorded in Kelvin, which was converted to Celsius by subtracting 273.15, and same shapefile as in the case of NDVI was used to define the extent of these datasets.

5.2.4. Pre-processing of covariates (DEM)

The elevation data used for this study was obtained from GMTED 2010. The elevation values range from -100 to 6500 m, using the shapefile of the boundary extent the study area was clipped.

5.3. Data exploration

The quantitative and descriptive analysis was done using graphs such as histograms and scatterplots. Histograms were used to understand the nature of the datasets, and scatterplots were used to understand the relationship of the response variable and auxiliary variables.

5.4. Data Analysis

As shown in Figure 2, the methodology chart summarizes the flow of ideas followed for the research. After downloading and pre-processing of data, the next step was to attain the three objectives, which are as follows:

5.4.1. Covariate selection

Methane emissions are influenced not by a single variable/factor rather by many complex physical, chemical, and biological factors (Whalen, & Reeburgh, 1992; Christensen et al., 1995). In this study, various environmental land surface factors were considered to find the key factors that influence the spatial variations in methane emissions. The covariate selection analysis using Pearson's correlation coefficient (CC) and Akaike information criterion (AIC) using stepwise regression both backward elimination and forward selection was implemented to improve the model selection. This method helps to assess the importance (strength of a linear or non-linear relationship) of all predictors to explain the dependent variable. It iteratively adds and removes the variable from the regression model until it finds the best fits and approximates. A total of 22 variables consisting of 51 datasets were downloaded for the purpose of covariate selection to improve the predictions. All the datasets were resampled to the resolution of the dependent variable using bilinear interpolation followed by the stepwise regression analysis (Hutmacher, & Kowalski, 2015; Ezzine et al., 2017). Lower values of AIC and root mean square error (RMSE), higher values of CC, R-squared (R^2), and adjusted R^2 were considered for the selection. There was no threshold value set for CC because the correlation values were rather very low.

5.4.2. Multicollinearity

Multicollinearity is a problem that occurs when two or more covariates chosen for prediction are highly associated with one another. If the covariates are highly correlated, it results in a greater standard error of the coefficients (Ezzine et al., 2017; Daoud, 2018). This study considered more than one variable to be used as covariates, so the issue of correlation among predictors is undesired and needed to be excluded. All the variables were tested for the issue of multicollinearity using Spearman's rank correlation coefficient method. Spearman method was used as it ranks the variables based on their measure of association and is beneficial for cases where either one of the variable is skewed (Mukaka, 2012). The correlation was calculated between each pair of variables with all complete pair of variables.

5.4.3. Downscaling using kriging

Interpolation methods based on geostatistics have a considerable advantage in terms of retaining the coarse image spectral features. This indicates that when downscaling a fine-scale image to a coarse image, the result should be similar to the original (Wang, Shi, & Atkinson, 2016). For this study, three geostatistical interpolation techniques of RK, ATAK, and ATARK were compared to estimate which technique predicts better-estimated values for downscaled methane emissions.

5.4.3.1. Regression kriging

Regression kriging (RK) is a hybrid non-stationery geostatistical interpolation technique (Hengl et al., 2003). It uses regression on auxiliary variables, and then simple kriging with known mean is performed to interpolate the residuals from the regression *Equation 1*. The drift and residuals can also be fitted separately and then summed up. RK combines the two approaches: regression which builds the relationship between the target and auxiliary variables at sample location and applying simple kriging to unknown locations with known mean to fit the residuals for unexplained variation (Odeh, McBratney, & Chittleborough, 1995; Hengl et al., 2007).

$$\hat{Z}_0^{RK} = \sum_{p=0}^{P} \hat{\beta}_p x_{0p} + \sum_{i=1}^{K} \lambda_{0i} e_i \; ; \qquad x_{00} = 1, \tag{1}$$

Equation 1: Equation for regression kriging.

Where:

- $\hat{Z}_0^{RK}$ are predictions at new locations,
- $\hat{\beta}_k$ are the drift model coefficients and the auxiliary variables x_k are measured at the same locations and all-new locations,
- λ_{0i} are weights determined by semivariance function and,
- e_i are the regression residuals.

The estimation of regression coefficients is done using ordinary least squares (OLS), the covariance function is derived from OLS residuals since a single iteration results are not different from several iterations using generalized least squares (GLS) (Kitanidis, 1993; Hengl et al., 2003; Hengl et al., 2007).

5.4.3.2. Area to area kriging

Inclusion of spatial support and weight function to centroid-based ordinary kriging modifies it to area-to-area kriging (ATAK) *Equation 2*. It is beneficial in situations where geographical units have different shapes and sizes. This approach accounts for the variability within geographical units and preserving the coherence property of predictions, so when averaged is equal to original areal data. In ATAK, the prediction and measurement supports are blocks rather than points. The block-to-block semivariogram is used for computing weights which are estimated using point support semivariogram. The deconvolution helps to estimate the optimal point-support semivariogram that minimizes the difference between the coarse-scale semivariogram and regularized semivariogram. Thus the kriging weights are calculated, and fine-scale predictions are performed (Goovaerts, 2008; Park, 2013; Kwak, Park, & Kyriakidis, 2018)

$$\hat{Z}_0^{ATAK} = \sum_{i=1}^{L(n)} \lambda_{0i} Z_i \tag{2}$$

Equation 2: Equation for area-to-area kriging.

Where:

- Z_i denotes the ith coarse-scale block,
- $\hat{Z}_0^{ATAK}$ denotes ATAK predictions at fine-scale locations within the coarse-scale block by a weighted linear combination of neighboring coarse-scale pixels,
- λ_{0i} are the simple kriging weights assigned to neighboring coarse-scale pixels at an estimation location, the vector of kriging weights are computed using semivariogram deconvolution for point-support semivariance,
- $L(n)$ denotes the number of neighboring blocks closest to the estimation location.

5.4.3.3. Area to area regression kriging

ATARK can be seen as an extension of regression kriging and Area to area kriging (*Equation 3* and Figure 3) (Wang et al., 2015). ATARK models the trend in the dependent variable by regression modeling on auxiliary variables *Equation 4 and 7*. The coarse resolution residuals from regression analysis *Equation 5* are downscaled to fine-scale through ATAK *Equation 6,* then these fine-scale residuals are added back to fine-scale regression predictions *Equation 8* (Wang et al., 2015; Wang et al., 2016). The model accounts for irregular geographical units, spatial correlation, size of support/supports, point spread function (PSF). It can perfectly preserve the spectral properties of the coarse resolution image, and the size of the matrices is much smaller. It uses semivariogram deconvolution to predict variables from areal support to areas and parameterize the kriging prediction (Wang et al., 2015; Wang, Shi, & Atkinson, 2016).

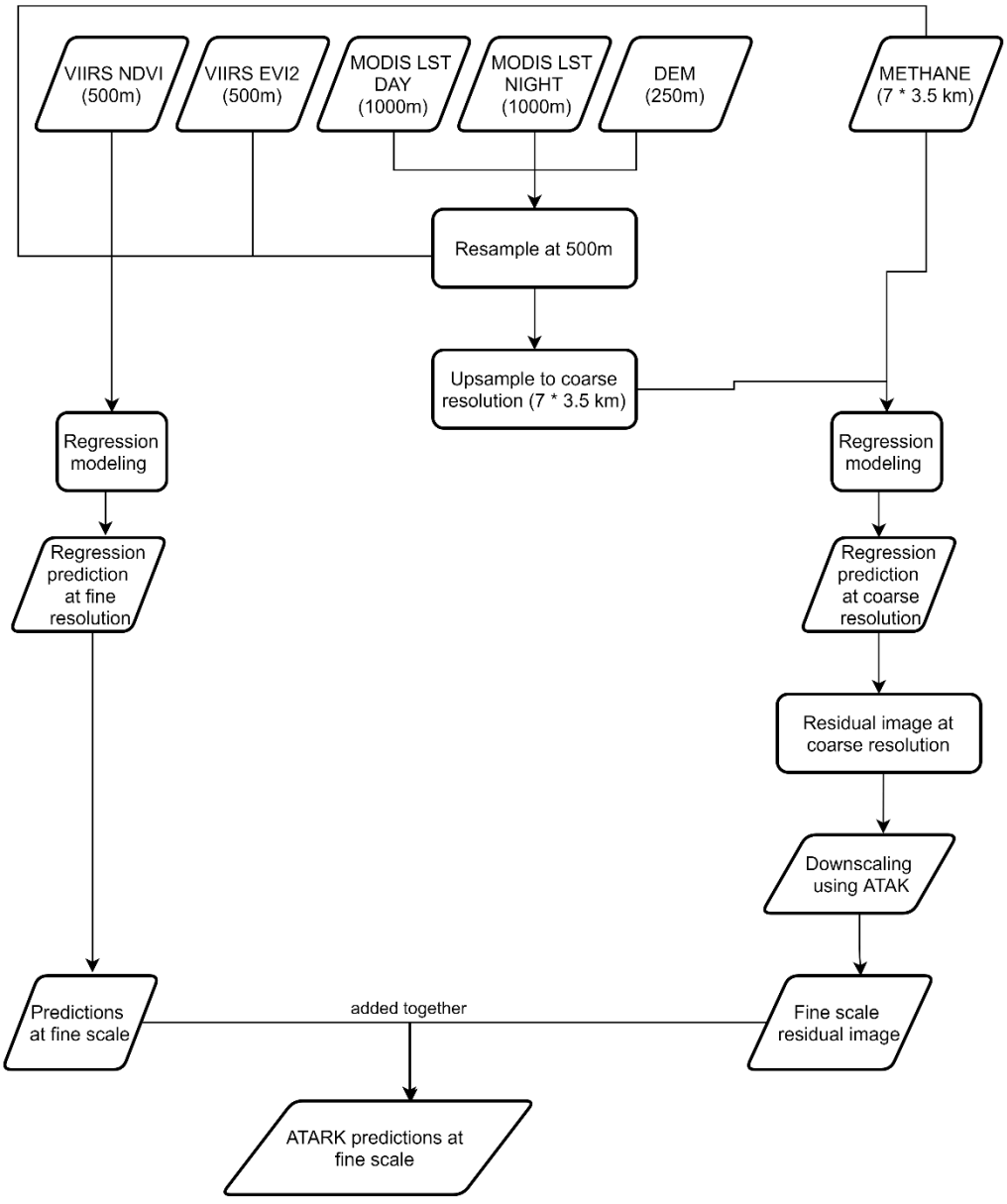

Figure 3: Area to area regression kriging simplified flow chart (Wang et al., 2015).

$$\hat{Z}_0^{ATARK} = \hat{Z}_0^{RK} + \hat{Z}_0^{ATAK} \quad \textbf{(3)}$$

Equation 3: Equation for Area-to-area regression kriging.

Where:

- $\hat{Z}_0^{ATARK}$ denotes ATARK predictions for all fine pixels in coarse data,
- $\hat{Z}_0^{RK}$ are the predictions from regression and $\hat{Z}_0^{ATAK}$ is the ATAK part of the model, which is used for downscaling coarse-scale residuals to fine-scale,
- The relationship between covariates and the dependent variable is built using a multiple linear regression model (MLR). This relationship is assumed to be universal at different spatial resolutions and can be applied at both coarser and finer resolutions (Gao, Kustas, & Anderson, 2012; Wang et al., 2015).

The relationship between fine auxiliary data and coarse data is modeled by multiple linear regression for the first part of the ATARK approach, and it is calculated as:

$$\hat{Z}_i^{RK(C)} = \sum_{p=0}^{P} \hat{\beta}_p x_{ip} + \sum_{i=1}^{K} \lambda_i e_i ; \qquad x_{00} = 1, \quad \textbf{(4)}$$

Equation 4: Coarse-scale regression prediction by upscaling fine-scale covariates.

Where:

- $\hat{Z}_i^{RK(C)}$ is the coarse-scale regression prediction given p group of covariates and x_{ik} are the covariates which are upscaled to the same resolution as coarse image,
- $\hat{\beta}_k$ are the coefficients which are estimated from the regression model between methane and the covariates,
- λ_i are the weights and e_i are the regression residuals,
- The coefficient is estimated using ordinary least squares (OLS) as coefficients derived from OLS by a single iteration are not different from the one derived using generalized least squares (GLS), which is an iterative process (Kitanidis, 1993b). The regression part takes advantage of the final spatial textural information from independent variables.

The coarse-scale residuals are derived by subtracting the coarse-scale predicted image with coarse-scale data. If the regression prediction is perfect, there should be no bias between the predictions and coarse-scale data (Wang et al., 2015). It is calculated as:

$$\hat{Z}_i^{RK(resi)(C)} = Z_i^{(C)} \quad \hat{Z}_i^{(C)} \quad \textbf{(5)}$$

Equation 5: Coarse-scale residual calculation.

Where:

- $\hat{Z}_i^{RK(resi)(C)}$ is denoted as coarse-scale residuals,
- $\hat{Z}_i^{RK(C)}$ is the coarse-scale regression prediction obtained using multiple linear regression model from *Equation 4,*
- $Z_i^{(C)}$ is the observed coarse-scale data.

The regression model is insufficient to reproduce the spectral properties of the coarse-scale data; thus, it cannot be directly used for downscaling. Based on the assumption that residuals are intrinsically stationary, ATAK is used in the second phase of ATARK to downscale coarse-scale residuals from *Equation 5* (Wang et al., 2015).

ATAK is used to predict the residuals at fine resolution by a linear combination of neighboring values at coarse-scale (Kyriakidis, 2004; Park, 2013) as calculated below:

$$\hat{Z}_i^{ATAK(resi)(F)} = \sum_{i=1}^{N} \lambda_i \hat{Z}_i^{RK(resi)(C)} \quad \textbf{(6)}$$

Equation 6: Residual downscaling using ATAK.

Where:

- $\hat{Z}_i^{RK(resi)(C)}$ refers to the residual component value at coarse-scale,
- $\hat{Z}_i^{ATAK(resi)(F)}$ are the downscaled fine-scale residuals calculated as a linear combination of N coarse residuals surrounding fine-scale pixels,
- λ_i is the kriging weight assigned to the neighboring residuals $\hat{Z}_i^{RK(resi)(C)}$ of coarse-scale at the prediction location,
- ATAK accounts for spatial correlation, which is ignored in regression. The objective of ATAK is to obtain $\mathbf{N}$ weights $\lambda_1, \ldots, \lambda_N$. The weights are calculated by minimizing the prediction error variance and kriging matrix made by convoluting coarse-to-coarse and fine-to-coarse semivariogram with point spread function (PSF) with which coarse-to-coarse and fine-to-coarse residual semivariograms are obtained.
- The issue in ATAK is the estimation of fine-to-fine residual semivariogram, which is solved using deconvolution of the coarse residual image to derive coarse residual semivariogram. Considering the same approach used in (Atkinson et al., 2008; Wang et al., 2015; Wang, Shi, & Atkinson, 2016), the fine-to-fine residual semivariogram is convolved to regularize semivariogram using two parameters and zero nugget effect. Then, the optimum parameters are selected from a pool of candidates. Finally, the combination leading to the smallest difference between convolved fine-to-fine residual semivariogram and coarse residual semivariogram is utilized.

$$\hat{Z}_0^{RK(F)} = \sum_{p=0}^{P} \hat{\beta}_p x_{0p} + \sum_{i=1}^{K} \lambda_{0i} e_i; \qquad x_{00} = 1, \tag{7}$$

Equation 7: Fine-scale regression prediction.

Similar to *Equation 4,* regression kriging is used to model prediction, but this time at fine resolution $\hat{Z}_0^{RK(F)}$ without upscaling the covariates to observed coarse data. This relationship built at coarse resolution can be applied at fine spatial resolution assuming the relationship in *Equation 4* to be universal (Park, 2013; Wang et al., 2015).

$$\hat{Z}_0^{ATARK(F)} = \hat{Z}_0^{RK(F)} + \hat{Z}_0^{ATAK(resi)(F)} \tag{8}$$

Equation 8: ATARK downscaled predictions.

Where:

- $\hat{Z}_0^{ATARK(F)}$ refers to ATARK fine-scale downscaled predictions,
- $\hat{Z}_0^{RK(F)}$ are the predictions obtained from regression kriging,
- $\hat{Z}_0^{ATAK(resi)(F)}$ denotes the fine-scale residuals obtained from the ATAK approach.

5.4.3.4. Accuracy assessment

The purpose of the quantitative assessment is to assess the results of predictions carried out. The downscaled methane data were validated against the coarse resolution satellite data using the leave one out cross-validation technique (LOOCV) since no ground measurements were available (Hengl, 2007). Also, due to no reference image to check for downscaling results, the mean, standard deviation (SD), and variance were used (Zhang et al., 2012). In addition, other three indices, including mean absolute error (MAE) (*Equation 9),* which indicate how close predictions are to the actual values, correlation coefficient (CC) measures the strength of relation, which is downscaled methane emissions to coarse resolution CH_4 emissions (*Equation 10)* and, Coherence (CH) statistics, an index measuring the relation between the coarse resolution CH_4 and upscaling fine resolution downscaled CH_4 predictions, were used. MAE was considered over RMSE for my study as outliers are regarded as an absolute value rather than excluding them and due to lack of pixels for downscaling (Anon, 2019). The best case for predictions has CC and CH close to one, MAE as low as possible (Pardo-Igúzquiza et al., 2006; Tang, Atkinson, & Zhang, 2015; Wang, Rodriguez-Galiano, & Atkinson, 2017).

$$MAE = abs\left(\frac{\sum_{i=1}^{n}(observed - predicted)}{n}\right) \tag{9}$$

$$CC = \frac{\sum(\mathbf{observed} - \overline{\mathbf{observed}})(\mathbf{predicted} - \overline{\mathbf{predicted}})}{\sqrt{\sum(\mathbf{observed} - \overline{\mathbf{observed}})^2 \sum(\mathbf{predicted} - \overline{\mathbf{predicted}})^2}} \quad \textbf{(10)}$$

Equation 9,10: Equation for MAE and CC.

Where:

- n is the number of observations,
- abs refers to absolute value.

5.4.4. Quantifying changes in methane emissions

After estimating the technique, which gives better evaluation results, it is used for quantifying temporal changes in methane emissions over the recorded years. Trend analysis is used to capture the changing trends using maximum methane emission values over a selected subset of an area within the study region. Furthermore, the temporal profile is applied to describe the varying pattern.

6. RESULTS

6.1. Covariate selection (1st objective)

For this analysis, the variables were upscaled via bilinear interpolation to 7000 * 3500 m resolution. 22 variables consisting of 51 datasets were tested for CC, AIC stepwise index as shown in Table 1, Figure 4, and *Appendix 1*. MODIS1 LST DAY 500 m showed the highest correlation value of 0.40, followed by MODIS2 LST NIGHT 500 m -0.37, NDVI VIIRS -0.34, Enhanced Vegetation Index (EVI2) VIIRS -0.22, and Digital Elevation Model (DEM) -0.07. Adding the datasets mentioned above showed improved values of AIC, R^2, and adjusted R^2 values. Thus, five auxiliary variables were selected for downscaling methane emissions. Landsat and Soil Moisture Index (SMI) dataset was not considered part of the covariate selection process as the dataset did not provide continuous coverage for the study area. Compared to other datasets where the number of missing pixels was few, Landsat and SMI datasets had huge unfilled gaps of missing pixels values.

Table 1: Pearson correlation values for 22 variables consisting of 51 different datasets.

	Methane
Methane	**1**
aspect	0.044093256
DEM	-0.076550148
diffuse_radiation	-0.079043484
direct_duration	0.082773541
direct_radiation	-0.075342544
EMI31_MODIS1	-0.125459194
EMI31_MODIS2	-0.134647395
EMI32_MODIS1	-0.11709101
EMI32_MODIS2	-0.11901522
ET1	-0.158948039
ET2	-0.158948219
FPAR1	-0.102491917
FPAR2	-0.102491917
LAI1	-0.16882262
LAI2	-0.16882262
LE1	-0.159902013
LE2	-0.159901935
LSTday_MODIS1	0.404886195
LSTday_MODIS2	0.366669825
LSTnight_MODIS1	-0.36097244
LSTnight_MODIS2	-0.328474749
PET1	-0.048782919
PET2	-0.048782753
PLE1	-0.049672561
PLE2	-0.049672419
S1	0.03998825
S2	0.056002702
S3	-0.013916185
S5	-0.159902013
S6	0.033394484
S7	-0.050897643
S8	0.097330324
S9	0.118020244
solar_radiation	-0.07690021
slope	-0.081407497
EVI250	-0.188265306
EVI1000	-0.206086131
NDVI_MODIS250	-0.239017988
NDVI_MODIS1000	-0.26721999
NDVI_VIIRS_500	-0.343133763
EVI2_VIIRS_500	-0.220611786
EVI1_VIIRS_500	-0.227941889
NDVI_MODISA1_500	-0.232605289
EVI_MODISA1_500	-0.186656162
LSTday_MODIS1_500	0.409917321
LSTnight_MODIS1_500	-0.371652003
LSTday_MODIS2_500	0.374724306
LSTnight_MODIS2_500	-0.33724908

BT_landsat7	0.35250488
BT10_landsat8	0.226513891
BT11_landsat8	0.247372361
EVI_landsat7	0.031979053
EVI_landsat8	-0.190251156
LST06_landsat7	0.401319059
LST10_landsat8	0.273473857
LST11_landsat8	0.277364149
NDVI_landsat7	0.116364687
NDVI_landsat8	-0.140246328
NDWI_landsat7	-0.029303146
NDWI_landsat8	-0.209257773

Stepwise Selection Summary

Step	Variable	Added/ Removed	R-Square	Adj. R-Square	C(p)	AIC	RMSE
1	values(layerstack$LSTday_MODIS1_500)	addition	0.192	0.192	1647.7250	26364.9400	12.4903
2	values(layerstack$LSTnight_MODIS2_500)	addition	0.242	0.241	1343.7210	26155.2564	12.1027
3	values(layerstack$EVI_landsat8)	addition	0.286	0.285	1074.8240	25957.9711	11.7489
4	values(layerstack$NDVI_VIIRS_500)	addition	0.302	0.301	973.3270	25880.5828	11.6120
5	values(layerstack$diffuse_radiation)	addition	0.316	0.315	893.5140	25818.4644	11.5028
6	values(layerstack$BT_landsat7)	addition	0.347	0.346	574.5530	20110.3232	11.2803
7	values(layerstack$S2)	addition	0.366	0.364	486.2240	20036.8561	11.1209
8	values(layerstack$S1)	addition	0.385	0.383	396.6100	19960.0243	10.9567
9	values(layerstack$diffuse_radiation)	removal	0.385	0.383	396.1880	19959.4028	10.9575
10	values(layerstack$NDVI_MODISA1_500)	addition	0.408	0.407	281.4640	19857.4515	10.7440
11	values(layerstack$LSTday_MODIS2_500)	addition	0.421	0.419	220.8870	19801.9731	10.6286
12	values(layerstack$aspect)	addition	0.429	0.427	184.6780	19768.2459	10.5583
13	values(layerstack$EVI_landsat7)	addition	0.436	0.434	152.9670	19738.3149	10.4961
14	values(layerstack$S7)	addition	0.441	0.439	129.1020	19715.5481	10.4485
15	values(layerstack$NDWI_landsat8)	addition	0.445	0.443	112.0950	19699.1977	10.4140
16	values(layerstack$LSTnight_MODIS1_500)	addition	0.448	0.445	99.3510	19686.8741	10.3875
17	values(layerstack$NDVI_landsat8)	addition	0.451	0.448	88.4020	19676.2282	10.3644
18	values(layerstack$S3)	addition	0.453	0.450	81.1490	19669.1550	10.3484
19	values(layerstack$EVI_landsat8)	removal	0.453	0.450	79.2620	19667.2664	10.3467
20	values(layerstack$EVI2_VIIRS_500)	addition	0.457	0.454	60.1260	19648.4221	10.3075
21	values(layerstack$EVI1_VIIRS_500)	addition	0.462	0.458	41.1120	19629.5331	10.2684
22	values(layerstack$NDWI_landsat7)	addition	0.463	0.459	36.2440	19624.6698	10.2569
23	values(layerstack$NDVI_MODIS250)	addition	0.464	0.460	32.4490	19620.8643	10.2475
24	values(layerstack$BT10_landsat8)	addition	0.443	0.438	115.1630	17553.6468	10.4295
25	values(layerstack$NDWI_landsat7)	removal	0.442	0.437	115.6330	17554.0403	10.4326
26	values(layerstack$PLE2)	addition	0.443	0.438	113.1380	17551.6827	10.4251
27	values(layerstack$PET2)	addition	0.446	0.441	100.8300	17539.7574	10.3962
28	values(layerstack$EMI31_MODIS2)	addition	0.448	0.442	96.9580	17536.0183	10.3857
29	values(layerstack$LSTnight_MODIS2)	addition	0.449	0.443	94.4090	17533.5626	10.3780
30	values(layerstack$NDVI_landsat7)	addition	0.449	0.444	93.4700	17532.6790	10.3738
31	values(layerstack$NDVI_landsat7)	removal	0.449	0.443	94.4090	17533.5626	10.3780
32	values(layerstack$S9)	addition	0.449	0.444	93.6060	17532.8126	10.3741
33	values(layerstack$S9)	removal	0.449	0.443	94.4090	17533.5626	10.3780

Figure 4: Stepwise regression results using Akaike index.

6.2. Multicollinearity

The Spearman's rank correlation coefficient value of >=0.7 was decided as a threshold value between the auxiliary variables. The variables selected if showed a correlation value greater or equal to 0.7 were eliminated. Figure 5 shows the multicollinearity index for and between each pair of variables. As the plot depicts, none of the chosen covariates indicated this issue.

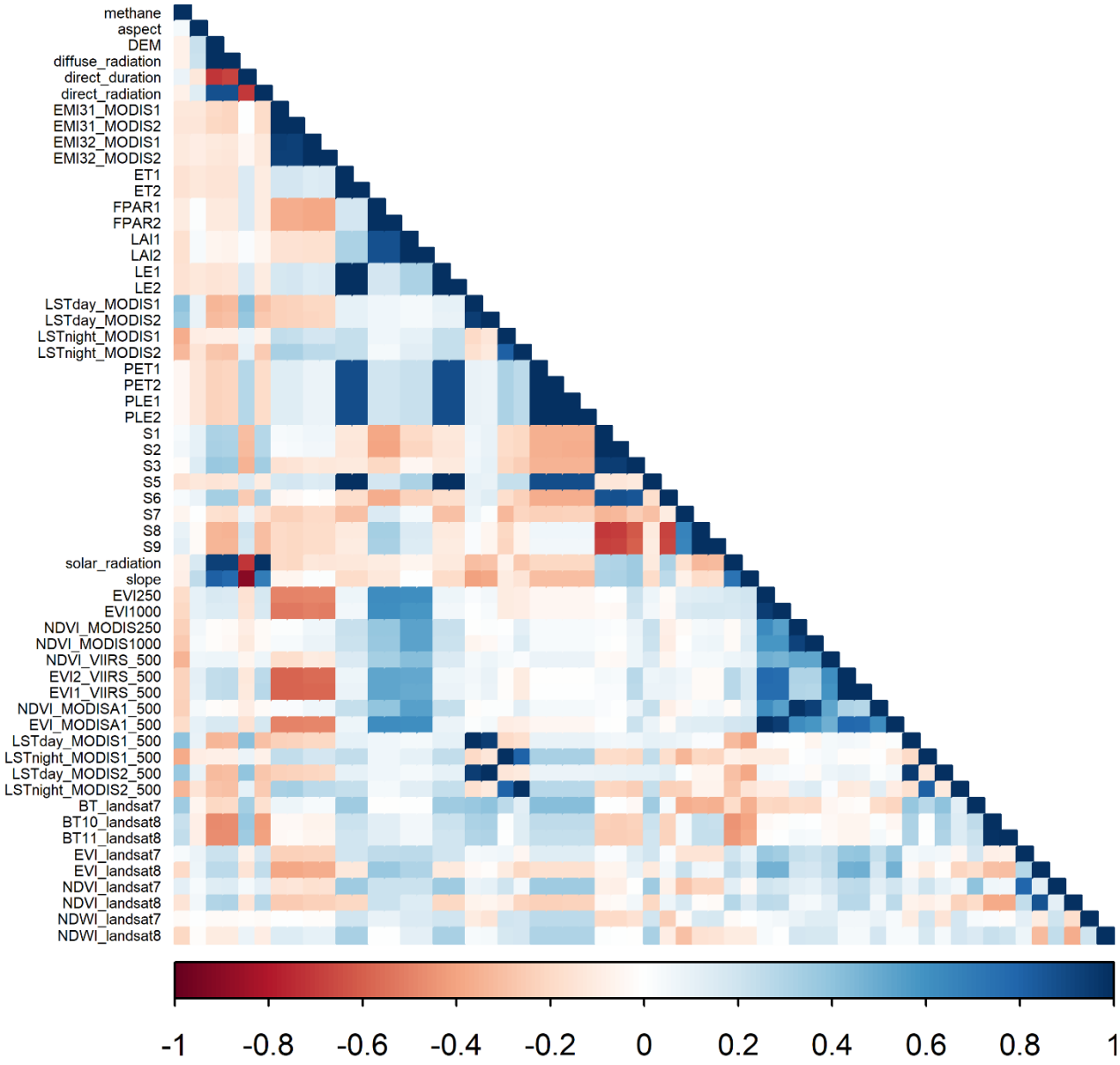

Figure 5: Multicollinearity index for covariate selection

6.3. Data exploration results

Descriptive and quantitative statistics over methane (dependent variable) and covariates (LSTDAY, LSTNIGHT, NDVI, DEM, EVI) were plotted to understand the distribution, linear/non-linear relationship, and positive or negative relationship. On plotting the histograms (Figure 6), it can be seen that the monthly mean of methane and EVI are normally distributed, DEM is right-skewed, and the remaining covariates LSTDAY, LSTNIGHT, NDVI are left-skewed. The data for methane was normally distributed, so no log transformation was undertaken to achieve approximate normal distribution. Scatterplots in Figure 7 were used to understand the relationship between dependent variables and independent variables. As can be seen except for LST DAY, the remaining auxiliary variables show a non-linear relationship.

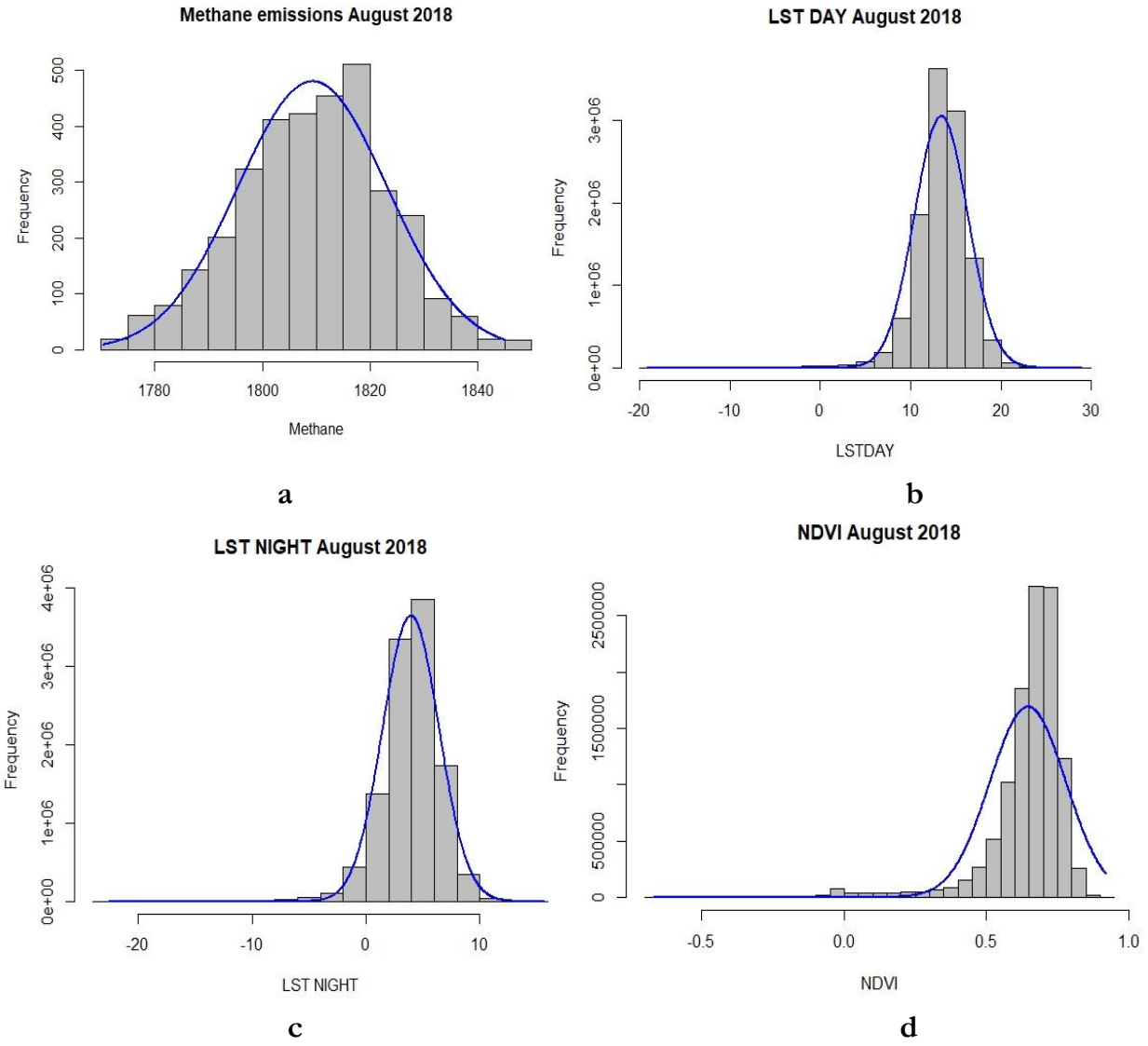

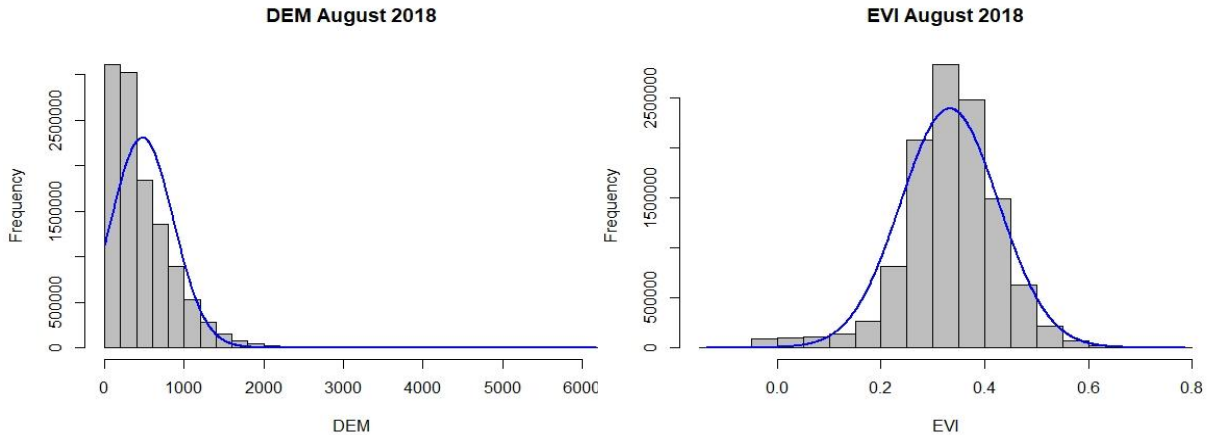

e **f**

Figure 6: Histogram plots for dependent variable and covariates (a) methane, (b) LST DAY, (c) LST NIGHT. (d) NDVI. (e) DEM. (f) EVI. for the month 08/2018.

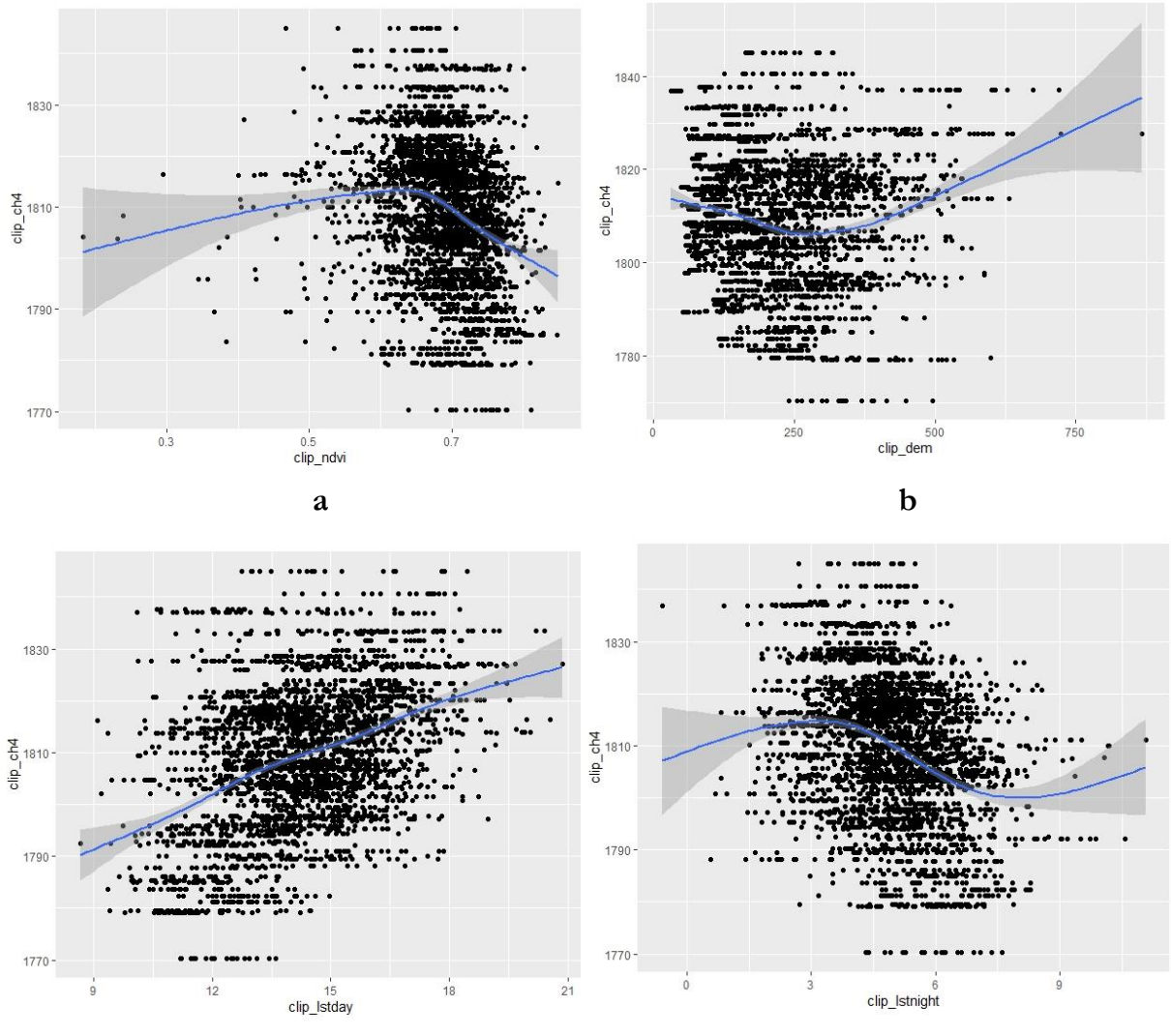

a **b**

c **d**

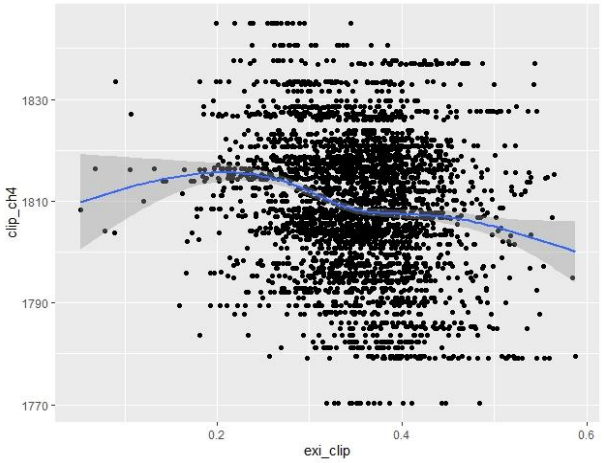

e

Figure 7: Scatterplot showing linear and non-linear relationship between methane and auxiliary variables (a) LST DAY, (b) LST NIGHT, (c) NDVI, (d) DEM, (e) EVI. for the month 08/2018.

6.4. Regression model selection

The first section for the two (RK and ATARK) techniques requires regression analysis. However, for ATARK, the relationship is modeled by linear regression (Park, 2013; Wang et al., 2015). Since variables show linear and non-linear relationships with dependent variables, testing of different regression models were done. The data was divided into a 60:40 ratio using hold out a sub-sample technique (Kassambara, 2018). Among different regression models, linear regression showed a higher R^2 of 0.29 and lower RMSE, MAE value of 11.47, 9.04 (Table 2). It explains about 29% of the variance in methane emissions compared to other models. Thus, for the regression modeling kriging approach, linear regression was selected.

Table 2: Model type and its parameters performance values.

Model	R^2	RMSE	MAE
Simple Linear regression	0.29	11.47	9.04
Polynomial regression 1	0.005	13.62	11.08
Polynomial regression 2	0.055	13.29	10.86
Polynomial regression 3	0.05	13.28	10.86
Polynomial regression 4	0.06	13.24	10.82
Polynomial regression 5	0.06	13.24	10.81
Polynomial regression 6	0.06	13.24	10.81
Log transformation (dependent variable)	0.29	1801.88	1801.83
Log transformation (independent variable)	0.01	13.56	11.09
Log transformation (both)	0.01	1801.88	1801.83
Spline regression	0.05	13.28	10.86
Generative additive model	0.19	12.22	9.86
Genelarized Linear model	0.29	11.49	9.04

6.5. Pre-processing results

Tiles 17 and 21 were selected to compare the three kriging interpolation techniques for the month of August 2018.

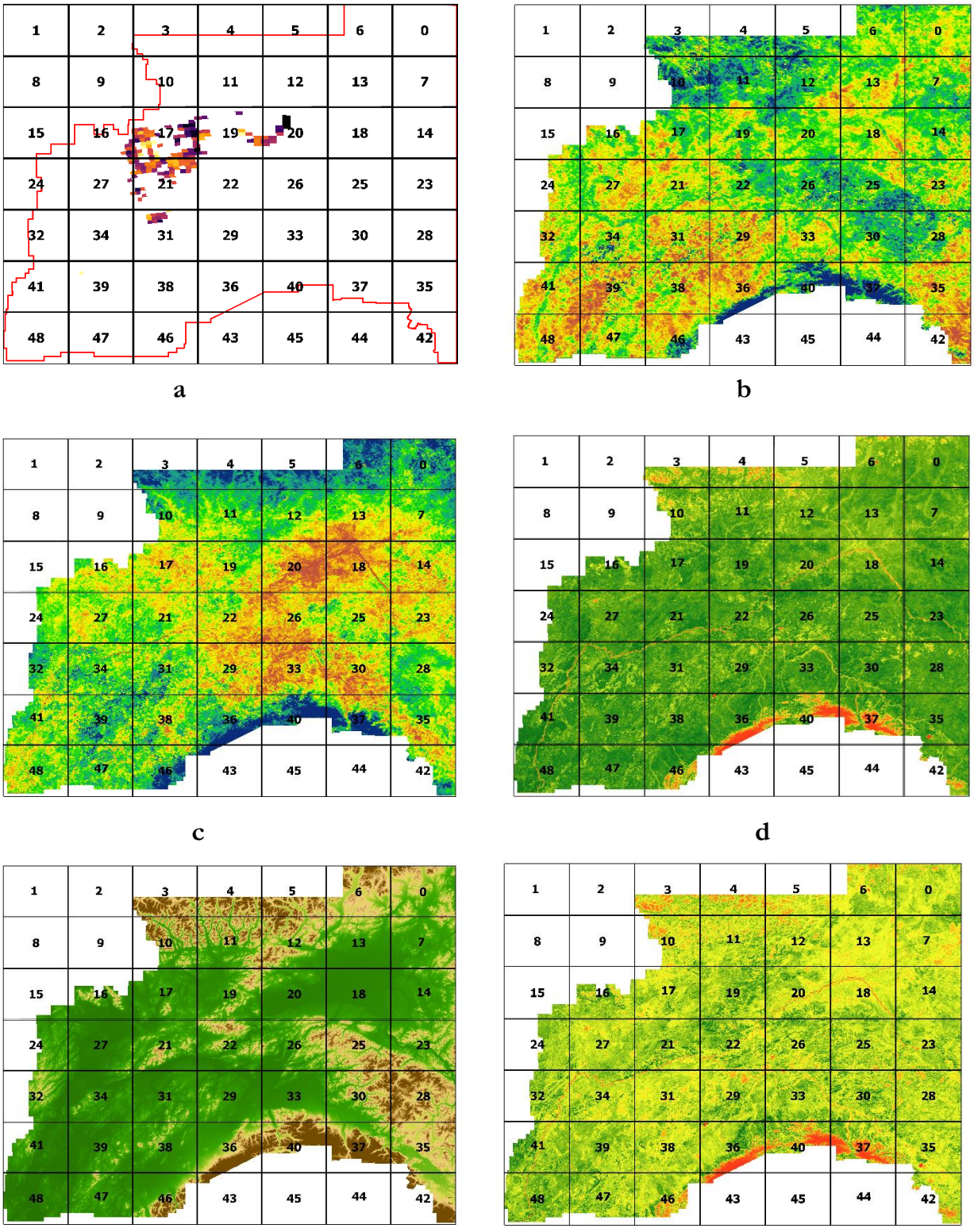

Figure 8: Grid overlay over (a) methane data, (b) LST DAY, (c) LST NIGHT, (d) NDVI, (e) DEM, (f) EVI.

6.6. Downscaling and comparing techniques (2nd objective)

In this study, the second objective is to compare techniques and estimate which technique best describes downscaled methane emissions. Finally, the selected technique is used to attain the third objective of monitoring changes in methane emissions over the years. Three techniques named RK, ATAK, and ATARK were performed for comparison over a single month, August 2018, on two tiles 17, 21. The tiles were selected based on a greater number of pixels within the tile that would help compare the three techniques cross-validation results.

6.6.1. Model and parameters selection

The semivariance parameters are dependent on the semivariance function for accurate predictions (Adigi, 2019). The spatial structure of methane for monthly mean was analyzed using three different models: the spherical (Sph), the exponential (Exp), and the Gaussian (Gau). RK and ATARK regression and residual predictions were made using a global semivariogram with an Exponential model, the partial sill of 150, range of 200000, and nugget of 0 (Figure 9 and Table 3). The zero nugget effect to ease the computational cost was followed in this paper (Pardo-Igúzquiza et al., 2006; Wang et al., 2015).

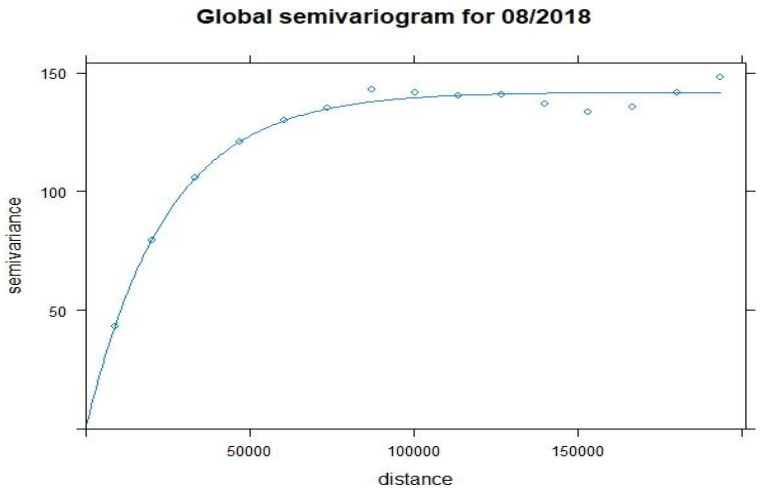

Figure 9: Global semivariogram for RK and ATARK

Table 3: *Global semivariogram functions and model parameters*

Month/year	Cutoff	Width	Psill	Model	Range	Nugget
Aug-18	200000	-	150	Exponential	200000	0

6.6.2. Semivariogram deconvolution result (ATAK AND ATARK)

6.6.2.1. ATAK

Unlike ATARK, where the residuals are downscaled, in ATAK, the original coarse data is downscaled without the effects of auxiliary variables. As a result, as shown in Table 4 and Figure 10, the semivariogram deconvolution results have a correlation structure with a range of 40000 for tiles 17 and 21. In addition, the fitted area variogram and deconvoluted point variogram seem to coincide and show a similar correlation structure.

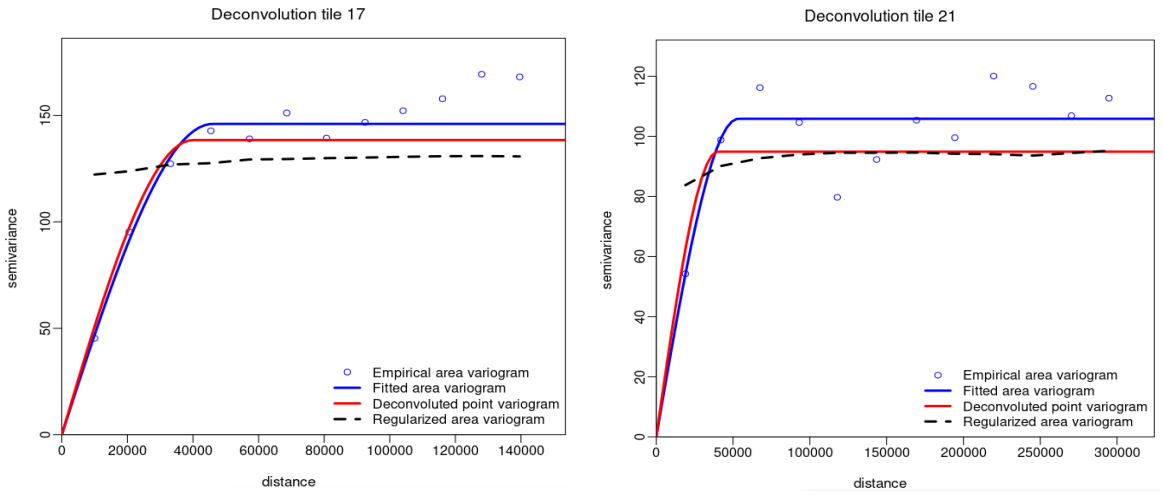

a **b**

Figure 10: Semivariogram deconvolution results using ATAK approach for tile 17 (a) and 21 (b).

Table 4: Semivariogram deconvolution results for ATAK

Date	Tile number	Psill	Model	Range(m)
Aug-18	17	198	Sph	40000
Aug-18	21	94	Sph	40000

6.6.2.2. ATARK

After generating residuals from multiple regression analysis at a coarse-scale (7000 * 3500 m), areal semivariogram deconvolution was applied to estimate unknown area-support semivariogram of the residuals. Each residual tile was discretized to 500 m which is the target resolution to be downscaled to. The areal semivariogram of the residuals has a very small correlation structure, as shown in Figure 11. It is clear that the deconvoluted point variogram and fitted area variogram are not similar and do not coincide. The semivariogram implies that the residual components are spatially independent. Since no spatial correlation was found between residuals, the residuals estimation approach could not provide efficient results. Table 5 shows the fitted parameters for deconvolution of coarse-scale residuals.

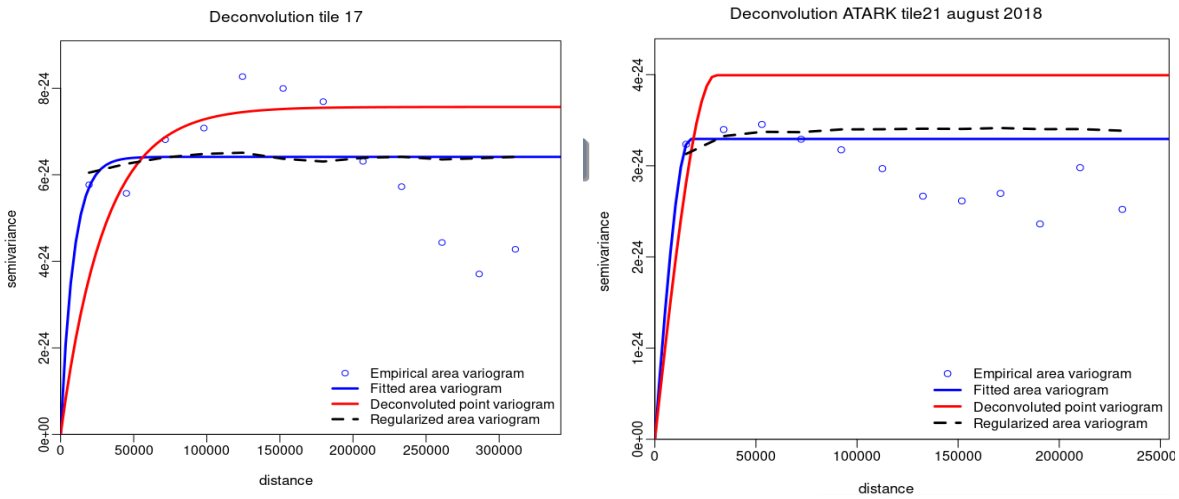

a **b**

Figure 11: Semivariogram residual deconvolution results using ATARK approach for tile 17 (a) and

Table 5: Semivariogram deconvolution results for ATARK

Date	Tile number	Psill	Model	Range(m)
Aug-18	17	7.71126E-24	Exp	40000
Aug-18	21	3.99413E-24	Sph	30000

6.6.3. Statistical measures of downscaling results

Comparing the results of the three downscaled techniques RK and ATARK show a similar spatial distribution. In contrast, ATAK shows a smoothing effect since this method is based on just the autocorrelation of coarse resolution CH_4 data (Figure 12). RK and ATARK achieved a significant spatial detail in emissions because spatial variations of the covariates were involved in their interpolation results.

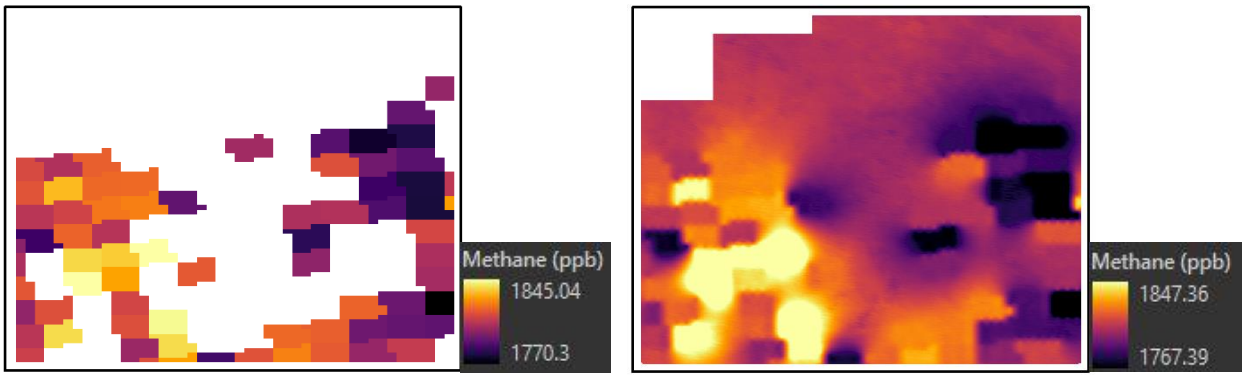

a **b**

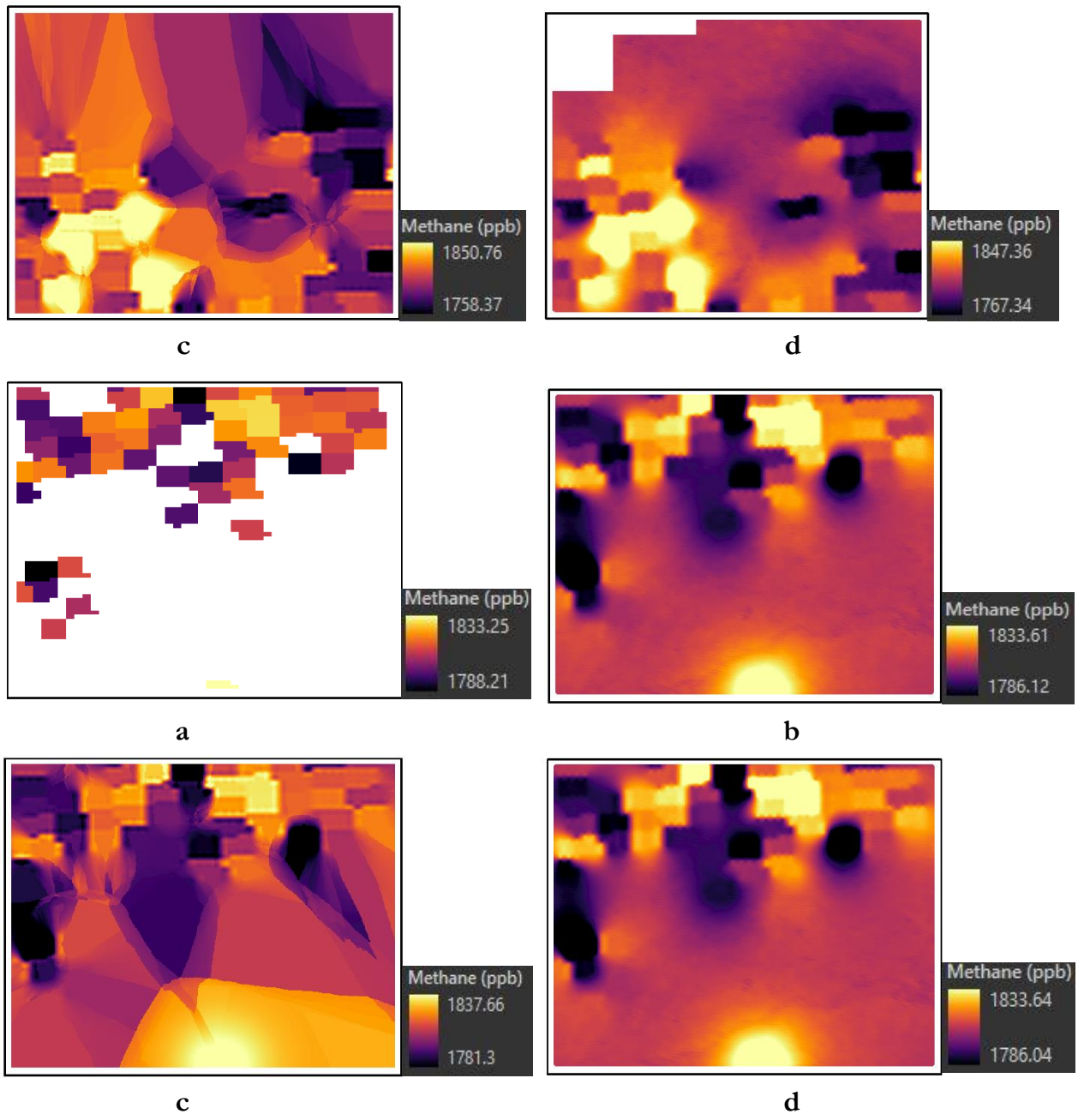

Figure 12: Downscaling methane concentration 500 m resolution of a) actual image tile 17, 20, b) RK tile 17, 20 c) ATAK tile 17, 20 and, d) ATARK tile 17, 21.

Since there is no reference image to check the downscaled results, six indices were used upon the interpolated images and original dataset. Table 6 exhibits the quantitative assessment of the downscaling methods. ATAK provides close SD and means of 12.30, 151.24 to the original dataset 15.07, 227.23 (tile17). The MAE and CC results show ATAK outperformed the other two techniques with an MAE and CC value of 1.35, 0.99 for ATAK, 2.23, 0.96 values for RK, and 1.39, 0.98 values for ATARK (tile 17).

Table 6: Comparison results between ATAK, ATARK, and RK. Actual image is the original coarse resolution data values

Tile number	Model	Mean	Variance	SD	MAE	CC	CH
17	Actual image	1808.95	227.23	15.07			
17	RK	1808.42	118.62	10.89	2.23	0.96	0.98
17	ATARK	1808.41	119.39	10.93	1.39	0.98	0.98
17	ATAK	1808.23	151.24	12.30	1.35	0.98	0.99
21	Actual image	1812.34	99.58	9.98			
21	RK	1811.83	41.56	6.45	1.64	0.96	0.98
21	ATARK	1811.86	41.99	6.48	0.09	0.99	0.98
21	ATAK	1813.20	78.59	8.87	0.06	0.99	0.99

Another essential criterion for evaluation is coherence statistics. The downscaled CH_4 emissions were upscaled to the original resolution to check for correlation values. Figure 13 show the scatterplots of each tile for all three techniques. RK and ATARK show a lower coherence statistic with the original image for tile 17 with a CH value of 0.98, 0.97 than ATAK showing a value of 0.99 (Table 6).

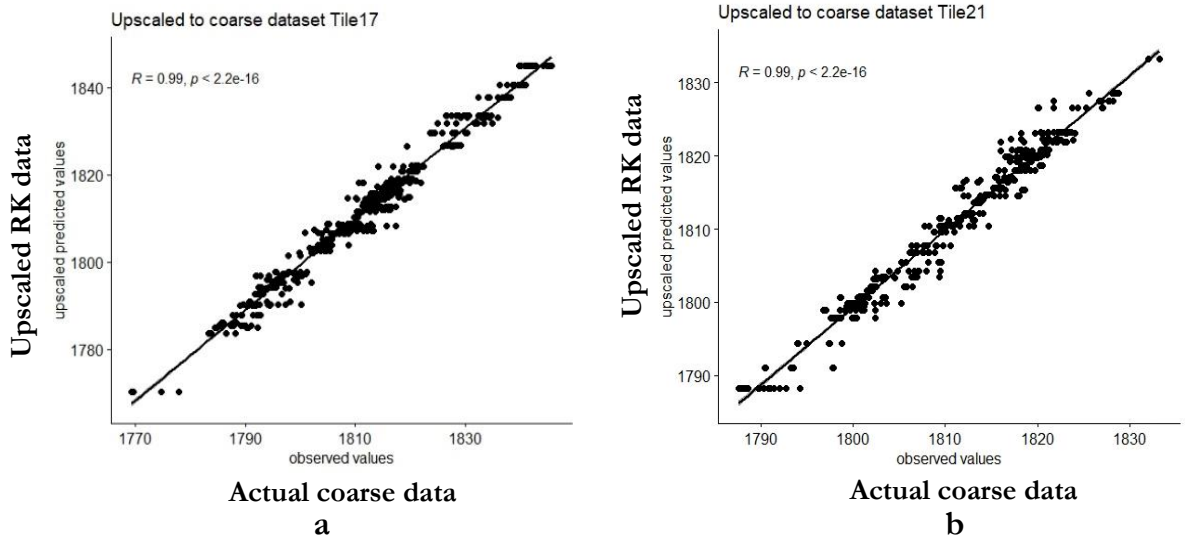

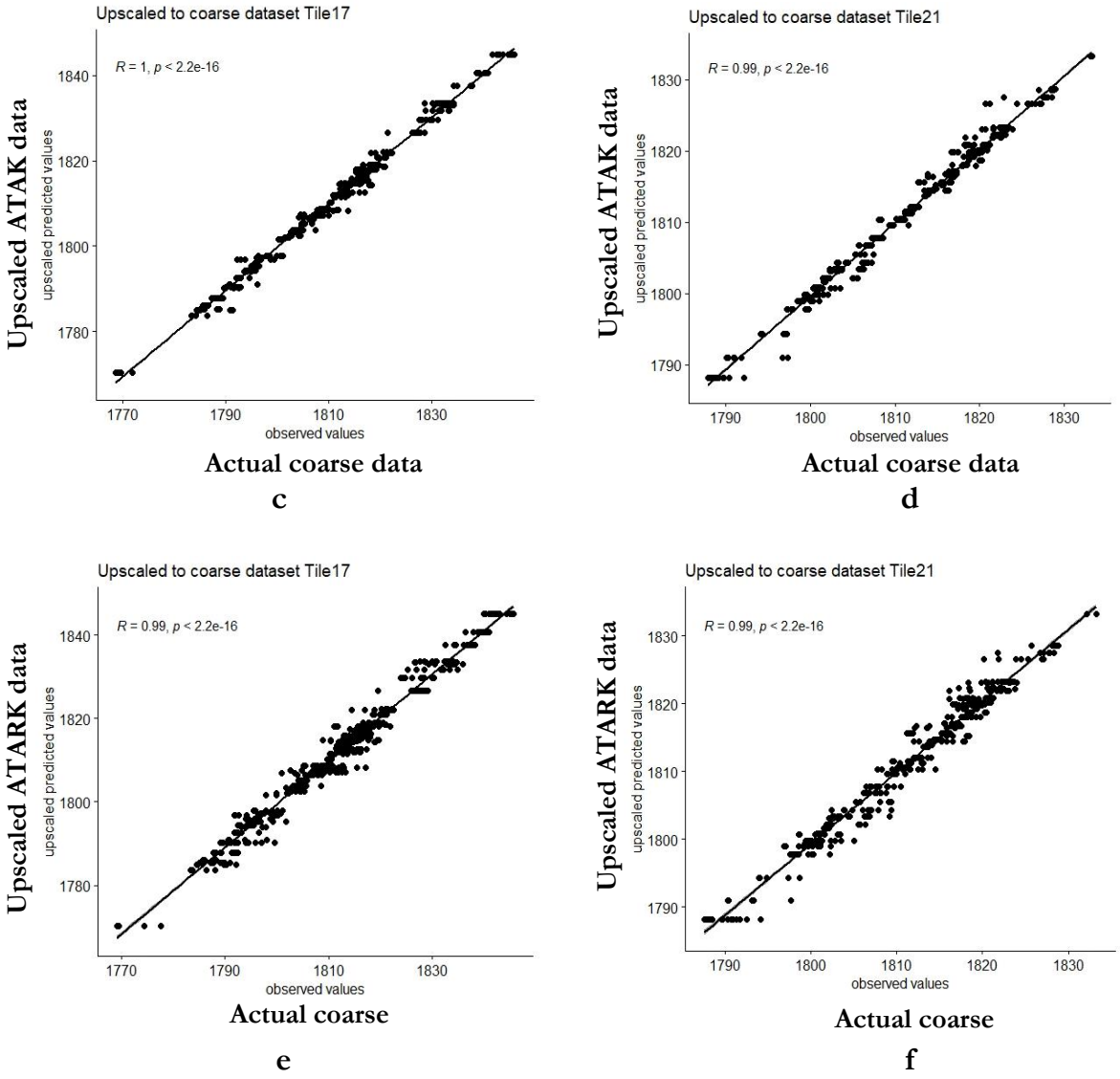

Figure 13: Coherence statistics using scatterplots of upscaled predictions against actual observed values for tile 17 and 20 (a),(b) RK, (c),(d)ATAK and (e),(f)ATARK .

6.7. Monitoring changes in methane emissions (3rd objective)

After estimating the technique that provides the best estimates of methane emissions, ATAK was used to downscale and monitor changes in methane emissions with the increasing global temperatures. Figure 14 depicts time-series mean monthly predictions of the emissions recorded from August 2018 to May 2021 using the preferred kriging technique. Deconvolution of all the tiles is presented in *Appendix 2* and estimated model parameters in *Appendix 3*. Monthly minimum and maximum values over the four years do not give much inference about the changing trends as the number of pixels is not sufficient to observe the changes, as shown in Figure 14. Even though August and May have recorded data for consecutive 2-3 years, the lack of pixel data values prevents from obtaining any supporting conclusion about the changing trends using time series. The cross-validation result using the LOOCV technique for all tiles are given in *Appendix 4*.

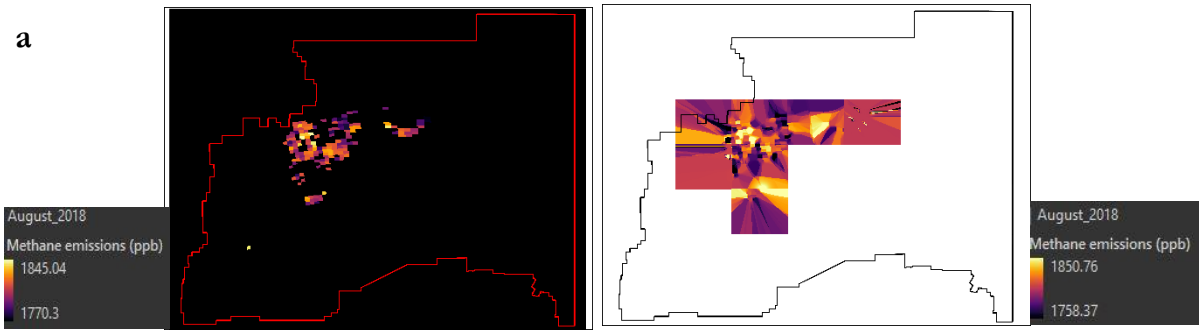
a
August_2018
Methane emissions (ppb)
1845.04
1770.3
August_2018
Methane emissions (ppb)
1850.76
1758.37

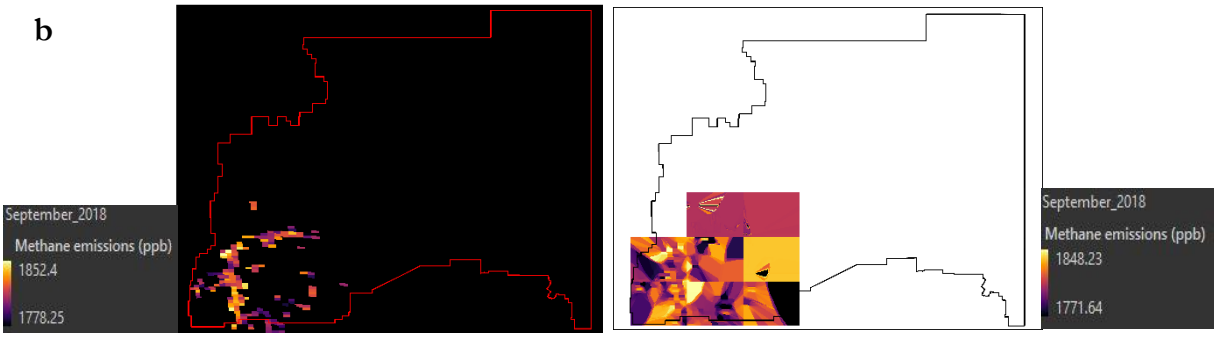
b
September_2018
Methane emissions (ppb)
1852.4
1778.25
September_2018
Methane emissions (ppb)
1848.23
1771.64

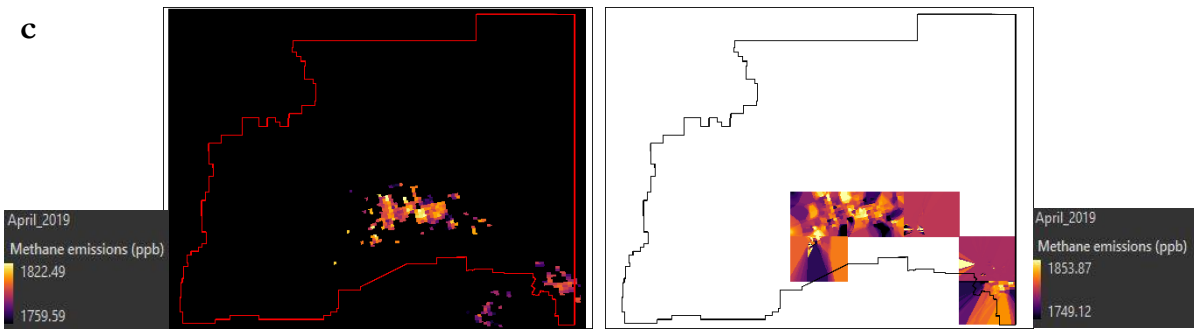
c
April_2019
Methane emissions (ppb)
1822.49
1759.59
April_2019
Methane emissions (ppb)
1853.87
1749.12

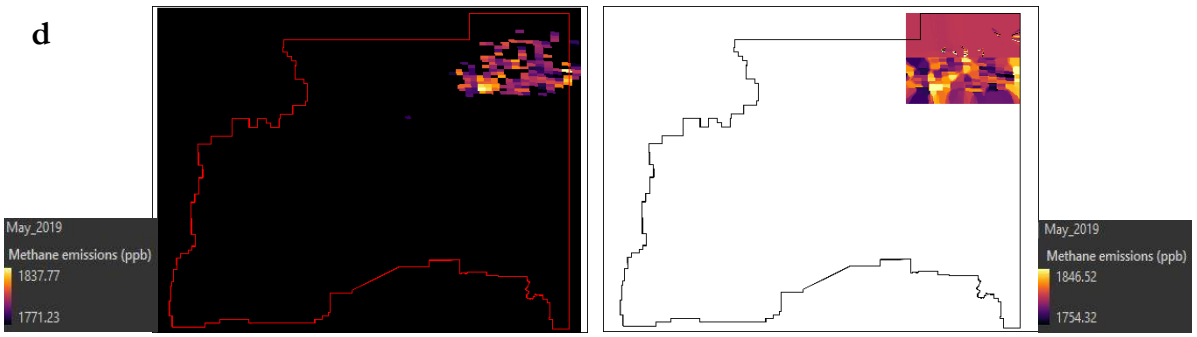
d
May_2019
Methane emissions (ppb)
1837.77
1771.23
May_2019
Methane emissions (ppb)
1846.52
1754.32

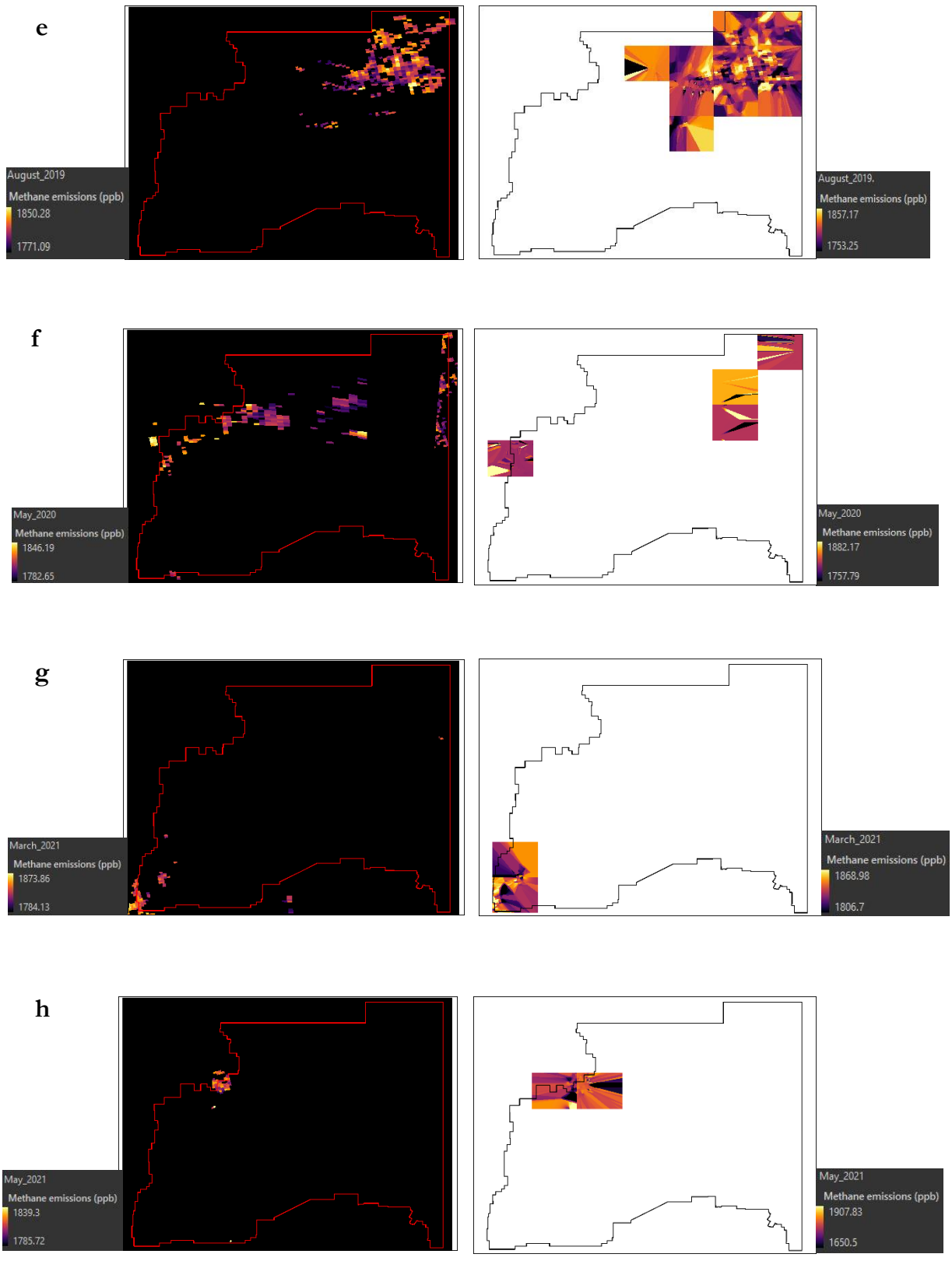

Figure 14: ATAK predictions from August 2018 – May 2021.

A smaller subset (tile 13) from the entire study area was selected to depict the changing trends in methane emissions over the time span of four years. Figure 15 shows the location of the selected area. The particular tile was selected because the changes were prominent in this particular tile using trend analysis. Areas in purple show an increase in methane emissions over the last four years, whereas green areas have faced a decrease in methane emissions. As shown in Figure 16 for the selected area of interest, the temporal profile depicts an increase in methane emissions with a rapid downfall for the following recorded years.

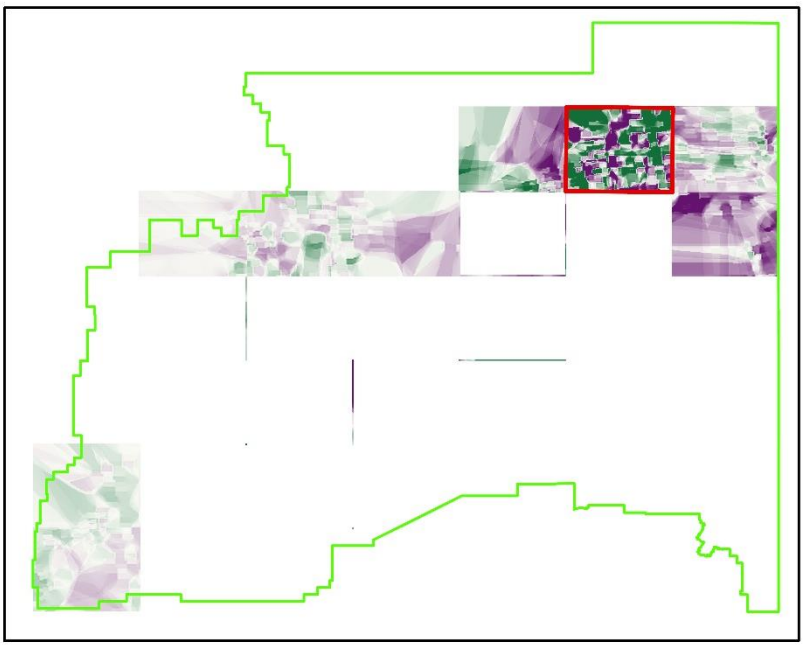

Figure 15: Area selected to capture changes in methane emissions using trend analysis.

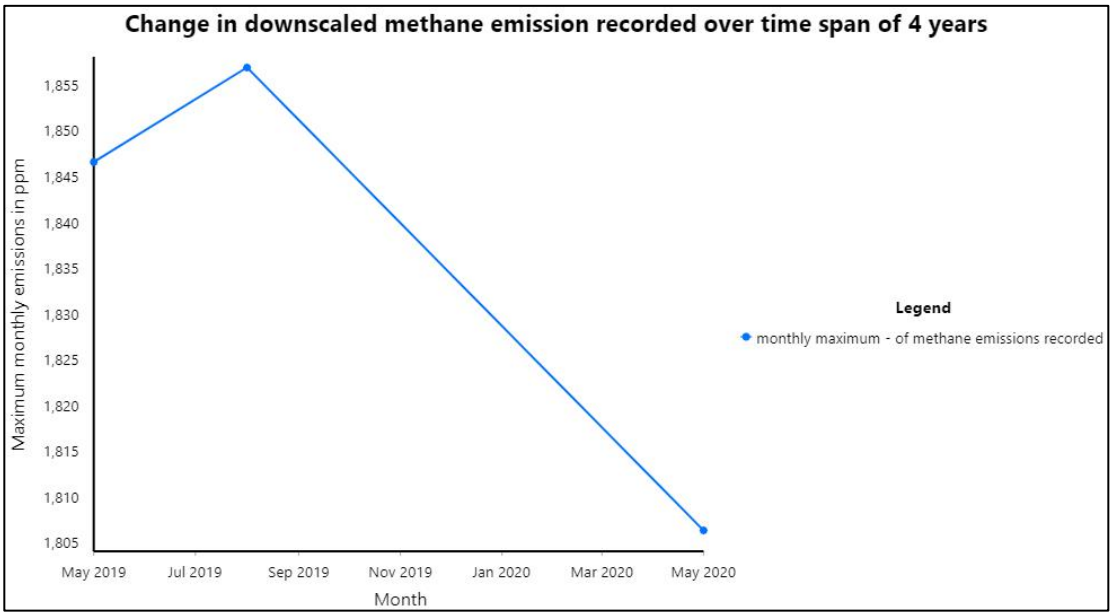

Figure 16: Temporal profile for the selected tile over the span of 4 years.

7. DISCUSSION

This thesis aimed to investigate the driving factors affecting methane emissions from abrupt permafrost thawing, which statistical downscaling technique best describes fine-scale methane data and monitors the changes in methane emissions over the years at the local level.

7.1. Discussion regarding driving factors affecting methane emissions

From the studies by Zhang et al., (2011) and Zhang et al., (2012) it is proved that, land surface temperature, organic matter, soil moisture, and vegetation index have a strong positive effect on CH_4 concentrations. Land surface temperature, derived soil moisture index, and vegetation index are the only parameters for which high spatial resolution was obtained. However, derived soil moisture index from Sentinel, Landsat7, and Landsat 8 could not be considered for this study due to the lack of satellite images covering the study area. NDVI and LST were considered as potential datasets to be used for downscaling. As per Zhang et al., (2011), and Zhang et al., (2012) CH_4 and NDVI show a high correlation retrieved using Scanning Imaging Absorption Spectrometer for Atmospheric Chartography (SCIAMACHY) and MODIS NDVI datasets because of the biophysical mechanism. Similarly, according to Zhang et al., (2011) soil temperature with soil moisture showed a highly significant relationship with methane flux. The statistical significance for this study region agrees with their findings, indicating that the covariates chosen have a statistically significant value for methane emissions, although the correlation coefficient values do not. LST (day and night) and NDVI alone or together did not show a higher correlation value (19%, 10%, 9%), but showed statistical significance ($p<0.05$). They could not explain most of the variance of the dependent variable that was analyzed using monthly means from April-May 2019. The selected time frame depended on the availability of TROPOMI CH_4 data. According to the research, one reason for the weak correlation could be a lack of pixels collected or a missing number of pixels that did not capture the relationship between the highly correlated variables. Another reason could be because of the homogeneity of the study area. As can be seen from Figure 17 methane data has gaps for some of the days, similarly, LST NIGHT and NDVI have gaps in the recorded data as the temporal resolution of these datasets is 16 days.

Previously downscaled studies did not consider elevation-derived variables such as aspect, slope which could be sensitive to methane emissions (Zhang et al., 2011). This study explored the potential sensitivity of variables related to the health of vegetation, air moisture, heat, elevation-derived indices, and water indices. To this end, a stepwise multiple regression model and AIC index were performed with each auxiliary variable mentioned in *Appendix 1* to select the best combinations of variables (Ezzine et al., 2017). In addition, the results were double-checked with multicollinearity removing all pairs of highly correlated variables because if left, they might increase the standard errors of coefficients. Thus, for multiple regression analysis, CH_4 was modeled, integrating auxiliary variables that are LST DAY, LST NIGHT, NDVI, EVI, and DEM, which were selected as the best model fit.

In this study, multiple regression using covariates such as LST DAY, LST NIGHT, NDVI, EVI, and DEM model could not explain much variance of the dependent variable, methane data. The reasons may be similar as mentioned above; due to lack of pixels, the relationship could not be captured well using auxiliary variables. Thus, for downscaling the effect using both covariates and no covariates were estimated.

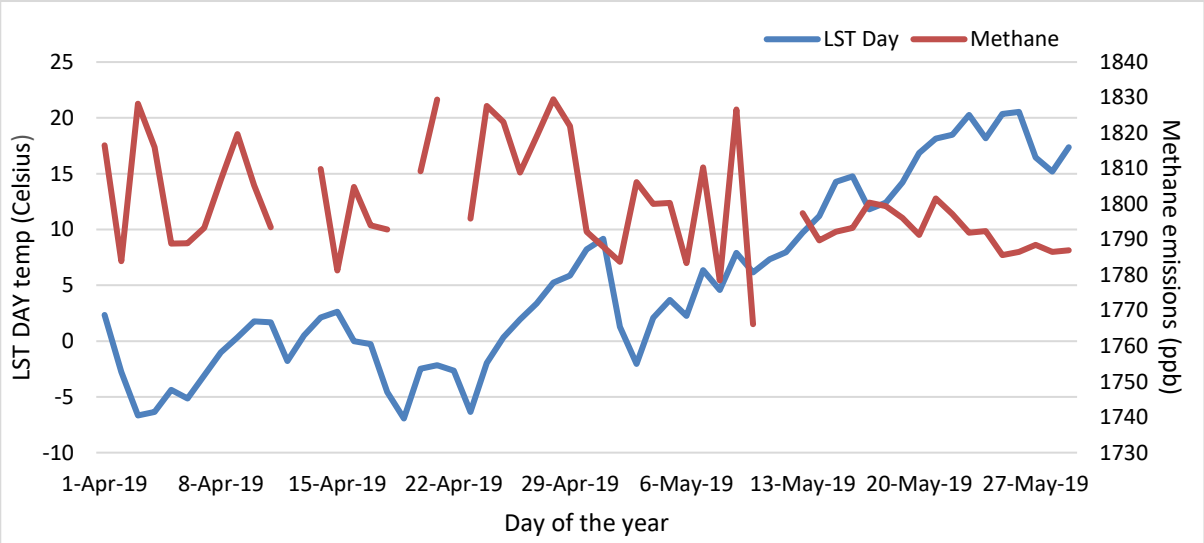
LST Day
Methane
LST DAY temp (Celsius)
Methane emissions (ppb)
25
20
15
10
5
0
-5
-10
1840
1830
1820
1810
1800
1790
1780
1770
1760
1750
1740
1730
1-Apr-19
8-Apr-19
15-Apr-19
22-Apr-19
29-Apr-19
6-May-19
13-May-19
20-May-19
27-May-19
Day of the year

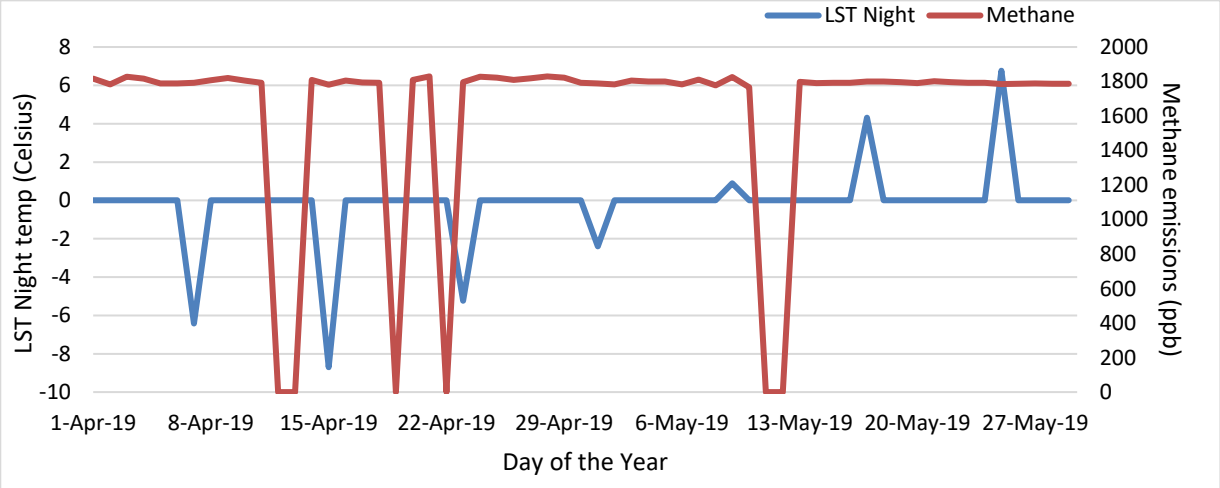
LST Night
Methane
LST Night temp (Celsius)
Methane emissions (ppb)
8
6
4
2
0
-2
-4
-6
-8
-10
2000
1800
1600
1400
1200
1000
800
600
400
200
0
1-Apr-19
8-Apr-19
15-Apr-19
22-Apr-19
29-Apr-19
6-May-19
13-May-19
20-May-19
27-May-19
Day of the Year

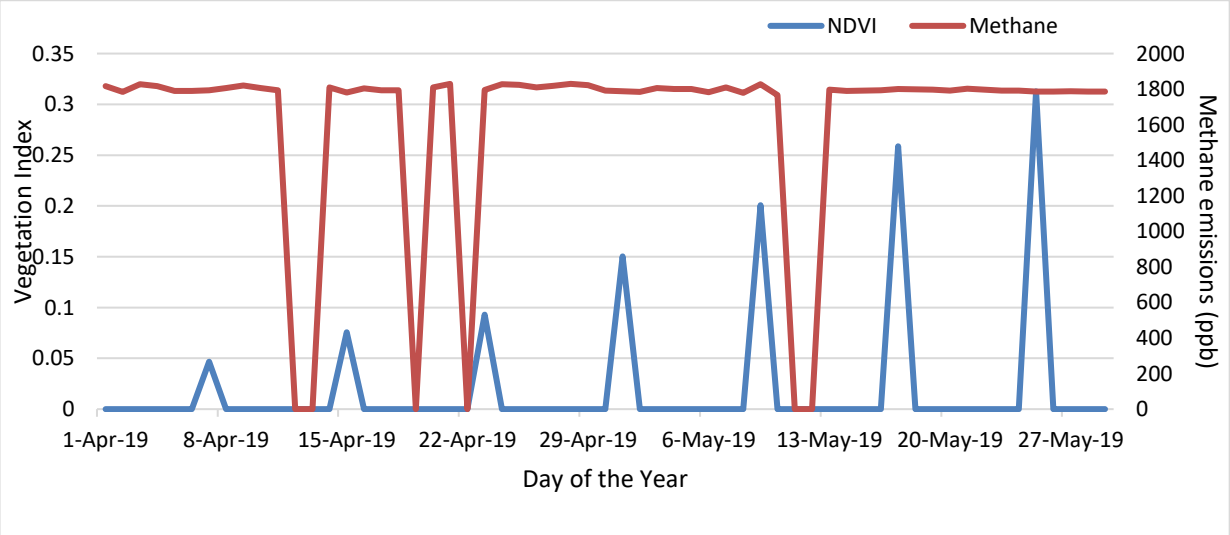
NDVI
Methane
Vegetation Index
Methane emissions (ppb)
0.35
0.3
0.25
0.2
0.15
0.1
0.05
0
2000
1800
1600
1400
1200
1000
800
600
400
200
0
1-Apr-19
8-Apr-19
15-Apr-19
22-Apr-19
29-Apr-19
6-May-19
13-May-19
20-May-19
27-May-19
Day of the Year

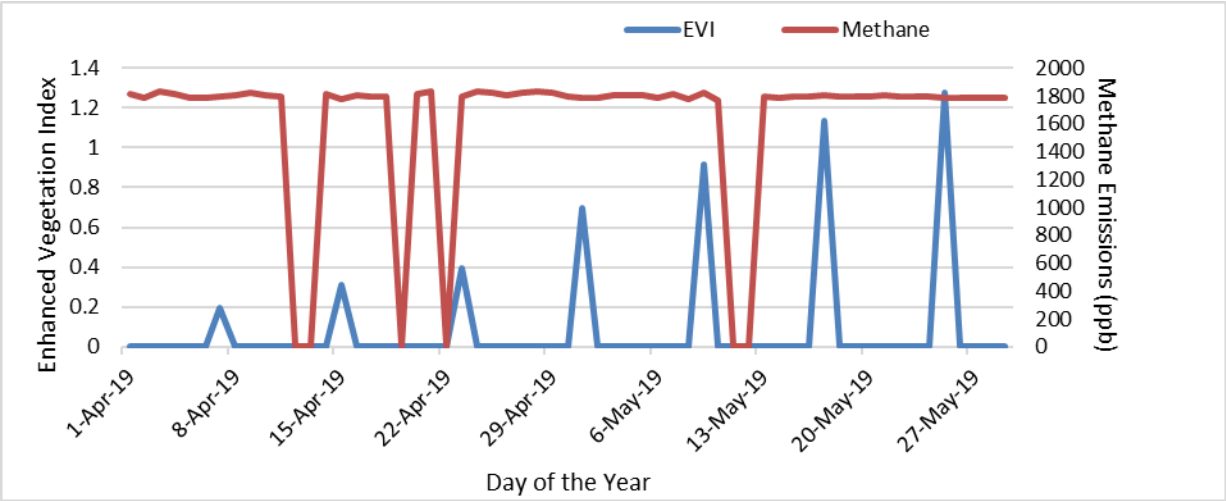

Figure 17: Daily mean of LST DAY, LST NIGHT, NDVI, EVI and METHANE values from April-May 2018.

7.2. Discussion on the performance of downscaling techniques

Three different techniques were used to downscale methane emissions to 500 m. Overall, all downscaling results were similar to those of the coarse-scale methane data, as shown in Figure 18. The results are in agreement with Park, (2013) findings of downscaling using covariates added local details compared to direct downscaling that showed distorted and smoothly varying patterns. The local details are more prominent in ATARK and RK than ATAK because the multiple regression took over the kriging where predictions were low, meaning the spatial variations of covariates had been involved in the interpolation. On the other hand, ATAK does not include any covariates, which caused the disturbing pattern observed in the images where predictions were low. When all downscaled results were averaged to original coarse-scale data, the coherence property of ATAK showed a slightly higher perseverance property of 0.99 than ATARK 0.98 and RK, which was 0.98 (Table 7). For this study, the discrepancy observed in ATARK and RK downscaled results was probably due to poor regression.

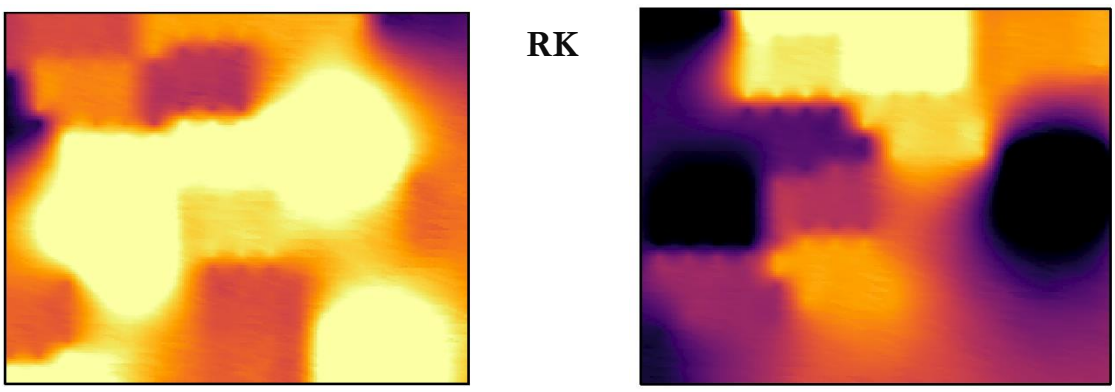

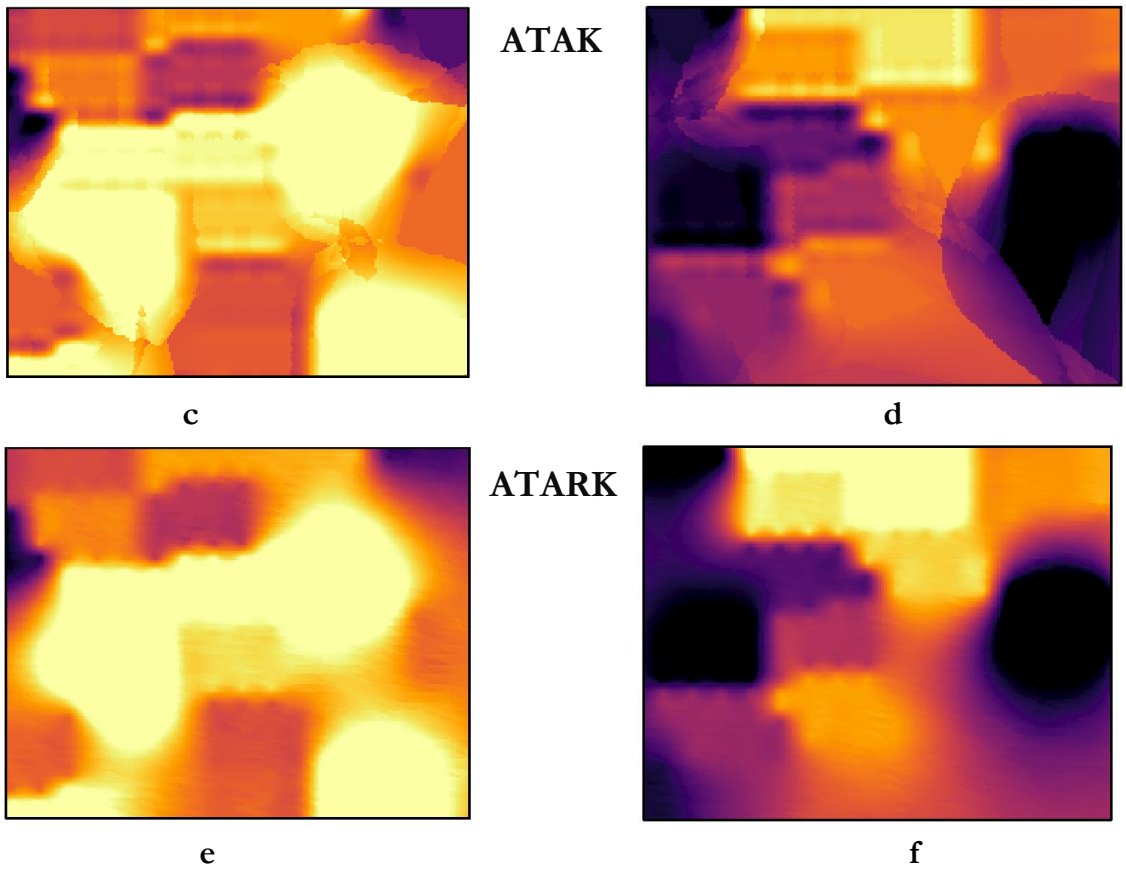

Figure 18: Zoomed in downscaled results for tiles 17 and 21 (a), (b) RK, (c), (d) ATAK and (e), (f) ATARK.

The ATAK method for downscaling was more performant than RK and ATARK statistically. Table 7 shows the mean value of the downscaled results. ATAK shows lower values of MAE 0.70 compared to RK and ATARK 1.93, 0.74. This may be because RK and ATARK could not capture the spatial distribution of methane emissions in Alaska as these techniques included covariates through regression. And since the regression model performed poorly, it affected the results.

Table 7: Validation result of downscaled methane data.

	Model	**MAE**	**CC**	**CH**
Mean	RK	1.93	0.96	0.98
Mean	ATARK	0.74	0.99	0.98
Mean	ATAK	0.70	0.99	0.99

7.3. Discussion on change observed in methane emissions over the years

Methane emissions vary during the monthly analysis as the summer season in Alaska starts from May to September. The observations are recorded mostly during these months, whereas for the remaining months, there are either no observations recorded or no data available (Table 8.) The pixel values with a min QA of 50 percent were considered as the pixel quality below this value is inaccurate. Due to this reason, the number of pixels recording methane emissions further reduced. The methane data show high emissions during the summer season, but it fails to capture the changing trends in these emissions over the recorded years. Firstly, the reason could be that the pixel ratio was significantly less to account for the changing yearly trends of monthly aggregated methane data. Secondly, to observe the changing trends, there has to be constant data (similar pixels) recorded over an area for comparison. Since the data recorded for the same months vary, it is challenging to conclude changes observed in methane emissions over different temporal aggregations.

Table 8: Observed versus predicted values for monthly averages of methane emissions in ppm.

Date	observed values	observed values	predicted values	predicted values
	min	max	min	max
Aug-18	1770.30	1845.04	1758.37	1850.76
Sep-18	1778.25	1852.40	1771.64	1848.23
Apr-19	1759.59	1822.49	1749.12	1853.87
May-19	1771.23	1837.77	1754.32	1846.52
Aug-19	1771.09	1850.28	1753.25	1857.17
May-20	1782.65	1846.19	1757.79	1882.17
Mar-21	1784.13	1873.86	1806.7	1868.98
May-21	1785.72	1839.30	1650.5	1907.83

Some of the tiles did not produce valid pixel values because the number of pixels within a tile was insufficient to produce promising results for downscaled prediction, as shown in Figure 19 for 2018. The remaining results are shown in *Appendix 5*. The tiles excluded while observing trend modeling are shown in Table 9.

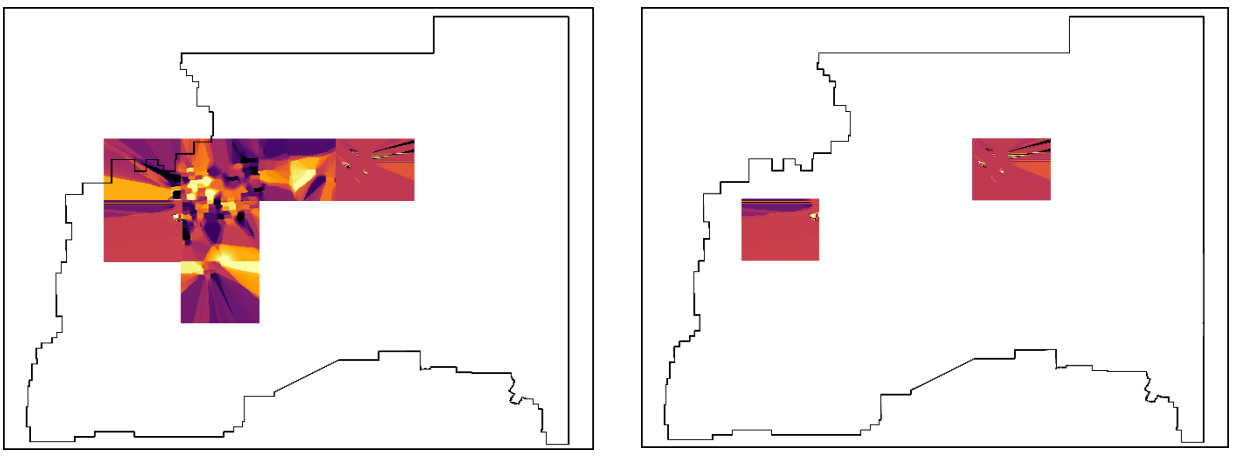

a **b**

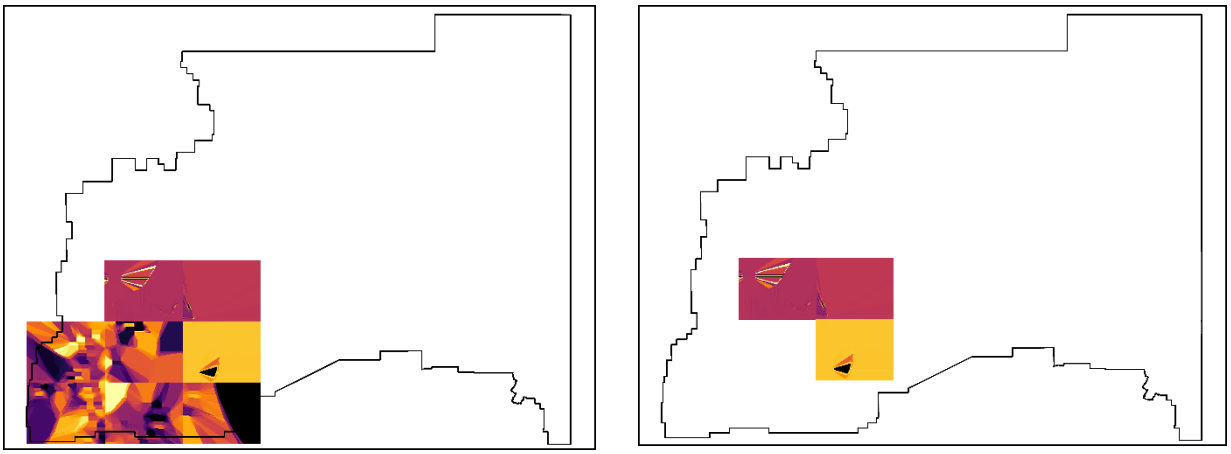

c d

Figure 19: August 2018 and September 2018 predictions (left) and excluded tiles (right).

Table 9: Rejected tiles after predictions.

Date	Tiles number
August 2018	20, 27
September 2018	31, 34, 38
April 2019	30, 35
May 2019	0, 6
August 2019	11, 20
May 2020	0, 13, 18, 24

7.4. Limitations

In this study, the downscaling approach was limited to land surface parameters such as LST, EVI, DEM, NDVI. The model performance could be improved by including other highly correlated fine-scale variables such as soil moisture, soil organic carbon, and precipitation (Sass et al., 1991; Zhang et al., 2011). However, due to limited satellite images, soil moisture data could not cover up the whole study area.

The downscaling results of methane emissions strongly depend on LST and NDVI (Zhang et al., 2011; Zhang et al., 2012). However, a major drawback of this study was the insufficient amount of methane recorded data. Due to the limited number of pixels, the relationship could not be captured between the dependent variable (methane) and the predictors (LSTDAY, LSTNIGHT, NDVI, DEM, EVI).

It is difficult to verify the accuracy of the covariates used for downscaling. The predictors could have brought the unknown error to downscaling results. The insufficient methane data limited the validation results. The satellite data used for cross-validation was captured at a resolution of 7 * 3.5 km^2, while the downscaled data products were estimated at 500 m that compromised the validation results (Elie, 2020).

The extent of the study area chosen for the research was large, and the operating system (RAM) processor was low. This added more computational time for calculating the inversed matrix for kriging and accuracy assessment indices using cross-validation, leading to a delay in the results.

8. CONCLUSION AND RECOMMENDATIONS

8.1. Conclusions

This study investigated downscaling of coarse-scale methane data over 22 variables and 51 datasets. The relationship was studied through multiple stepwise regression and the AIC index on open-source datasets. The use of stepwise regression and AIC helped in choosing the best combination of covariates and best-fit models. The study showed the existence of a weak but statistically significant relationship between methane data, LSTDAY, LSTNIGHT, NDVI, DEM, and EVI with adjusted R^2 reaching 0.29, as shown in Table 2. According to the findings, independent factors had no effect on methane emissions, resulting in unsatisfactory regression results and consequently unsuitable downscaling outcomes. The inclusion of covariates did not lead to improvement for the model. Among the three kriging techniques to downscale methane emissions assuming a non-stationary mean, ATAK gave slightly better results over the two tiles. There was a slight difference between the MAEs, CC, and CH for ATAK and ATARK but prominently for RK. The geostatistical downscaling method presented in this study can be applied to studies and areas with no ground measurement but with only open-source satellite data. In general, the downscaling scheme presented in the paper can be extended to other coarse resolution remote sensing data. The applicability of the suggested downscaling technique has been tested on only CH_4 TROPOMI data from August 2018 to May 2021. In the future, with increased data availability referring to the number of quality pixels recording methane emissions, more extensive experiments can be conducted. The impact of correlation strength between methane data and different auxiliary variables can be better studied with extensive recorded data.

What factors affect methane emissions change due to abrupt permafrost thawing through literature review and statistical relationship?

The study demonstrated a weak and statistically significant relationship existence between methane and predictors (LSTDAY, LSTNIGHT, NDVI, DEM, and EVI). Previous studies showed a significant relationship between NDVI and methane Zhang et al., (2011), and Zhang et al., (2012). Secondly, with LST and methane Zhang et al., (2011), depending upon their study area but this study shows different results. The highest correlation value reached up to 0.4 for LST DAY. Since no single variable could explain much of the variance, the integration of multiple predictors for the regression model was used. The correlation coefficient value of the predictors reached 0.29, which was a slight improvement however, not significant enough to explain the variance. Hence, none of the predictors helped in improving downscaled methane predictions through multiple regression analysis.

Which among the three statistical downscaling techniques is suitable for depicting methane emissions at the local level for small-scale study?

Statistical results show minor differences between ATAK and ATARK but notably for RK. Downscaling of methane data with auxiliary variables produced downscaling results that preserved not only local details but also varying overall patterns. ATAK shows slightly improved predictive performance compared to the downscaling with covariates. RK captured lower information for downscaled predictions.

What is the temporal variation in the magnitude of methane emissions?

The insufficient number of pixel information for mean monthly aggregated data over the summer season obstructs from making any conclusion about temporal changes in methane emissions with increasing global temperatures. What is noticeable is a seasonal shift in methane emissions from South-North-South again due to seasonal changes.

8.2. Recommendations

The simulations would be beneficial as it generates multiple alternative realizations while regenerating spatial patterns, unlike a single realization in kriging. Moreover, comparing multiple realizations can be used for modeling uncertainty about the unknown values at a fine scale (Park, 2013). In the future, the availability of high spatial-resolution data such as soil moisture, soil temperature, and precipitation can be included to evaluate their influence on methane estimation. Also, with extensive and constant data, this work could be extended to space-time kriging.

LIST OF REFERENCES

Adigi, Jacob Azumaana. (2019). Spatio-Temporal Regression Kriging for Predicting Rainfall From Sparse Precipitation Data in Ghana (Masters' thesis). Retrieved from https://essay.utwente.nl/83501/1/adigi.pdf

Anon. (2019). "MAE vs MSE vs RMSE." Retrieved from http://zerospectrum.com/2019/06/02/mae-vs-mse-vs-rmse/.

Anon. (2021). "USDA Natural Resources Conservation Service Soils." Retrieved from https://www.nrcs.usda.gov/wps/portal/nrcs/detailfull/soils/edu/?cid=STELPRDB1236841.

Apituley, Arnoud, Mattia Pedergnana, Maarten Sneep, J. Pepijn, Diego Loyola, and Otto Hasekamp. (2021). *Sentinel-5 Precursor/TROPOMI Level 2 Product User Manual Methane*.Retrieved from https://sentinel.esa.int/documents/247904/2474726/Sentinel-5P-Level-2-Product-User-Manual-Methane.pdf/1808f165-0486-4840-ac1d-06194238fa96.

Association, Canadian Permafrost. (2021). "Permafrost 101." Retrieved from https://canadianpermafrostassociation.ca/What-is-Permafrost.htm.

Atkinson, P. M., E. Pardo-Iguzquiza, and Mario Chica-Olmo. (2008). "Downscaling Cokriging for Super-Resolution Mapping of Continua in Remotely Sensed Images." *IEEE Transactions on Geoscience and Remote Sensing* 46(2),573-580. http://doi.org/: 10.1109/TGRS.2007.909952.

Atkinson, Peter M. (2013). "Downscaling in Remote Sensing." *International Journal of Applied Earth Observation and Geoinformation* 22(1),106-114. http://doi.org/10.1016/j.jag.2012.04.012.

Atkinson, Peter M., and Nicholas J. Tate. (2000). "Spatial Scale Problems and Geostatistical Solutions: A Review." *Professional Geographer* 52(4),607-623. http://doi.org/ 10.1111/0033-0124.00250.

Bubier, Jill L., Tim R. Moore, Lianne Bellisario, Neil T. Comer, and Patrick M. Crill. (1995). "Ecological Controls on Methane Emissions from a Northern Peatland Complex in the Zone of Discontinuous Permafrost, Manitoba, Canada." *Global Biogeochemical Cycles* 9(4),455-470. http://doi.org/ 10.1029/95GB02379.

Chen, Hsiang-Chieh, and Wen-June Wang. (2010). "Locally Edge-Adapted Distance for Image Interpolation Based on Genetic Fuzzy System." *Expert Systems with Applications* 37(1),288-297. http://doi.org/ 10.1016/j.eswa.2009.05.069.

Christensen, T. R., S. Jonasson, T. V. Callaghan, and M. Havström. (1995). "Spatial Variation in High-Latitude Methane Flux along a Transect across Siberian and European Tundra Environments." *Journal of Geophysical Research* 100(D10),21035. http://doi.org/ 10.1029/95JD02145.

Christensen, Torben R. (2004). "Thawing Sub-Arctic Permafrost: Effects on Vegetation and Methane Emissions." *Geophysical Research Letters* 31(4),L04501. http://doi.org/ 10.1029/2003GL018680.

Danielson, J.J., Gesch, D. B. (2011). *Global Multi-Resolution Terrain Elevation Data 2010 (GMTED2010)*. Retrieved from https://pubs.usgs.gov/of/2011/1073/.

Daoud, Jamal I. 2018. "Multicollinearity and Regression Analysis." in *Journal of Physics: Conference Series*. Vol. 949. Institute of Physics Publishing. Retrieved from https://iopscience.iop.org/article/10.1088/1742-6596/949/1/012009/meta.

Denchak, Melissa. (2018). "Permafrost: Everything You Need to Know." *NRDC*. Retrieved from https://www.nrdc.org/stories/permafrost-everything-you-need-know.

Didan, Kamel, Armando Barreto Munoz, Tucker J. Comptom, and Jorge E. Pinzon. (2018). *Suomi National Polar-Orbiting Partnership Visible Infrared Imaging Radiometer Suite Vegetation Index Product Suite User Guide & Abridged Algorithm Theoretical Basis Document*. Retrieved from https://lpdaac.usgs.gov/documents/184/VNP13_User_Guide_ATBD_V2.1.2.pdf.

Eastern Region Geography, Information Services. (2005). "Elevations and Distances."Retrieved from https://pubs.usgs.gov/gip/Elevations-Distances/elvadist.html.

Elder, Clayton D., David R. Thompson, Andrew K. Thorpe, Philip Hanke, Katey M. Walter Anthony, and Charles E. Miller. (2020). "Airborne Mapping Reveals Emergent Power Law of Arctic Methane Emissions." *Geophysical Research Letters. Vol* 47(3). http:/ /doi.org/ 10.1029/2019GL085707.

Elie, Byukusenge. (2020). Spatial Downscaling of Satellite Soil Moisture Utilising High-Resolution UAS Data over Alento Catchment in Italy (Masters' thesis). Retrieved from

https://library.itc.utwente.nl/login/2020/msc/wrem/byukusenge.pdf
Ezzine, Hicham, Ahmed Bouziane, Driss Ouazar, and Moulay Driss Hasnaoui. (2017). "Downscaling of Open Coarse Precipitation Data through Spatial and Statistical Analysis, Integrating NDVI, NDWI, Elevation, and Distance from Sea." *Advances in Meteorology* 2017. http:/ /doi.org/ 10.1155/2017/8124962.
Fairbanks, University of Alaska. (2004). "Welcome to SLED :: FAQ Alaska." Retrieved from https://web.archive.org/web/20070102180919/http://sled.alaska.edu/akfaq/aksuper.html#wea.
Frankenberg, C., J. F. Meirink, M. Van Weele, U. Platt, and T. Wagner. (2005). *Assessing Methane Emissions from Global Space-Borne Observations*. Vol. 308. American Association for the Advancement of Science. Retrieved from https://science.sciencemag.org/content/308/5724/1010.abstract.
Gao, Feng, William P. Kustas, and Martha C. Anderson. (2012). "A Data Mining Approach for Sharpening Thermal Satellite Imagery over Land." *Remote Sensing* 4(11),3287–3319. http://doi.org/ 10.3390/rs4113287.
Gido, Nureldin A. A., Mohammad Bagherbandi, Lars E. Sjöberg, and Robert Tenzer. (2019). "Studying Permafrost by Integrating Satellite and in Situ Data in the Northern High-Latitude Regions." *Acta Geophysica* 67(2),721–734. http://doi.org/ 10.1007/s11600-019-00276-4.
van der Gon, H. A. C. Denier, P. M. van Bodegom, S. Houweling, P. H. Verburg, and N. van Breemen. (2000). "Combining Upscaling and Downscaling of Methane Emissions from Rice Fields: Methodologies and Preliminary Results." Pp. 285–301 in *Methane Emissions from Major Rice Ecosystems in Asia*. Dordrecht: Springer, Dordrecht. Retrieved from https://link.springer.com/content/pdf/10.1007%2F978-94-010-0898-3.pdf.
González-Eguino, Mikel, and Marc B. Neumann. (2016). "Significant Implications of Permafrost Thawing for Climate Change Control." *Climatic Change* 136(2),381–388. http://doi.org/ 10.1007/s10584-016-1666-5.
Goovaerts, Pierre. (2008). "Kriging and Semivariogram Deconvolution in the Presence of Irregular Geographical Units." *Mathematical Geosciences* 40(1),101–128. http://doi.org/ 10.1007/s11004-007-9129-1.
Guo, Hua Dong, Li Zhang, and Lan Wei Zhu. (2015). "Earth Observation Big Data for Climate Change Research." *Advances in Climate Change Research* 6(2),108–117. http://doi.org/ 10.1016/j.accre.2015.09.007.
Hengl, Tomislav. (2007). *A Practical Guide to Geostatistical Mapping of Environmental Variables*. Retrieved from https://edepot.wur.nl/485517
Hengl, Tomislav, Gbm Heuvelink, and Alfred Stein. (2003). "Comparison of Kriging with External Drift and Regression-Kriging." *Technical Note, ITC* 17. http:/ /doi.org/ 10.1016/S0016-7061(00)00042-2.
Hengl, Tomislav, Gerard B. M. Heuvelink, and David G. Rossiter. (2007). "About Regression-Kriging: From Equations to Case Studies." *Computers and Geosciences* 33(10),1301–1315. http://doi.org/ 10.1016/j.cageo.2007.05.001.
Hu, Maogui, and Yanwei Huang. (2020). "Atakrig: An R Package for Multivariate Area-to-Area and Area-to-Point Kriging Predictions." *Computers and Geosciences* 139,104471. http://doi.org/ 10.1016/j.cageo.2020.104471.
Hull, Teresa, and Linda Leask. (2007). "Alaska Review of Social and Econmic Conditions." 32(1),536–538. Retrieved from https://www.arlis.org/docs/vol1/B/54838963.pdf.
Hutmacher, Matthew M., and Kenneth G. Kowalski. 2015. "Covariate Selection in Pharmacometric Analyses: A Review of Methods." *British Journal of Clinical Pharmacology* 79(1),132–147. http://doi.org/ 10.1111/bcp.12451.
In P. Katila, C. Pierce Colfer, W. De Jong, G. Galloway, P. Pacheco, &. G. Winkel. (2019). *Sustainable Development Goals: Their Impacts on Forests and People*. edited by P. Katila, C. J. Pierce Colfer, W. de Jong, G. Galloway, P. Pacheco, and G. Winkel. Cambridge University Press. Retrieved from https://doi.org/10.1017/9781108765015.
Isaksen, Ivar, Terje Berntsen, Stig Dalsøren, Kostas Eleftheratos, Yvan Orsolini, Bjørg Rognerud, Frode Stordal, Ole Søvde, Christos Zerefos, and Chris Holmes. (2014). "Atmospheric Ozone and Methane in a Changing Climate." *Atmosphere* 5(3),518–535. http://doi.org/ 10.3390/atmos5030518.
Jin, Yan, Yong Ge, Jianghao Wang, Gerard B. M. Heuvelink, and Le Wang. (2018). "Geographically Weighted Area-to-Point Regression Kriging for Spatial Downscaling in Remote Sensing." *Remote Sensing* 10(4),579. http://doi.org/ 10.3390/rs10040579.

Jorgenson, M. Torre, Yuri L. Shur, and Erik R. Pullman. (2006). "Abrupt Increase in Permafrost Degradation in Arctic Alaska." *Geophysical Research Letters* 33(2),L02503. http://doi.org/ 10.1029/2005GL024960.

Kassambara. (2018). "Nonlinear Regression Essentials in R: Polynomial and Spline Regression Models." Retrieved from http://www.sthda.com/english/articles/40-regression-analysis/162-nonlinear-regression-essentials-in-r-polynomial-and-spline-regression-models/.

Kirschke, Stefanie, Philippe Bousquet, Philippe Ciais, Marielle Saunois, Josep G. Canadell, Edward J. Dlugokencky, Peter Bergamaschi, Daniel Bergmann, Donald R. Blake, Lori Bruhwiler, Philip Cameron-Smith, Simona Castaldi, Frédéric Chevallier, Liang Feng, Annemarie Fraser, Martin Heimann, Elke L. Hodson, Sander Houweling, Béatrice Josse, Paul J. Fraser, Paul B. Krummel, Jean François Lamarque, Ray L. Langenfelds, Corinne Le Quéré, Vaishali Naik, Simon O'doherty, Paul I. Palmer, Isabelle Pison, David Plummer, Benjamin Poulter, Ronald G. Prinn, Matt Rigby, Bruno Ringeval, Monia Santini, Martina Schmidt, Drew T. Shindell, Isobel J. Simpson, Renato Spahni, L. Paul Steele, Sarah A. Strode, Kengo Sudo, Sophie Szopa, Guido R. Van Der Werf, Apostolos Voulgarakis, Michiel Van Weele, Ray F. Weiss, Jason E. Williams, and Guang Zeng. (2013). "Three Decades of Global Methane Sources and Sinks." *Nature Geoscience* 6(10),813–823. http://doi.org/ 10.1038/ngeo1955.

Kitanidis, Peter K. (1993). "Generalized Covariance Functions in Estimation." *Mathematical Geology* 25(5),525–540. http://doi.org/ 10.1007/BF00890244.

Kohnert, Katrin, Andrei Serafimovich, Stefan Metzger, Jörg Hartmann, and Torsten Sachs. (2017). "Strong Geologic Methane Emissions from Discontinuous Terrestrial Permafrost in the Mackenzie Delta, Canada." *Scientific Reports* 7(1),5828. http://doi.org/ 10.1038/s41598-017-05783-2.

Kumari, Madhuri, Chander Kumar Singh, Ashoke Basistha, Singay Dorji, and Tayba Buddha Tamang. (2017). "Non-Stationary Modelling Framework for Rainfall Interpolation in Complex Terrain." *International Journal of Climatology* 37(11),4171–4185. http://doi.org/ 10.1002/joc.5057.

Kwak, Geun-Ho, No-Wook Park, and Phaedon Kyriakidis. (2018). "Development of an R-Based Spatial Downscaling Tool to Predict Fine Scale Information from Coarse Scale Satellite Products." *Korean Journal of Remote Sensing* 34(1),89–99. https://doi.org/10.7780/kjrs.2018.34.1.6.

Kyriakidis, Phaedon C. (2004). "A Geostatistical Framework for Area-to-Point Spatial Interpolation." *Geographical Analysis* 36(3),259–289. http://doi.org/ 10.1111/j.1538-4632.2004.tb01135.x.

Kyriakidis, Phaedon C., and Eun-Hye Yoo. (2005). "Geostatistical Prediction and Simulation of Point Values from Areal Data." *Geographical Analysis* 37(2),124–151. http://doi.org/ 10.1111/j.1538-4632.2005.00633.x.

Landgraf, Jochen, Alba Lorente, Bavo Langerock, and Mahesh Kumar Sha BIRA-. (2021). *S5P Mission Performance Centre Methane [L2__CH4___] Readme*. Retrieved from https://sentinel.esa.int/documents/247904/3541451/Sentinel-5P-Methane-Product-Readme-File.

League, Alaska Municipal. (2021). *Alaska Municipal League Alaskan Local Government Primer*. Retrieved from http://www.akml.org/wp-content/uploads/2014/02/Legislative-PRIMER-WEB.pdf.

Liu, X. H., P. C. Kyriakidis, and M. F. Goodchild. (2008). "Population-Density Estimation Using Regression and Area-to-Point Residual Kriging." *International Journal of Geographical Information Science* 22(4),431–447. http://doi.org/ 10.1080/13658810701492225.

Memarsadeghi, Nargess, Jacqueline Le Moigne, David M. Mount, and Jeffrey Morisette. (2005). "A New Approach to Image Fusion Based on Cokriging." Pp. 622–629 in *2005 7th International Conference on Information Fusion, FUSION*. Vol. 1. IEEE. http://doi.org/10.1109/ICIF.2005.1591912

Meul, M., and M. Van Meirvenne. (2003). "Kriging Soil Texture under Different Types of Nonstationarity." Pp. 217–233 in *Geoderma*. Vol. 112. Elsevier. http://doi.org/10.1016/S0016-7061(02)00308-7

Mukaka, M. M. (2012). "Statistics Corner: A Guide to Appropriate Use of Correlation Coefficient in Medical Research." *Malawi Medical Journal : The Journal of Medical Association of Malawi* 24(3),69–71. Retrieved from https://www.ncbi.nlm.nih.gov/pmc/articles/PMC3576830/.

Mukherjee, Sandip, Pawan Kumar Joshi, and Rahul Dev Garg. (2015). "Regression-Kriging Technique to Downscale Satellite-Derived Land Surface Temperature in Heterogeneous Agricultural Landscape." *IEEE Journal of Selected Topics in Applied Earth Observations and Remote Sensing* 8(3),1–1. http://doi.org/ 10.1109/JSTARS.2015.2396032.

Natali, Susan M., John P. Holdren, Brendan M. Rogers, Rachael Treharne, Philip B. Duffy, Rafe

Pomerance, and Erin MacDonald. (2021). "Permafrost Carbon Feedbacks Threaten Global Climate Goals." *Proceedings of the National Academy of Sciences of the United States of America* 118(21). http:/ /doi.org/ 10.1073/pnas.2100163118.
National Association of Counties. (2013). "Find A County." *NACo*. Retrieved from https://archive.is/20130416102355/http://www.uscounties.org/cffiles_web/counties/state.cfm?statecode=ak.
National Snow and Ice Data Center. (2020). "All About Frozen Ground." *National Snow and Ice Data Center*. Retrieved from https://nsidc.org/cryosphere/frozenground/index.html.
Northwest Alliance for Computational Science and Engineering, NACSE. (2021). "PRISM Climate Group." Retrieved from https://prism.oregonstate.edu/projects/alaska.php.
Oberle, Ferdinand K. J., Ann E. Gibbs, Bruce M. Richmond, Li H. Erikson, Mark P. Waldrop, and Peter W. Swarzenski. (2019). "Towards Determining Spatial Methane Distribution on Arctic Permafrost Bluffs with an Unmanned Aerial System." *SN Applied Sciences* 1(3),236. http://doi.org/ 10.1007/s42452-019-0242-9.
Odeh, I. O. A., A. B. McBratney, and D. J. Chittleborough. (1995). "Further Results on Prediction of Soil Properties from Terrain Attributes: Heterotopic Cokriging and Regression-Kriging." *Geoderma* 67(3–4),215–226. http://doi.org/ 10.1016/0016-7061(95)00007-B.
Olefeldt, David, Merritt R. Turetsky, Patrick M. Crill, and A. David Mcguire. (2013). "Environmental and Physical Controls on Northern Terrestrial Methane Emissions across Permafrost Zones." *Global Change Biology* 19(2),589–603. http://doi.org/ 10.1111/gcb.12071.
Pachauri, Rajendra K., Leo Meyer, Stephane Hallegatte France, World Bank, Gabriele Hegerl, Sander Brinkman, Line van Kesteren, Noëmie Leprince-Ringuet, and Fijke van Boxmeer. (2014). *Climate Change 2014 Synthesis Report*. Gian-Kasper Plattner. Retrieved from https://www.ipcc.ch/site/assets/uploads/2018/02/SYR_AR5_FINAL_full.pdf.
Pardo-Igúzquiza, Eulogio, Mario Chica-Olmo, and Peter M. Atkinson. (2006). "Downscaling Cokriging for Image Sharpening." *Remote Sensing of Environment* 102(1–2),86–98. http://doi.org/ 10.1016/j.rse.2006.02.014.
Park, No Wook. 2013. "Spatial Downscaling of TRMM Precipitation Using Geostatistics and Fine Scale Environmental Variables." *Advances in Meteorology* (2013). http://doi.org/ 10.1155/2013/237126.
Piazza, Annalisa, Francesco Conti, Francesco Viola, Emanuele Eccel, and Leonardo Noto. (2015). "Comparative Analysis of Spatial Interpolation Methods in the Mediterranean Area: Application to Temperature in Sicily." *Water* 7(12),1866–1888. http://doi.org/ 10.3390/w7051866.
Qingbai, Wu, and Liu Yongzhi. (2004). "Ground Temperature Monitoring and Its Recent Change in Qinghai-Tibet Plateau." *Cold Regions Science and Technology* 38(2–3),85–92. http://doi.org/ 10.1016/S0165-232X(03)00064-8.
Rashid, Kashif, Andrew Speck, Timothy P. Osedach, Dominic V. Perroni, and Andrew E. Pomerantz. (2020). "Optimized Inspection of Upstream Oil and Gas Methane Emissions Using Airborne LiDAR Surveillance." *Applied Energy* 275,115327. http://doi.org/ 10.1016/j.apenergy.2020.115327.
Rasmus E Benestad, Deliang Chen, Inger Hanssen-bauer. (2008). "Empirical-Statistical Downscaling." *World Scientific Publishing Company*. Retrieved from https://books.google.nl/books?hl=en&lr=&id=WxM8DQAAQBAJ&oi=fnd&pg=PR5&dq=statistical+downscaling+&ots=5bquMA9DGG&sig=JxV_KMwOgVwVznUMjiGNk6HeoG8#v=onepage&q=statistical downscaling&f=false.
Rata, Mohamed, Abdelkader Douaoui, Mohamed Larid, and Ahmed Douaik. (2020). "Comparison of Geostatistical Interpolation Methods to Map Annual Rainfall in the Chéliff Watershed, Algeria." *Theoretical and Applied Climatology* 141(3–4),1009–1024. http:/ /doi.org/ 10.1007/s00704-020-03218-z.
Reuder, Joachim, Marius O. Jonassen, and Haraldur Ólafsson. (2012). "The Small Unmanned Meteorological Observer SUMO: Recent Developments and Applications of a Micro-UAS for Atmospheric Boundary Layer Research." *Acta Geophysica* 60(5),1454–1473. http://doi.org/ 10.2478/s11600-012-0042-8.
Ribeiro Sales, Marcio H., Carlos M. Souza, and Phaedon C. Kyriakidis. (2013). "Fusion of MODIS Images Using Kriging with External Drift." *IEEE Transactions on Geoscience and Remote Sensing* 51(4),2250–2259. http://doi.org/ 10.1109/TGRS.2012.2208467.
Romanovsky, V., M. Burgess, S. Smith, K. Yoshikawa, and J. Brown. (2002). "Permafrost Temperature Records: Indicators of Climate Change." *Eos, Transactions American Geophysical Union* 83(50),589.

http://doi.org/ 10.1029/2002EO000402.
Rossi, Richard E., Jennifer L. Dungan, and Louisa R. Beck. (1994). "Kriging in the Shadows: Geostatistical Interpolation for Remote Sensing." *Remote Sensing of Environment* 49(1),32–40. http://doi.org/ 10.1016/0034-4257(94)90057-4.
Sabine, C, G Bala, L Bopp, V. Brovkin, J. Canadell, A. Chhabra, R. DeFries, J. Galloway, M. Heimann, C. Jones, C. Le Quéré, RB Myneni, S. Piao, P. Thornton, D. Qin, G-k Plattner, M. Tignor, SK Allen, J. Boschung, A. Nauels, Y. Xia, V. Bex, PM Midgley, Philippe Ciais, Christopher Sabine, Govindasamy Bala, Laurent Bopp, and Victor Brovkin Germany. (2014). *Carbon and Other Biogeochemical Cycles. In Climate Change 2013: The Physical Science Basis. Contribution of Working Group I to the Fifth Assessment Report of the Intergovernmental Panel on Climate Change*. Cambridge University Press.Retrieved from https://pure.mpg.de/rest/items/item_2058766/component/file_2058769/content.
Samuel Rieger, Dale B. Schoephorster, Clarence E. Furbush, Soil Conservation Service.(1979). *Exploratory Soil Survey of Alaska*. US Department of Agriculture, Soil Conservation Service. Retrieved from https://www.nrcs.usda.gov/Internet/FSE_MANUSCRIPTS/alaska/AK_exploratory1979/alaska.pdf.
Sass, R. L., F. M. Fisher, F. T. Turner, and M. F. Jund. (1991). "Methane Emission from Rice Fields as Influenced by Solar Radiation, Temperature, and Straw Incorporation." *Global Biogeochemical Cycles* 5(4),335–350. http://doi.org/ 10.1029/91GB02586.
Schaefer, Kevin, Hugues Lantuit, Vladimir E. Romanovsky, Edward A. G. Schuur, and Ronald Witt. (2014). "The Impact of the Permafrost Carbon Feedback on Global Climate." *Environmental Research Letters* 9(8),085003. http://doi.org/ 10.1088/1748-9326/9/8/085003.
Schneising, Oliver, Michael Buchwitz, Maximilian Reuter, Jens Heymann, Heinrich Bovensmann, and John P. Burrows. 2011. "Long-Term Analysis of Carbon Dioxide and Methane Column-Averaged Mole Fractions Retrieved from SCIAMACHY." *Atmospheric Chemistry and Physics* 11(6),2863–2880. http://doi.org/ 10.5194/acp-11-2863-2011.
Schuur, Edward A. G., James Bockheim, Josep G. Canadell, Eugenie Euskirchen, Christopher B. Field, Sergey V. Goryachkin, Stefan Hagemann, Peter Kuhry, Peter M. Lafleur, Hanna Lee, Galina Mazhitova, Frederick E. Nelson, Annette Rinke, Vladimir E. Romanovsky, Nikolay Shiklomanov, Charles Tarnocai, Sergey Venevsky, Jason G. Vogel, and Sergei A. Zimov. (2008). "Vulnerability of Permafrost Carbon to Climate Change: Implications for the Global Carbon Cycle." *BioScience* 58(8),701–714. http://doi.org/ 10.1641/B580807.
Serikova, S., O. S. Pokrovsky, H. Laudon, I. V. Krickov, A. G. Lim, R. M. Manasypov, and J. Karlsson. (2019). "High Carbon Emissions from Thermokarst Lakes of Western Siberia." *Nature Communications* 10(1),1552. http://doi.org/ 10.1038/s41467-019-09592-1.
Takeuchi, Wataru, Masayuki Tamura, and Yoshifumi Yasuoka. (2003). "Estimation of Methane Emission from West Siberian Wetland by Scaling Technique between NOAA AVHRR and SPOT HRV." *Remote Sensing of Environment* 85(1),21–29. http://doi.org/ 10.1016/S0034-4257(02)00183-9.
Tamocai, C., J. G. Canadell, E. A. G. Schuur, P. Kuhry, G. Mazhitova, and S. Zimov. (2009). "Soil Organic Carbon Pools in the Northern Circumpolar Permafrost Region." *Global Biogeochemical Cycles* 23(2). http://doi.org/ 10.1029/2008GB003327.
Tang, Yunwei, Peter M. Atkinson, and Jingxiong Zhang. (2015). "Downscaling Remotely Sensed Imagery Using Area-to-Point Cokriging and Multiple-Point Geostatistical Simulation." *ISPRS Journal of Photogrammetry and Remote Sensing* 101,174–185. http:/ doi.org/ 10.1016/j.isprsjprs.2014.12.016.
Thorpe, Andrew K., Dar A. Roberts, Eliza S. Bradley, Christopher C. Funk, Philip E. Dennison, and Ira Leifer. (2013). "High Resolution Mapping of Methane Emissions from Marine and Terrestrial Sources Using a Cluster-Tuned Matched Filter Technique and Imaging Spectrometry." *Remote Sensing of Environment* 134,305–318. http://doi.org/ 10.1016/j.rse.2013.03.018.
Turner, A. J., D. J. Jacob, J. Benmergui, S. C. Wofsy, J. D. Maasakkers, A. Butz, O. Hasekamp, and S. C. Biraud. (2016). "A Large Increase in U.S. Methane Emissions over the Past Decade Inferred from Satellite Data and Surface Observations." *Geophysical Research Letters* 43(5),2218–2224. http://doi.org/ 10.1002/2016GL067987.
UNFCCC. (2021a). "The Paris Agreement." *United Nations Framework Convention on Climate Change*. Retrieved from https://unfccc.int/process-and-meetings/the-paris-agreement/the-paris-agreement.
UNFCCC. (2021b). "Why Methane Matters." *United Nations Framework Convention on Climate Change*.

Retrieved from https://unfccc.int/news/new-methane-signs-underline-urgency-to-reverse-emissions.
Villa, Tommasofrancesco, Felipe Gonzalez, Branka Miljievic, Zoran Ristovski, and Lidia Morawska. (2016). "An Overview of Small Unmanned Aerial Vehicles for Air Quality Measurements: Present Applications and Future Prospectives." *Sensors* 16(7),1072. http://doi.org/ 10.3390/s16071072.
Walter, K. M., S. A. Zimov, J. P. Chanton, D. Verbyla, and F. S. Chapin. (2006). "Methane Bubbling from Siberian Thaw Lakes as a Positive Feedback to Climate Warming." *Nature* 443(7107),71–75. http://doi.org/ 10.1038/nature05040.
Wan, Zhengming. (2013). *Collection-6 MODIS Land Surface Temperature Products Users' Guide*. Retrieved from https://lpdaac.usgs.gov/documents/118/MOD11_User_Guide_V6.pdf.
Wang, Qunming, Victor Rodriguez-Galiano, and Peter M. Atkinson. 2017. "Geostatistical Solutions for Downscaling Remotely Sensed Land Surface Temperature." *International Archives of the Photogrammetry, Remote Sensing and Spatial Information Sciences - ISPRS Archives* 42(2W7). http://doi.org/ 10.5194/isprs-archives-XLII-2-W7-913-2017.
Wang, Qunming, Wenzhong Shi, and Peter M. Atkinson. (2016). "Area-to-Point Regression Kriging for Pan-Sharpening." *ISPRS Journal of Photogrammetry and Remote Sensing* 114,151–165. http://doi.org/ 10.1016/j.isprsjprs.2016.02.006.
Wang, Qunming, Wenzhong Shi, Peter M. Atkinson, and Eulogio Pardo-Igúzquiza.(2016). "A New Geostatistical Solution to Remote Sensing Image Downscaling." *IEEE TRANSACTIONS ON GEOSCIENCE AND REMOTE SENSING* 54(1). http://doi.org/ 10.1109/TGRS.2015.2457672.
Wang, Qunming, Wenzhong Shi, Peter M. Atkinson, and Yuanling Zhao. (2015). "Downscaling MODIS Images with Area-to-Point Regression Kriging." *Remote Sensing of Environment* 166,191–204. http://doi.org/ 10.1016/j.rse.2015.06.003.
Weatherbase. (2021). "United States of America Travel Weather Averages." Retrieved from http://www.weatherbase.com/weather/city.php3?c=US&s=AK&statename=Alaska-United-States-of-America.
Wei, Shiping, Hongpeng Cui, Youhai Zhu, Zhenquan Lu, Shouji Pang, Shuai Zhang, Hailiang Dong, and Xin Su. (2018). "Shifts of Methanogenic Communities in Response to Permafrost Thaw Results in Rising Methane Emissions and Soil Property Changes." *Extremophiles* 22(3),447–459. http://doi.org/ 10.1007/s00792-018-1007-x.
Welch, Craig. (2019). "Arctic Permafrost Is Thawing Fast. That Affects Us All." *National Geographic*. Retrieved from https://www.nationalgeographic.com/environment/2019/08/arctic-permafrost-is-thawing-it-could-speed-up-climate-change-feature/.
Whalen, Stephen C., and William S. Reeburgh. (1992). "Interannual Variations in Tundra Methane Emission: A 4-Year Time Series at Fixed Sites." *Global Biogeochemical Cycles* 6(2),139–159. http://doi.org/ 10.1029/92GB00430.
Wik, Martin, Ruth K. Varner, Katey Walter Anthony, Sally MacIntyre, and David Bastviken. (2016). "Climate-Sensitive Northern Lakes and Ponds Are Critical Components of Methane Release." *Nature Geoscience* 9(2),99–105. http://doi.org/ 10.1038/ngeo2578.
Wolf, Julie, Ghassem R. Asrar, and Tristram O. West. (2017). "Revised Methane Emissions Factors and Spatially Distributed Annual Carbon Fluxes for Global Livestock." *Carbon Balance and Management* 12(1),16. http://doi.org/ 10.1186/s13021-017-0084-y.
Xue, Xian, Jian Guo, Bangshuai Han, Qingwei Sun, and Lichao Liu. (2009). "The Effect of Climate Warming and Permafrost Thaw on Desertification in the Qinghai-Tibetan Plateau." *Geomorphology* 108(3–4),182–190. http://doi.org/ 10.1016/j.geomorph.2009.01.004.
Yawitz, Dan. (2012). "Report Says IPCC Needs to Address Melting Permafrost." *Climate Central*. Retrieved from https://www.climatecentral.org/news/report-says-ipcc-needs-to-address-impact-of-melting-permafrost-15291.
Yoshikawa, Kenji, Mikhail Kanevskiy, Y. L. Shur, and Vladimir E. Romanovsky. (2008). *Permafrost Characteristics of Alaska*. Vol. 3. Retrieved from https://www.researchgate.net/profile/Sergey-Marchenko-3/publication/334524021_Permafrost_Characteristics_of_Alaska_Map/links/5d2f7672a6fdcc2462e86fae/Permafrost-Characteristics-of-Alaska-Map.pdf.
Yvon-Durocher, Gabriel, Andrew P. Allen, David Bastviken, Ralf Conrad, Cristian Gudasz, Annick St-Pierre, Nguyen Thanh-Duc, and Paul A. Del Giorgio. (2014). "Methane Fluxes Show Consistent

Temperature Dependence across Microbial to Ecosystem Scales." *Nature* 507(7493),488–491. http://doi.org/ 10.1038/nature13164.

Zarei, A., M. Masihi, and K. Salahshoor. (2011). "Comparison of Different Univariate and Multivariate Geostatistical Methods by Porosity Modeling of an Iranian Oil Field." *Petroleum Science and Technology* 29(19),2061–2076. http://doi.org/ 10.1080/10916461003681703.

Zhang, C., W. Li, and D. Travis. (2007). "Gaps-fill of SLC-off Landsat ETM+ Satellite Image Using a Geostatistical Approach." *International Journal of Remote Sensing* 28(22),5103–5122. http://doi.org/ 10.1080/01431160701250416.

Zhang, Xiuying, Hong Jiang, Yueqi Wang, Ying Han, M. Buchwitz, O. Schneising, and J. P. Burrows. (2011). "Spatial Variations of Atmospheric Methane Concentrations in China." *International Journal of Remote Sensing* 32(3),833–847. http://doi.org/ 10.1080/01431161.2010.517804.

Zhang, Xiuying, Hong Jiang, Guomo Zhou, Zhongyong Xiao, and Zhen Zhang. (2012). "Geostatistical Interpolation of Missing Data and Downscaling of Spatial Resolution for Remotely Sensed Atmospheric Methane Column Concentrations." *International Journal of Remote Sensing* 33(1),120–134. http://doi.org/ 10.1080/01431161.2011.584078.

Zhang, Zhen, Niklaus E. Zimmermann, Andrea Stenke, Xin Li, Elke L. Hodson, Gaofeng Zhu, Chunlin Huang, and Benjamin Poulter. (2017). "Emerging Role of Wetland Methane Emissions in Driving 21st Century Climate Change." *Proceedings of the National Academy of Sciences of the United States of America* 114(36),9647–9652. http://doi.org/ 10.1073/pnas.1618765114.

Zimov, Sergey A., Edward A. G. Schuur, and F. Stuart Chapin. (2006). "CLIMATE CHANGE: Permafrost and the Global Carbon Budget." *Science* 312(5780),1612–1613. http://doi.org/ 10.1126/science.1128908.

APPENDICES

Appendix 1. Tile-wise deconvolution from August 2018-May 2021

Data Name	Band Name	Description	Source	Spatial Resolution	Resampled Resolution	Temporal Resolution	Type
Sentinel-5P L2	CH_4	Methane emissions with QA value of above 50%	https://apps.sentinel-hub.com/	7*3.5 km and 5.5*3.5km	7*3.5 km and 5.5*3.5km	1 day	Raster
Sentinel-3 SLSTR L1B	S1	Vegetation monitoring	https://apps.sentinel-hub.com/	500 m	500m	< 0.9days	Raster
Sentinel-3 SLSTR L1B	S2	Normalized Differential vegetation Index (NDVI), Vegetation monitoring	https://apps.sentinel-hub.com/	500 m	500m	< 0.9days	Raster
Sentinel-3 SLSTR L1B	S3	NDVI	https://apps.sentinel-hub.com/	500 m	500m	< 0.9days	Raster
Sentinel-3 SLSTR L1B	S5	Vegetation monitoring	https://apps.sentinel-hub.com/	500 m	500m	< 0.9days	Raster
Sentinel-3 SLSTR L1B	S6	Vegetation state	https://apps.sentinel-hub.com/	500 m	500m	< 0.9days	Raster
Sentinel-3 SLSTR L1B	S7	Land surface temperature (LST)	https://apps.sentinel-hub.com/	1000 m	500m	< 0.9days	Raster
Sentinel-3 SLSTR L1B	S8	LST	https://apps.sentinel-hub.com/	1000 m	500m	< 0.9days	Raster
Sentinel-3 SLSTR L1B	S9	LST	https://apps.sentinel-hub.com/	1000 m	500m	12days	Raster
Sentinel1	Derived SMI	Soil moisture	https://apps.sentinel-hub.com/	10, 25, 40 m	500m	< 0.9days	Raster
Landsat8	B10	Brightness	https://cod	30m	500m	16days	Raster

		temperature (BT)	e.earthengine.google.com/				
Landsat8	B11	BT	https://code.earthengine.google.com/	30m	500m	16days	Raster
Landsat8	Derived datasets	Enhanced vegetation Index (EVI)	https://code.earthengine.google.com/	30m	500m	8days	Raster
Landsat8	Derived datasets	NDVI	https://code.earthengine.google.com/	30m	500m	8days	Raster
Landsat8	Derived datasets	Normalized difference water Index (NDWI)	https://code.earthengine.google.com/	30m	500m	8days	Raster
Landsat8	Derived datasets	Normalized difference water Index (NDWI)	https://code.earthengine.google.com/	30m	500m	8days	Raster
Landsat8	Derived datasets	Normalized difference water Index (NDWI)	https://code.earthengine.google.com/	30m	500m	8days	Raster
Landsat7	B6	BT	https://code.earthengine.google.com/	30m	500m	16days	Raster
Landsat7	Derived datasets	EVI	https://code.earthengine.google.com/	30m	500m	8days	Raster
Landsat7	Derived datasets	NDVI	https://code.earthengine.google.com/	30m	500m	8days	Raster
Landsat7	Derived datasets	NDWI	https://code.earthengine.google.com/	30m	500m	8days	Raster
MODIS 11A1.006	LST_day_1km	LST	https://code.earthengin	1000m	500m	Daily	Raster

			e.google.com/				
MODIS 11A1.006	LST_Night_1km	LST	https://code.earthengine.google.com/	1000m	500m	Daily	Raster
MODIS 11A1.006	Emis_31	Emissivity	https://code.earthengine.google.com/	1000m	500m	Daily	Raster
MODIS 11A1.006	Emis_32	Emissivity	https://code.earthengine.google.com/	1000m	500m	Daily	Raster
MODIS 11A2.006	LST_day_1km	LST	https://code.earthengine.google.com/	1000m	500m	8days	Raster
MODIS 11A2.006	LST_Night_1km	LST	https://code.earthengine.google.com/	1000m	500m	8days	Raster
MODIS 11A2.006	Emis_31	Emissivity	https://code.earthengine.google.com/	1000m	500m	8days	Raster
MODIS 11A2.006	Emis_32	Emissivity	https://code.earthengine.google.com/	1000m	500m	8days	Raster
MODIS MCD15A3H.006	FPAR	Fraction of Photosynthetically Active Radiation	https://code.earthengine.google.com/	500m	500m	4days	Raster
MODIS MCD15A3H.006	LAI	Leaf Area Index	https://code.earthengine.google.com/	500m	500m	4days	Raster
MODIS MOD16A2.006	ET	Total evapotranspiration	https://code.earthengine.google.com/	500m	500m	8days	Raster
MODIS MOD16A2.006	LE	Average latent heat flux	https://code.earthengine.google.co	500m	500m	8days	Raster

			m/				
MODIS MOD16A 2.006	PET	Total potential evapotranspiration	https://code.earthengine.google.com/	500m	500m	8days	Raster
MODIS MOD16A 2.006	PLE	Average potential latent heat flux	https://code.earthengine.google.com/	500m	500m	8days	Raster
VNP13A 1: VIIRS	NDVI	NDVI	https://code.earthengine.google.com/	500m	500m	16days	Raster
VNP13A 1: VIIRS	EVI	EVI	https://code.earthengine.google.com/	500m	500m	16days	Raster
VNP13A 1: VIIRS	EVI2	EVI	https://code.earthengine.google.com/	500m	500m	16days	Raster
MOD13A 1.006 NDVI	NDVI &EVI	NDVI & EVI	https://developers.google.com/earth-engine/datasets/catalog/MODIS_006_MOD13A1	500m	500m	16days	Raster
MODIS13A2.006 NDVI	NDVI &EVI	NDVI & EVI	https://developers.google.com/earth-engine/datasets/catalog/MODIS_006_MOD13A2	1000m	500m	16days	Raster
MODIS13Q1.006	NDVI &EVI	NDVI & EVI	https://developers.google.com/earth-engine/datasets/catalog	250m	500m	16days	Raster

			/MODIS_006_MOD13Q1				
GMTED 2010 DEM	Height	Elevation of ground	https://developers.google.com/earth-engine/datasets/catalog/USGS_GMTED2010#description	7.5arc seconds/ 250m	500m		Raster
Slope				7.5arc seconds/ 250m	500m		Raster
Aspect				7.5arc seconds/ 250m	500m		Raster
Direct radiation				7.5arc seconds/ 250m	500m		Raster
Surface roughness				7.5arc seconds/ 250m	500m		Raster
Solar radiation				7.5arc seconds/ 250m	500m		Raster
Diffuse radiation				7.5arc seconds/ 250m	500m		Raster
Direct duration				7.5arc seconds/ 250m	500m		Raster
Permafrost extent			https://nsidc.org/data/ggd318#				Shapefile

Appendix 2. Tile-wise deconvolution from August 2018-May 2021.

August 2018

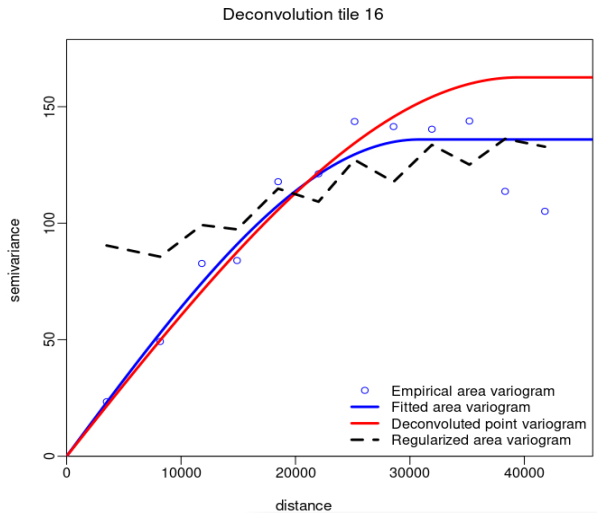

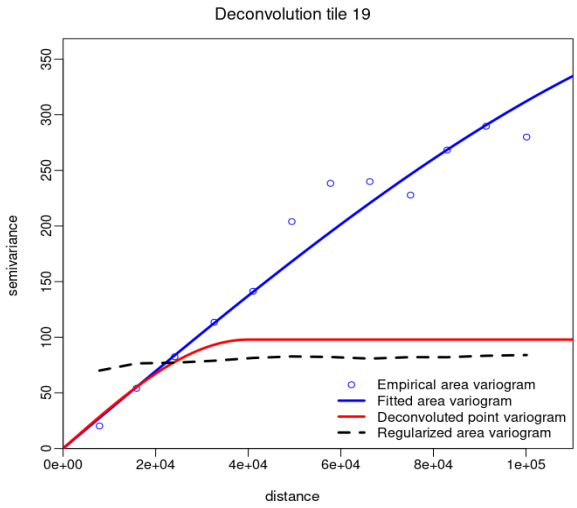

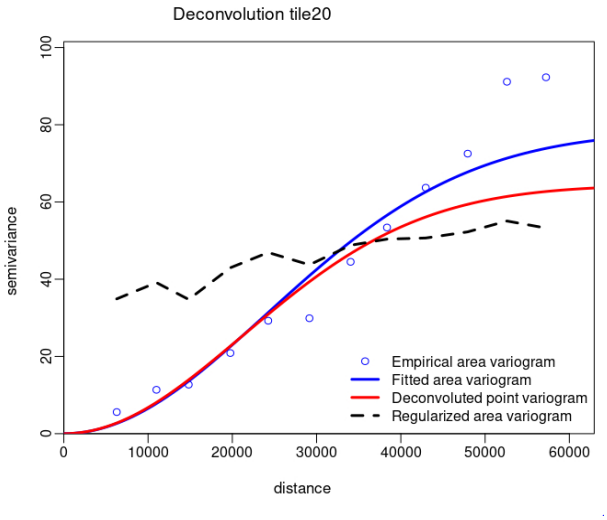

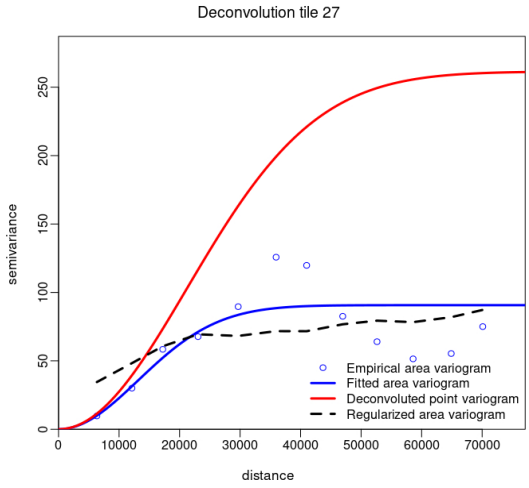

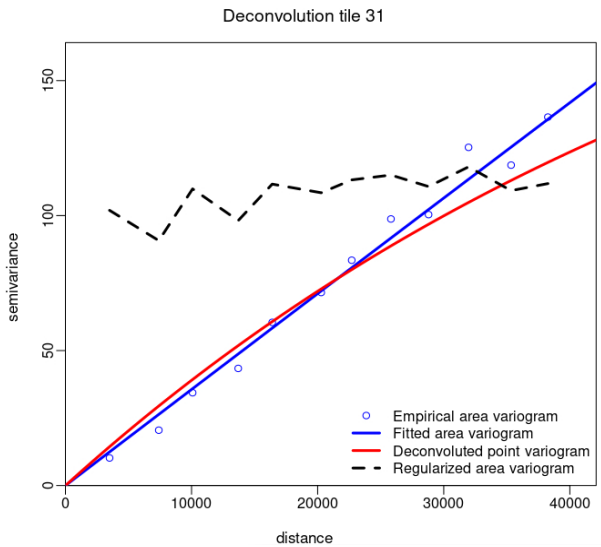

September 2018

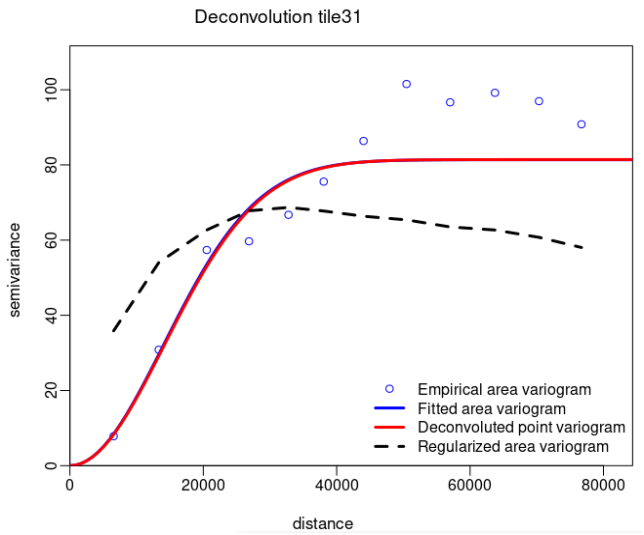

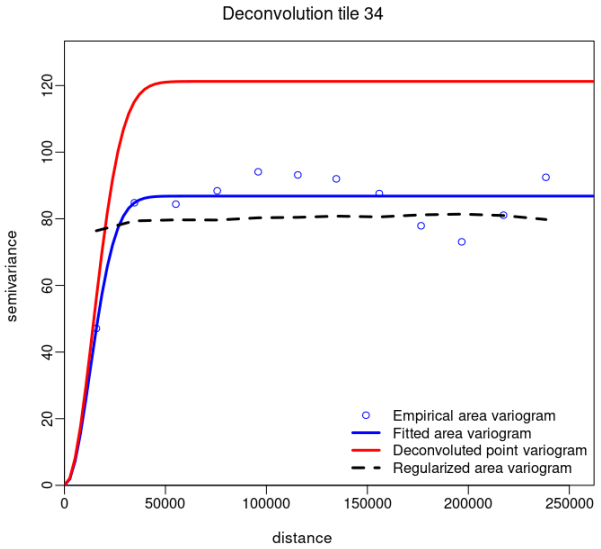

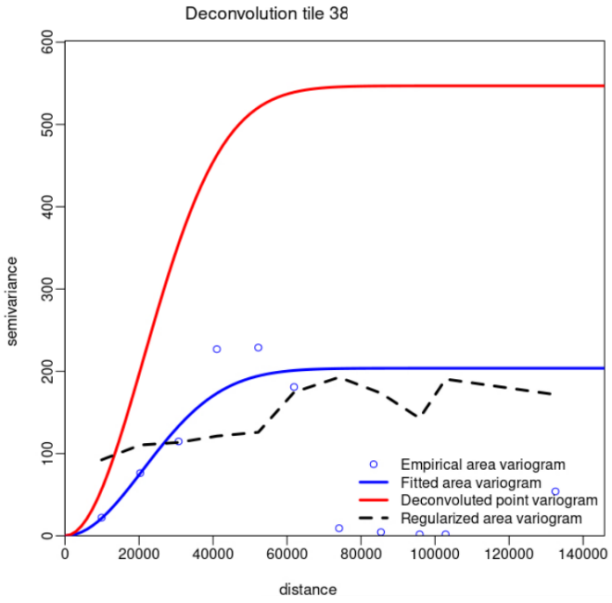

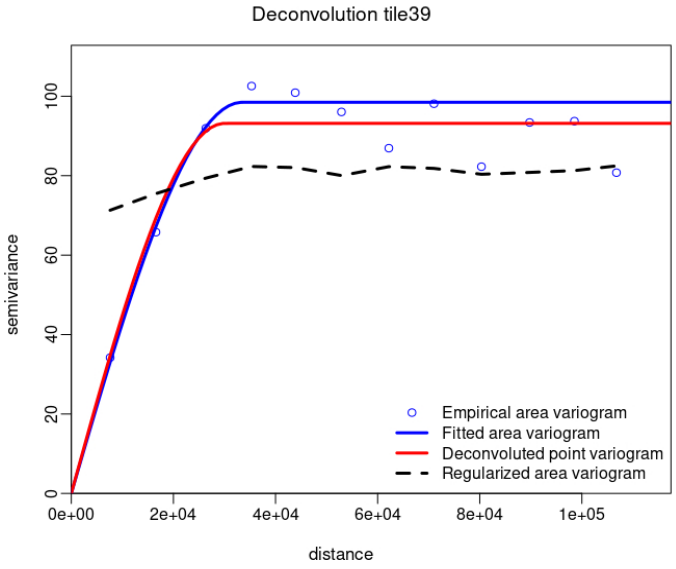

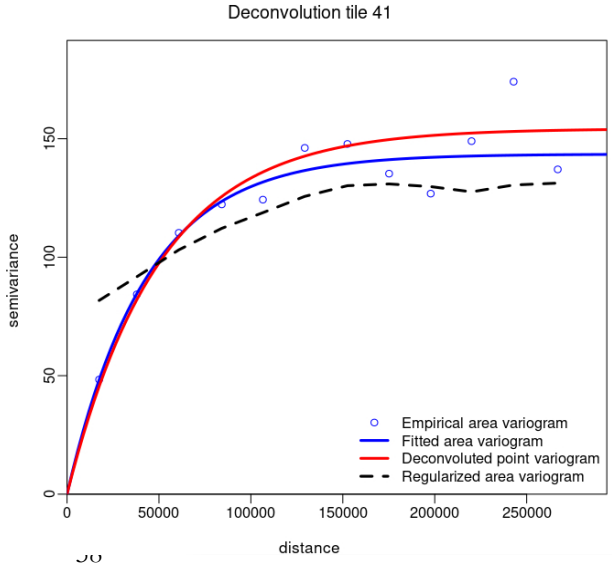

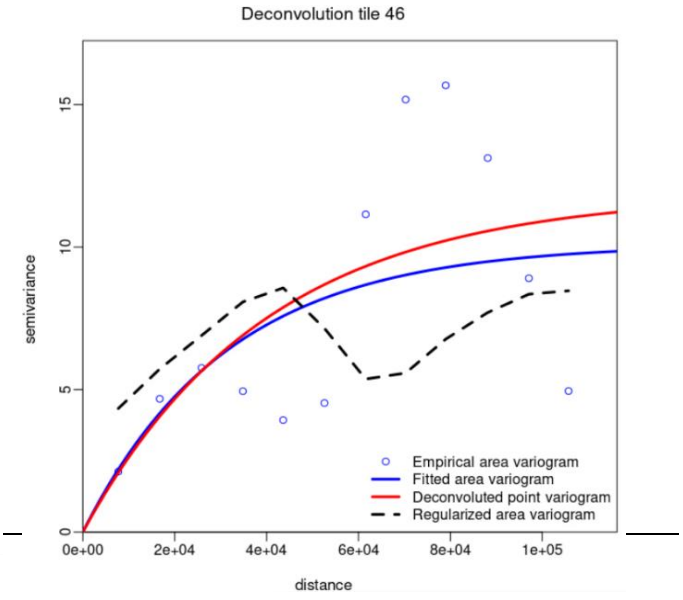

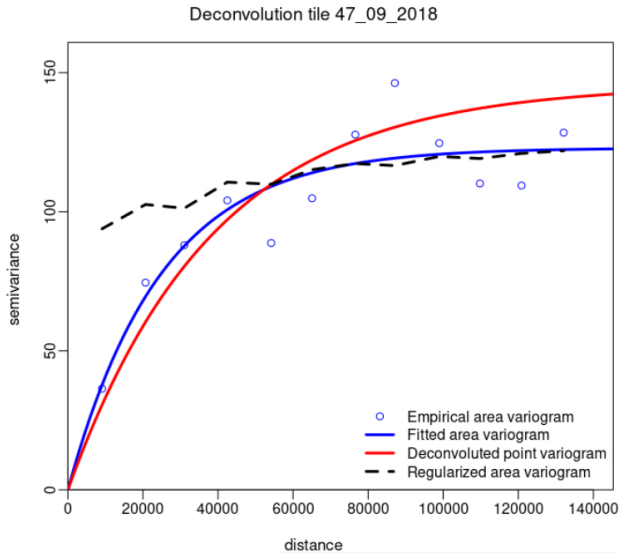
Deconvolution tile 47_09_2018
semivariance
distance
0
50
100
150
0
20000
40000
60000
80000
100000
120000
140000
Empirical area variogram
Fitted area variogram
Deconvoluted point variogram
Regularized area variogram

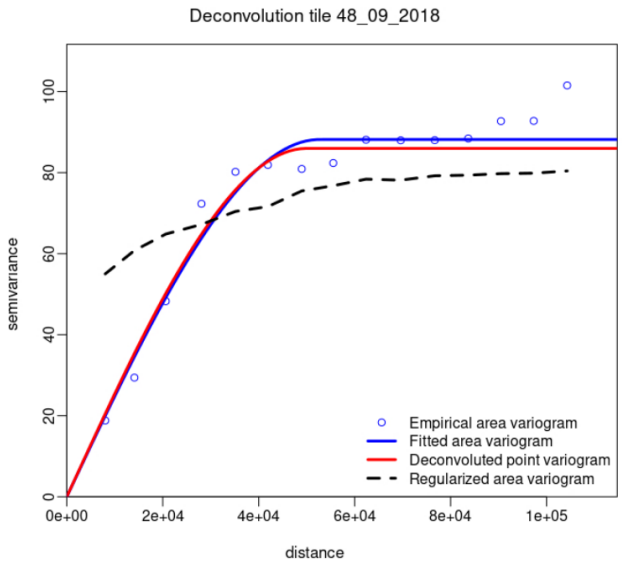
Deconvolution tile 48_09_2018
semivariance
distance
0
20
40
60
80
100
0e+00
2e+04
4e+04
6e+04
8e+04
1e+05
Empirical area variogram
Fitted area variogram
Deconvoluted point variogram
Regularized area variogram

April 2019

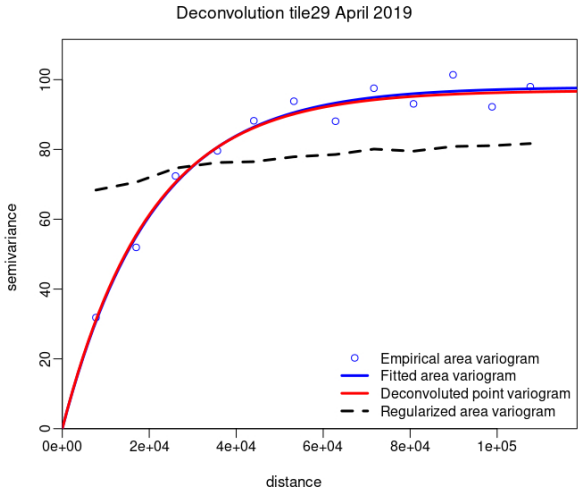
Deconvolution tile29 April 2019
semivariance
distance
Empirical area variogram
Fitted area variogram
Deconvoluted point variogram
Regularized area variogram

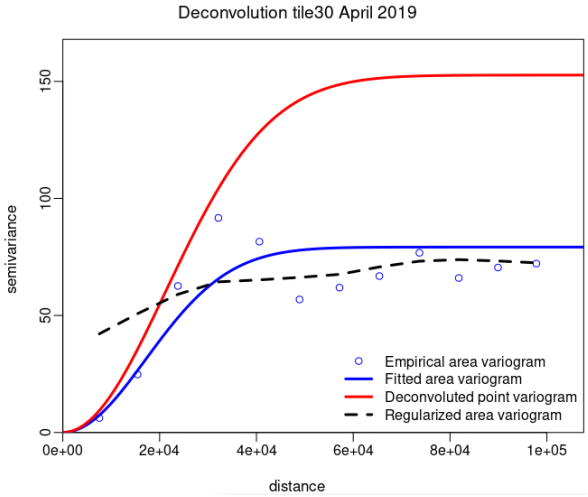
Deconvolution tile30 April 2019
semivariance
distance
Empirical area variogram
Fitted area variogram
Deconvoluted point variogram
Regularized area variogram

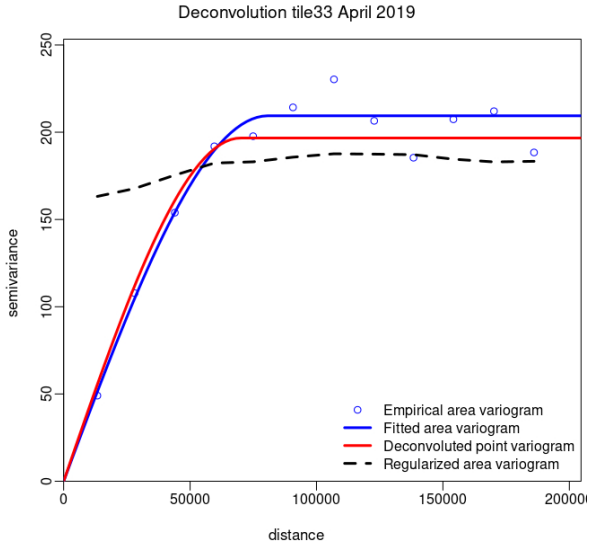
Deconvolution tile33 April 2019
semivariance
distance
Empirical area variogram
Fitted area variogram
Deconvoluted point variogram
Regularized area variogram

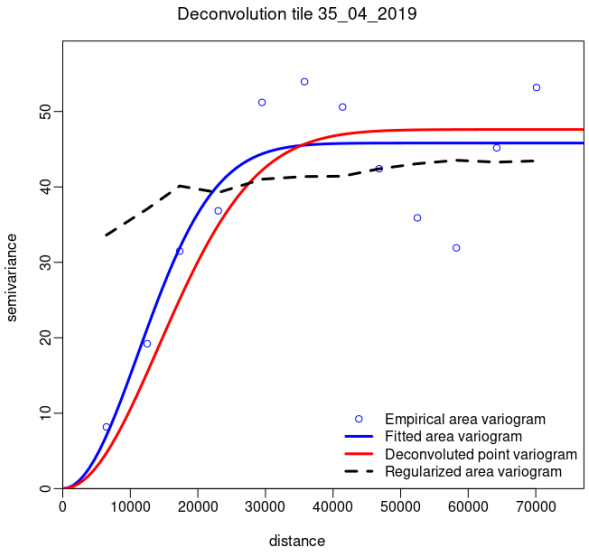
Deconvolution tile 35_04_2019
semivariance
distance
Empirical area variogram
Fitted area variogram
Deconvoluted point variogram
Regularized area variogram

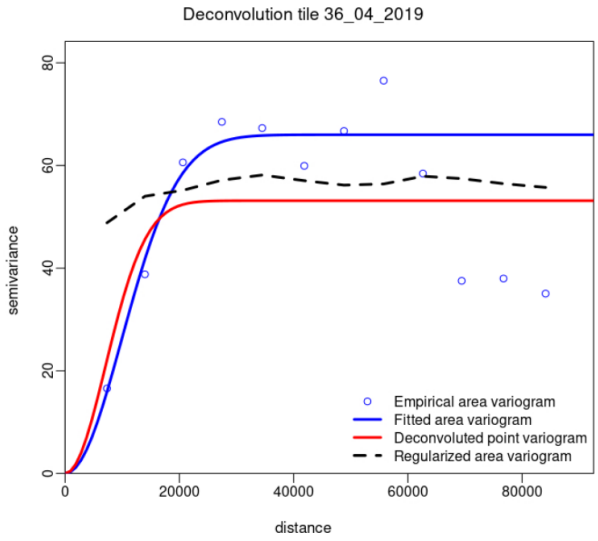
Deconvolution tile 36_04_2019
semivariance
distance
Empirical area variogram
Fitted area variogram
Deconvoluted point variogram
Regularized area variogram

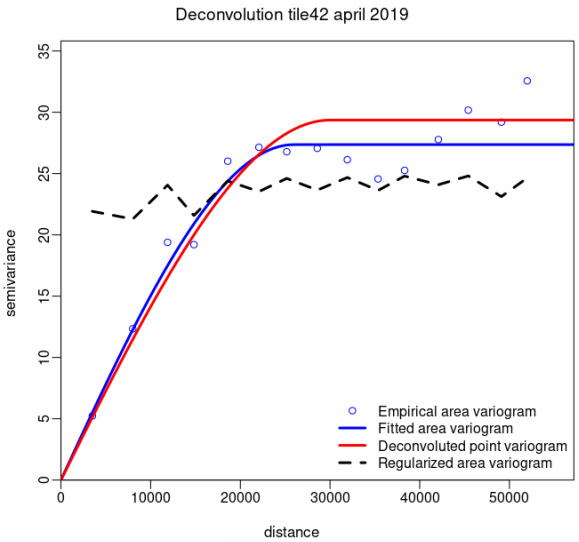
Deconvolution tile42 april 2019
semivariance
distance
Empirical area variogram
Fitted area variogram
Deconvoluted point variogram
Regularized area variogram

May 2019

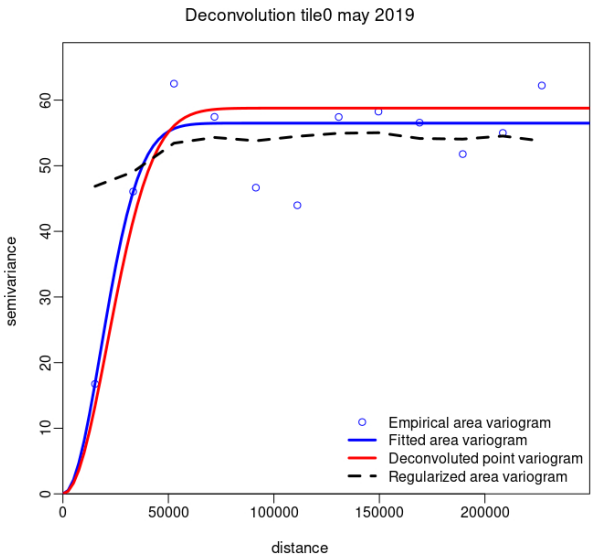
Deconvolution tile0 may 2019
semivariance
distance
0
10
20
30
40
50
60
0
50000
100000
150000
200000
Empirical area variogram
Fitted area variogram
Deconvoluted point variogram
Regularized area variogram

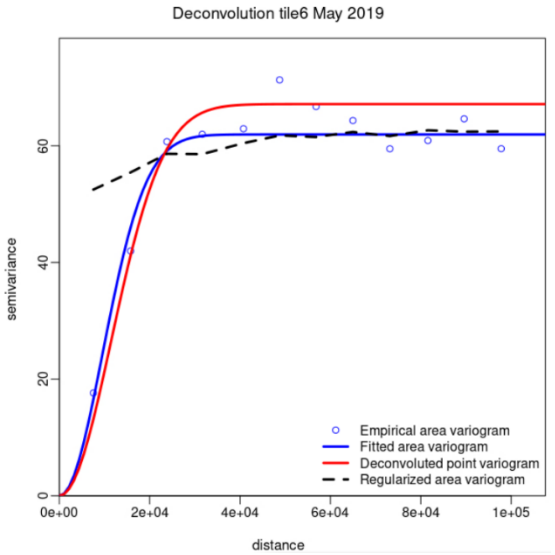
Deconvolution tile6 May 2019
semivariance
distance
0
20
40
60
0e+00
2e+04
4e+04
6e+04
8e+04
1e+05
Empirical area variogram
Fitted area variogram
Deconvoluted point variogram
Regularized area variogram

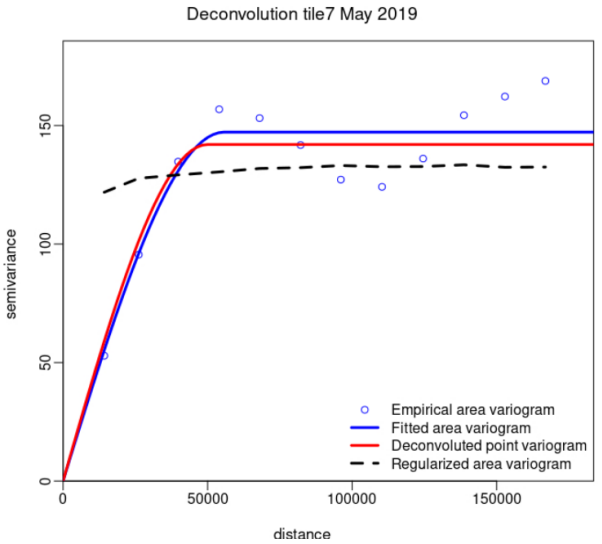
Deconvolution tile7 May 2019
semivariance
distance
0
50
100
150
0
50000
100000
150000
Empirical area variogram
Fitted area variogram
Deconvoluted point variogram
Regularized area variogram

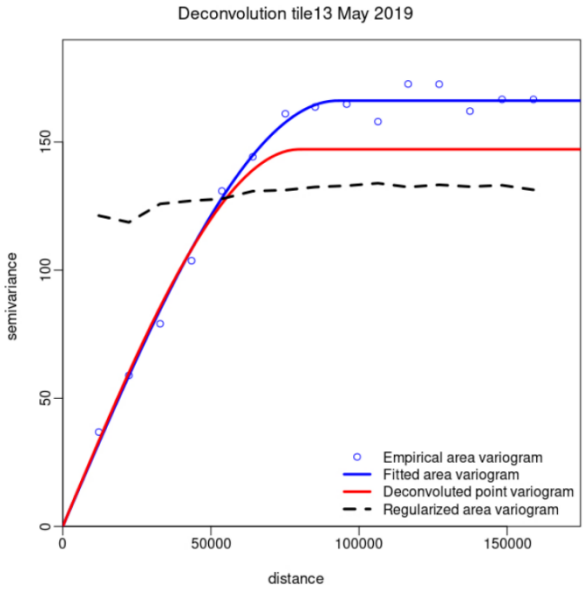
Deconvolution tile13 May 2019
semivariance
distance
0
50
100
150
0
50000
100000
150000
Empirical area variogram
Fitted area variogram
Deconvoluted point variogram
Regularized area variogram

August 2019

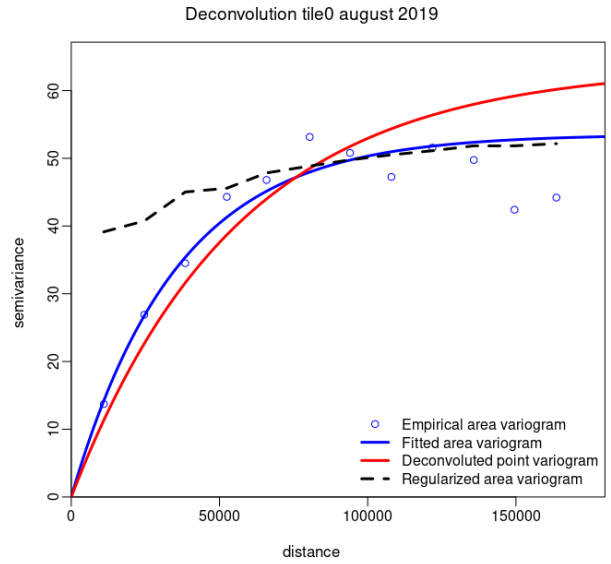
Deconvolution tile0 august 2019
semivariance
distance
Empirical area variogram
Fitted area variogram
Deconvoluted point variogram
Regularized area variogram

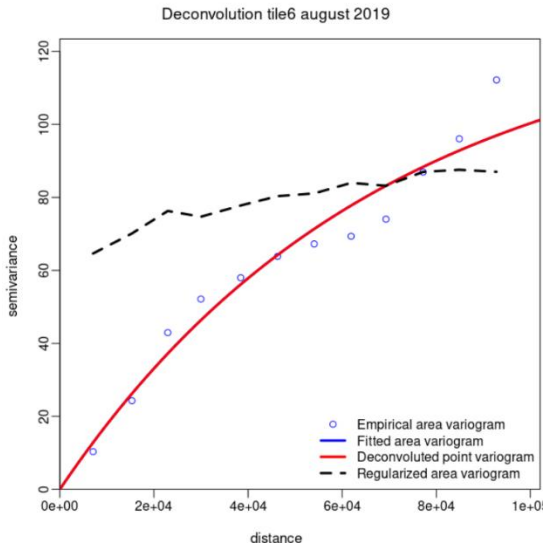
Deconvolution tile6 august 2019
semivariance
distance
Empirical area variogram
Fitted area variogram
Deconvoluted point variogram
Regularized area variogram

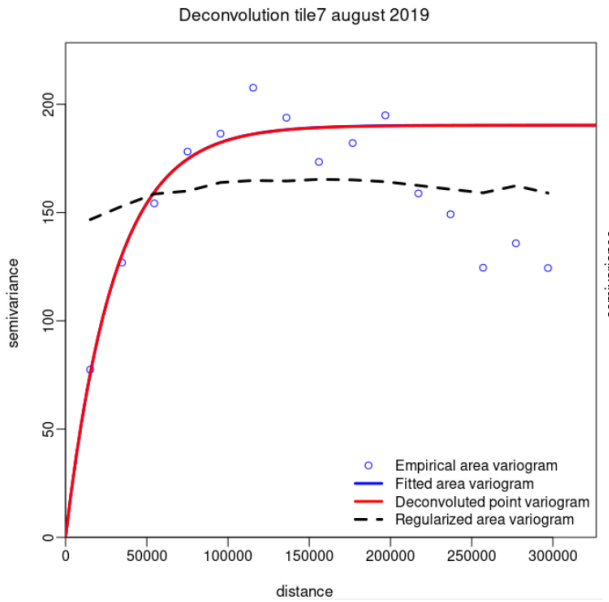
Deconvolution tile7 august 2019
semivariance
distance
Empirical area variogram
Fitted area variogram
Deconvoluted point variogram
Regularized area variogram

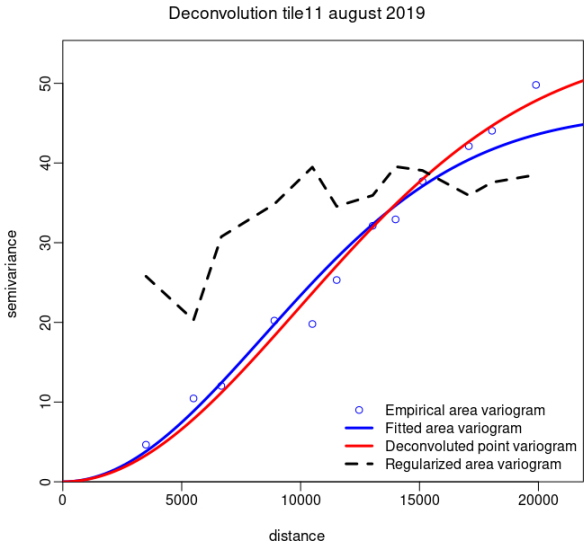
Deconvolution tile11 august 2019
semivariance
distance
Empirical area variogram
Fitted area variogram
Deconvoluted point variogram
Regularized area variogram

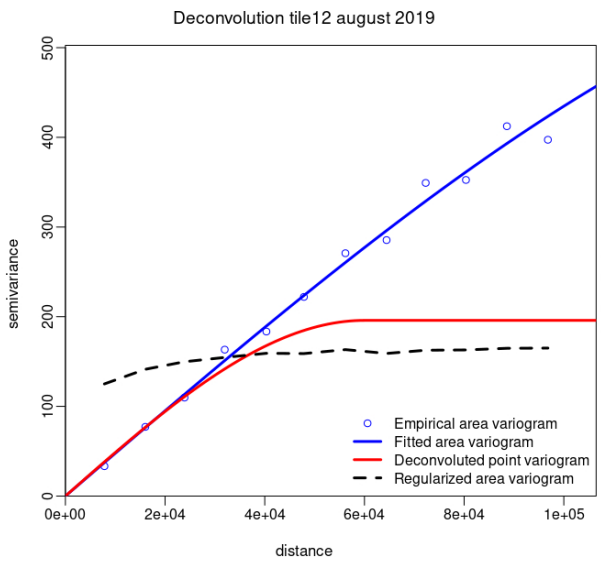
Deconvolution tile12 august 2019
semivariance
distance
Empirical area variogram
Fitted area variogram
Deconvoluted point variogram
Regularized area variogram

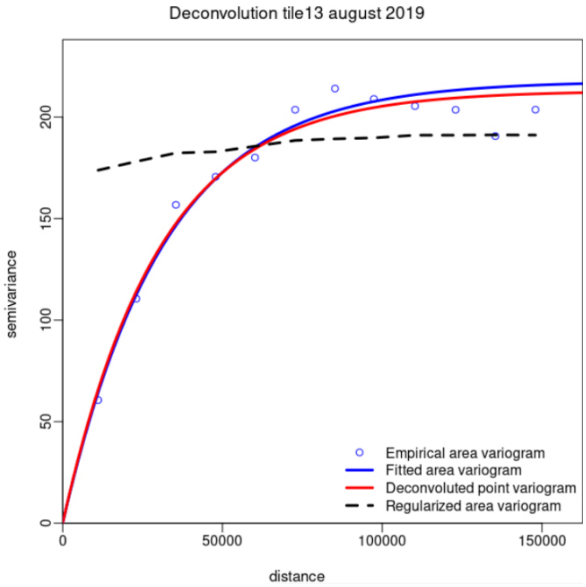
Deconvolution tile13 august 2019
semivariance
distance
Empirical area variogram
Fitted area variogram
Deconvoluted point variogram
Regularized area variogram

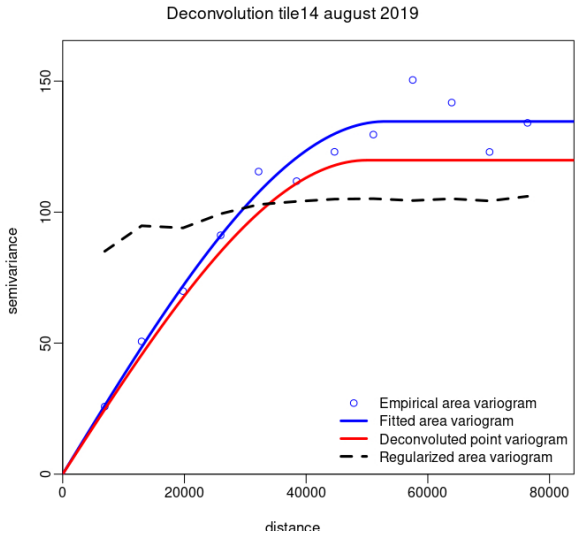
Deconvolution tile14 august 2019
semivariance
distance
Empirical area variogram
Fitted area variogram
Deconvoluted point variogram
Regularized area variogram

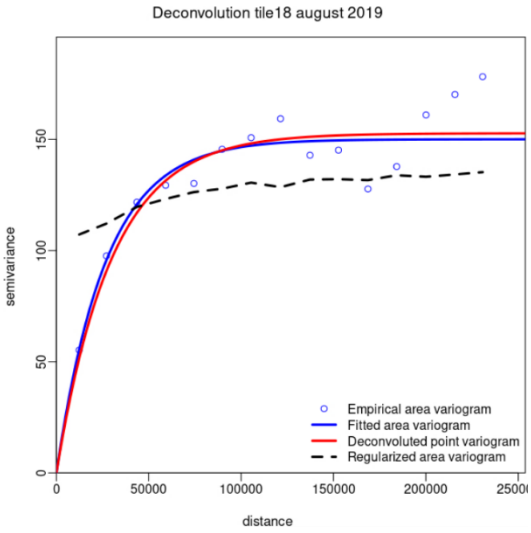
Deconvolution tile18 august 2019
semivariance
distance
Empirical area variogram
Fitted area variogram
Deconvoluted point variogram
Regularized area variogram

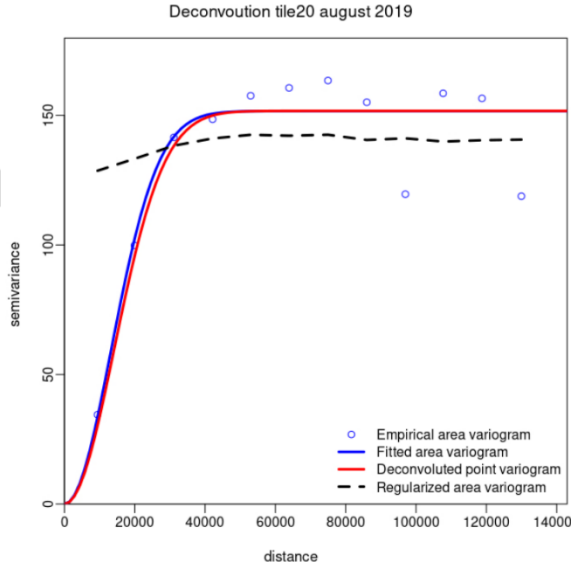
Deconvoution tile20 august 2019
semivariance
distance
Empirical area variogram
Fitted area variogram
Deconvoluted point variogram
Regularized area variogram

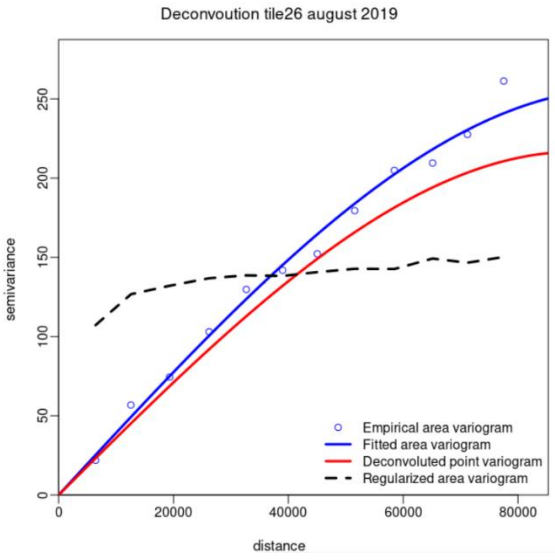
Deconvoution tile26 august 2019
semivariance
distance
Empirical area variogram
Fitted area variogram
Deconvoluted point variogram
Regularized area variogram

May 2020

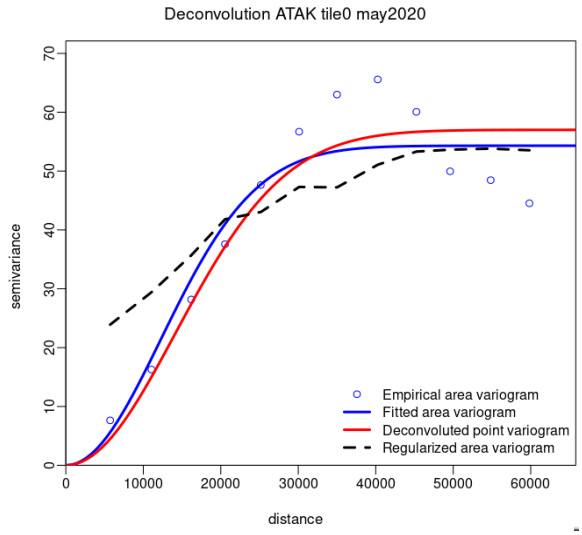
Deconvolution ATAK tile0 may2020
semivariance
distance
Empirical area variogram
Fitted area variogram
Deconvoluted point variogram
Regularized area variogram

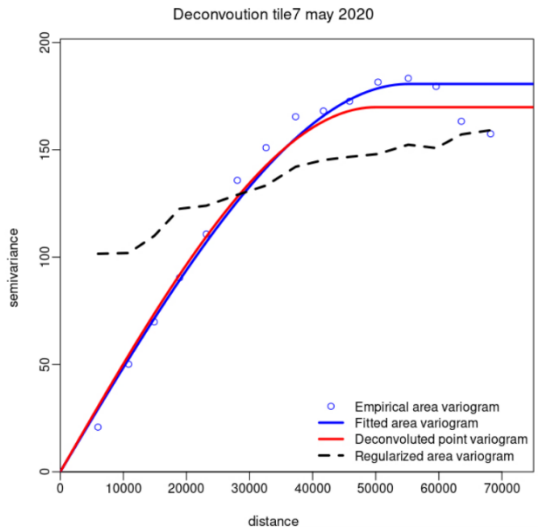
Deconvoution tile7 may 2020
semivariance
distance
Empirical area variogram
Fitted area variogram
Deconvoluted point variogram
Regularized area variogram

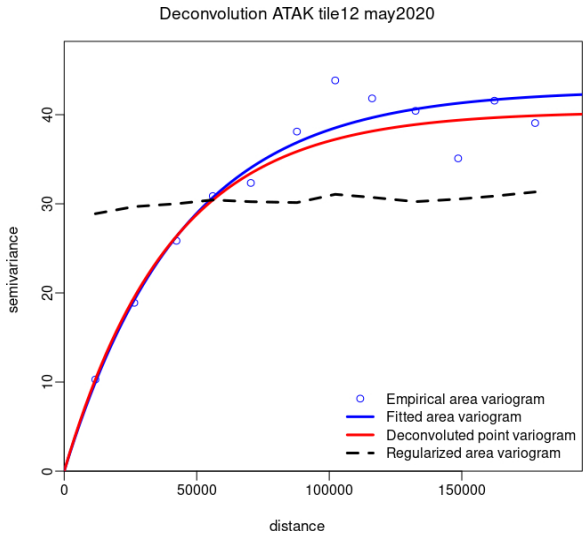
Deconvolution ATAK tile12 may2020
semivariance
distance
Empirical area variogram
Fitted area variogram
Deconvoluted point variogram
Regularized area variogram

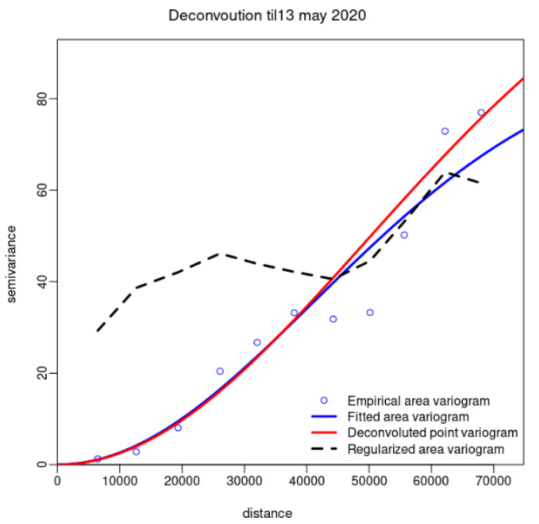
Deconvoution til13 may 2020
semivariance
distance
Empirical area variogram
Fitted area variogram
Deconvoluted point variogram
Regularized area variogram

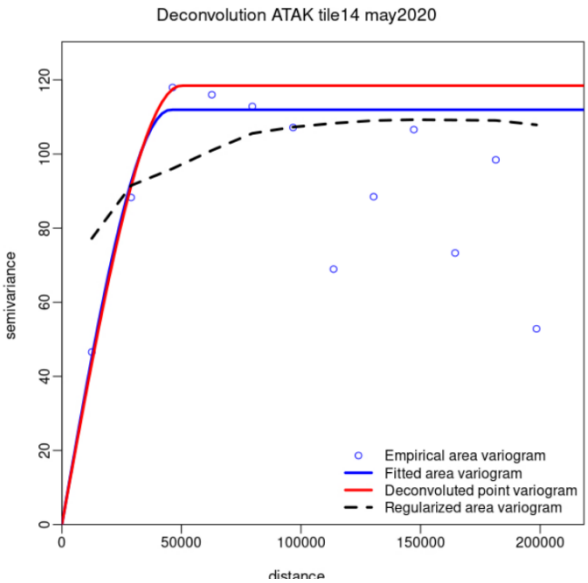
Deconvolution ATAK tile14 may2020
semivariance
distance
Empirical area variogram
Fitted area variogram
Deconvoluted point variogram
Regularized area variogram

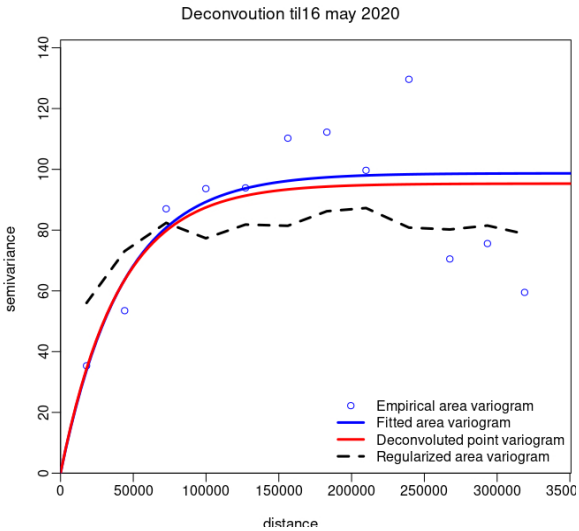
Deconvoution til16 may 2020
semivariance
distance
Empirical area variogram
Fitted area variogram
Deconvoluted point variogram
Regularized area variogram

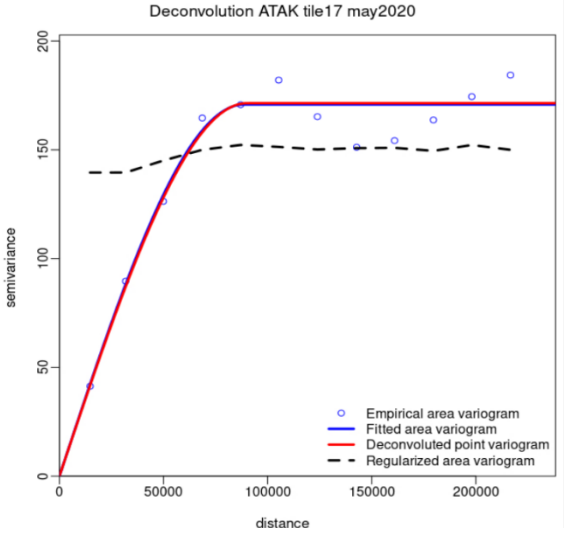
Deconvolution ATAK tile17 may2020
semivariance
distance
Empirical area variogram
Fitted area variogram
Deconvoluted point variogram
Regularized area variogram

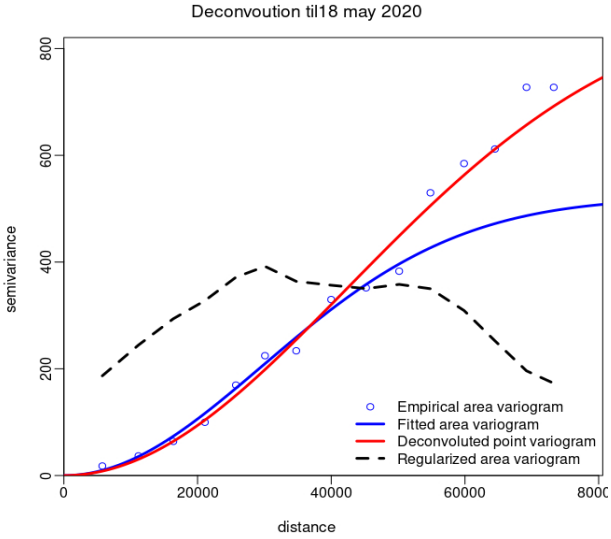
Deconvoution til18 may 2020
semivariance
distance
Empirical area variogram
Fitted area variogram
Deconvoluted point variogram
Regularized area variogram

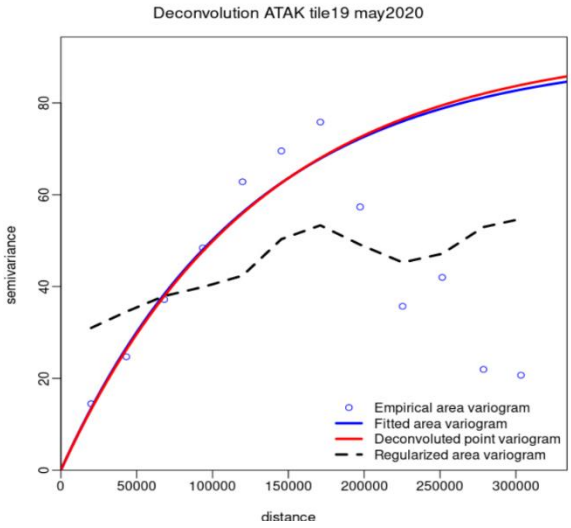
Deconvolution ATAK tile19 may2020
semivariance
distance
Empirical area variogram
Fitted area variogram
Deconvoluted point variogram
Regularized area variogram

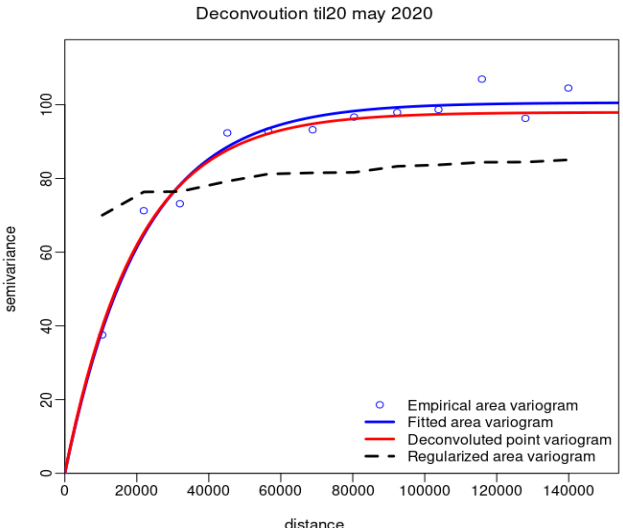
Deconvoution til20 may 2020
semivariance
distance
Empirical area variogram
Fitted area variogram
Deconvoluted point variogram
Regularized area variogram

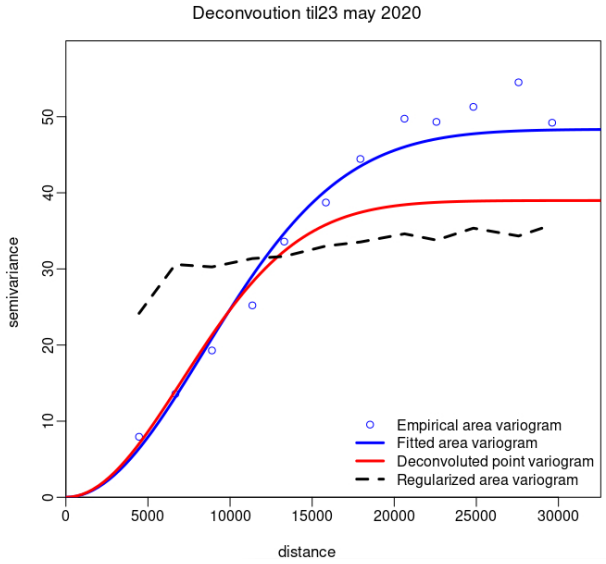
Deconvoution til23 may 2020
semivariance
distance
Empirical area variogram
Fitted area variogram
Deconvoluted point variogram
Regularized area variogram

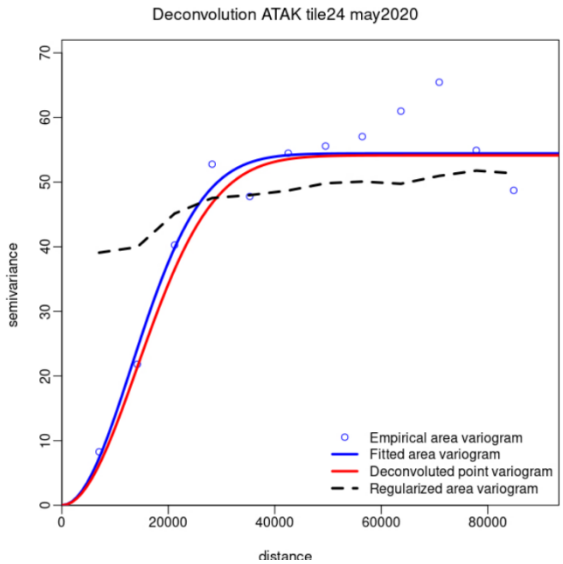
Deconvolution ATAK tile24 may2020
semivariance
distance
Empirical area variogram
Fitted area variogram
Deconvoluted point variogram
Regularized area variogram

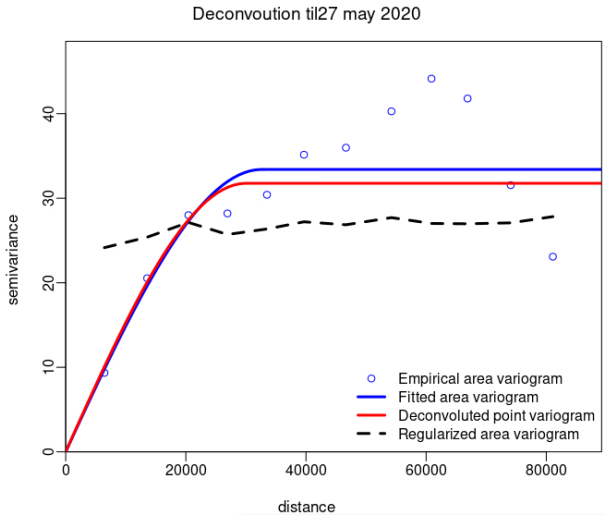
Deconvoution til27 may 2020
semivariance
distance
0
10
20
30
40
0
20000
40000
60000
80000
Empirical area variogram
Fitted area variogram
Deconvoluted point variogram
Regularized area variogram

March 2021

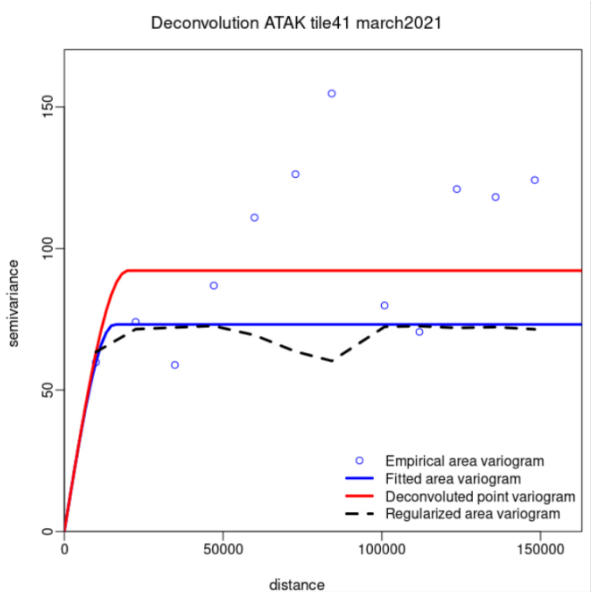
Deconvolution ATAK tile41 march2021
semivariance
distance
0
50
100
150
0
50000
100000
150000
Empirical area variogram
Fitted area variogram
Deconvoluted point variogram
Regularized area variogram

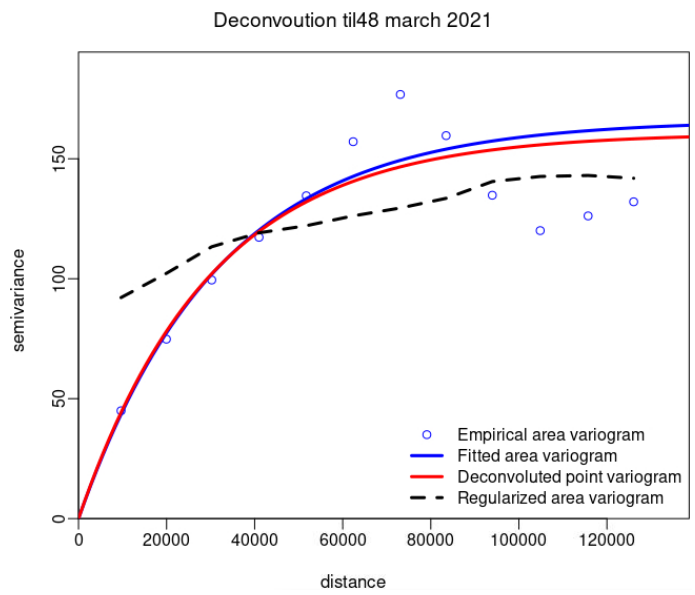
Deconvoution til48 march 2021
semivariance
distance
0
50
100
150
0
20000
40000
60000
80000
100000
120000
Empirical area variogram
Fitted area variogram
Deconvoluted point variogram
Regularized area variogram

May 2021

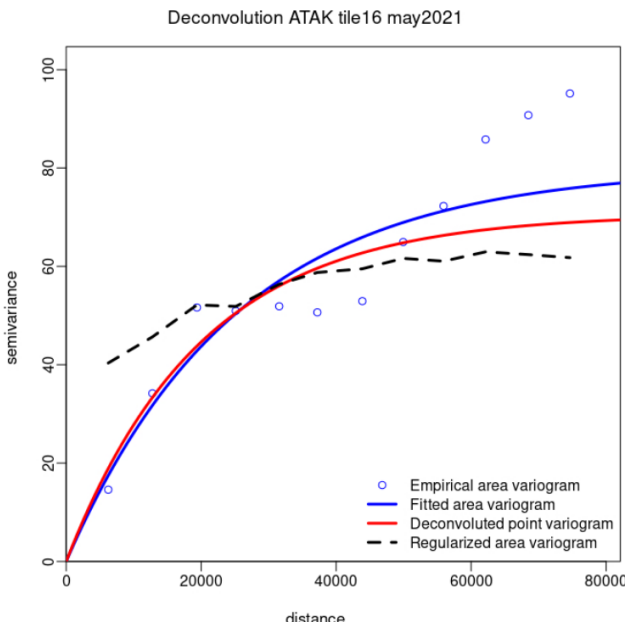
Deconvolution ATAK tile16 may2021
semivariance
distance
0
20
40
60
80
100
0
20000
40000
60000
80000
Empirical area variogram
Fitted area variogram
Deconvoluted point variogram
Regularized area variogram

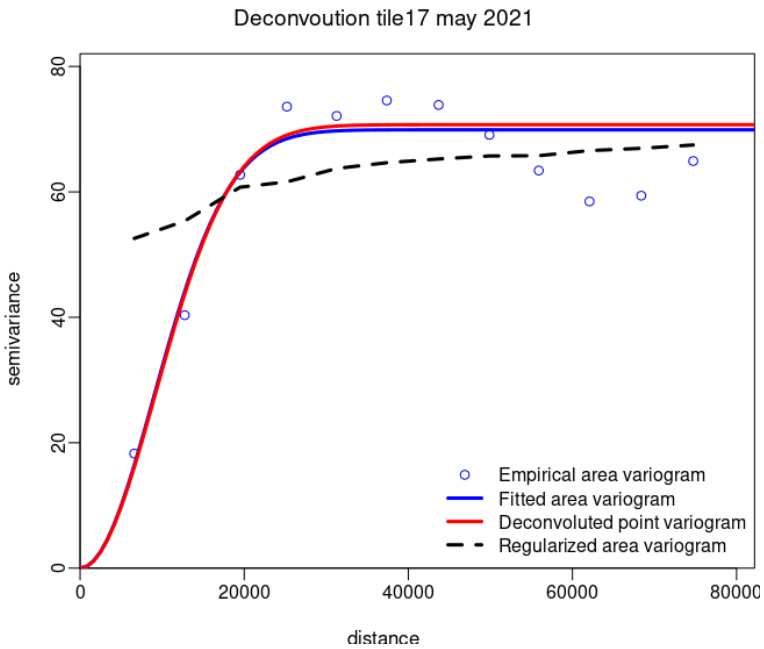
Deconvoution tile17 may 2021
semivariance
distance
0
20
40
60
80
0
20000
40000
60000
80000
Empirical area variogram
Fitted area variogram
Deconvoluted point variogram
Regularized area variogram

Appendix 3. Tile-wise model parameters from August 2018-May 2021.

Date	Tile number	Psill	Model	Range(m)
Aug-18	16	162	Sph	30000
Aug-18	17	198	Sph	40000
Aug-18	19	97	Sph	40000
Aug-18	20	64	Gau	30000
Aug-18	21	94	Sph	40000
Aug-18	27	93	Gau	20000
Aug-18	31	183	Exp	40000
Aug-18	39	-	-	-

Date	Tile number	Psill	Model	Range(m)
Sep-18	31	81	Gau	20000
Sep-18	34	88	Gau	20000
Sep-18	38	205	Gau	30000
Sep-18	39	93	Sph	30000
Sep-18	41	154	Gau	50000
Sep-18	46	11	Exp	40000
Sep-18	47	145	Exp	38669
Sep-18	48	85	Sph	50000

Date	Tile number	Psill	Model	Range(m)
Apr-19	22	-	-	-
Apr-19	26	-	-	-
Apr-19	29	96	Exp	20000
Apr-19	30	84	Gau	30000
Apr-19	33	196	Gau	70000
Apr-19	35	47	Gau	20000
Apr-19	36	53	Gau	10000
Apr-19	38	-	-	-
Apr-19	42	29	Sph	30000

Date	Tile number	Psill	Model	Range(m)
May-19	0	58	Gau	30000
May-19	6	67	Gau	16185
May-19	7	142	Gau	50000
May-19	13	147	Sph	80000
May-19	20	-	-	-

Date	Tile number	Psill	Model	Range(m)
Aug-19	0	63	Exp	55942
Aug-19	6	130	Exp	68373
Aug-19	7	190	Exp	30000
Aug-19	11	55	Gau	14000
Aug-19	12	195	Sph	60000
Aug-19	13	212	Exp	30000
Aug-19	14	119	Sph	50000
Aug-19	18	150	Exp	30000
Aug-19	20	151	Gau	20000
Aug-19	26	216	Sph	90000

Date	Tile number	Psill	Model	Range(m)
May-20	0	57	Gau	20000
May-20	7	169	Sph	50000
May-20	11	-	-	-
May-20	12	40	Exp	40000
May-20	13	124	Gau	70000
May-20	14	118	Sph	50000
May-20	16	95	Exp	40000
May-20	17	171	Sph	90000
May-20	18	892	Gau	60000
May-20	19	92	Exp	130000
May-20	20	97	Exp	20000
May-20	23	38	Gau	10000
May-20	24	54	Gau	20000
May-20	26	-	-	-
May-20	27	31	Sph	30000
May-20	48	17760	Exp	9178263

Date	Tile number	Psill	Model	Range(m)
Mar-21	14	-	-	-
Mar-21	32	-	-	-
Mar-21	41	92	Sph	20000
Mar-21	48	160	Exp	30000

Date	Tile number	Psill	Model	Range(m)
May-21	16	70	Exp	20000
May-21	17	70	Gau	13000
May-21	46	-	-	-

Appendix 4. Cross-validation results for all tiles from August 2018 to May 2021

Date	Tile number	Psill	Model	Range(m)	MAE	CC	CH
Aug-18	16	162	Sph	30000	0.03971464	0.9987267	0.99455
Aug-18	17	198	Sph	40000	0.1265589	0.9994586	0.996565
Aug-18	19	97	Sph	40000	0.1101574	0.9990011	0.998057
Aug-18	20	64	Gau	30000	264.1889	0.9386484	0.265431
Aug-18	21	94	Sph	40000	0.09121189	0.9992243	0.994278
Aug-18	27	93	Gau	20000	4.237769	0.972898	0.435715
Aug-18	31	183	Exp	40000	0.0747412	0.999317	0.995163
Aug-18	39	-	-	-	-	-	-

Date	Tile number	Psill	Model	Range(m)	MAE	CC	CH
Sep-18	31	81	Gau	20000	0.9269885	0.3471841	-0.103939
Sep-18	34	88	Gau	20000	0.9671294	15.01897	0.897518
Sep-18	38	205	Gau	30000	537.2752	0.9943598	0.0953
Sep-18	39	93	Sph	30000	0.05973491	0.999097	0.995597
Sep-18	41	154	Gau	50000	0.1309583	0.9986601	0.997803
Sep-18	46	11	Exp	40000	0.02588903	0.9994414	0.999179
Sep-18	47	145	Exp	38669	0.1207372	0.9993138	0.997605
Sep-18	48	85	Sph	50000	0.112249	0.9993028	0.997236

Date	Tile number	Psill	Model	Range(m)	MAE	CC	CH
Apr-19	22	-	-	-	-	-	-
Apr-19	26	-	-	-	-	-	-
Apr-19	29	96	Exp	20000	0.1086391	0.9993747	0.991917
Apr-19	30	84	Gau	30000	9.611836	0.9570809	0.359847
Apr-19	33	196	Gau	70000	0.1481458	0.9993117	0.99677
Apr-19	35	47	Gau	20000	55.86762	0.995594	0.068474
Apr-19	36	53	Gau	10000	0.07983068	0.9924553	0.988989
Apr-19	38	-	-	-	-	-	-
Apr-19	42	29	Sph	30000	0.04126563	0.999333	0.992849

Date	Tile number	Psill	Model	Range(m)	MAE	CC	CH
May-19	0	58	Gau	30000	812.1985	0.9592446	-0.013372
May-19	6	67	Gau	16185	2.251728	0.9411016	0.611802
May-19	7	142	Gau	50000	0.1018653	0.9996394	0.996362
May-19	13	147	Sph	80000	0.09993175	0.999476	0.996764
May-19	20	-	-	-	-	-	-

Date	Tile number	Psill	Model	Range(m)	MAE	CC	CH
Aug-19	0	63	Exp	55942	0.07154534	0.9992935	0.998478
Aug-19	6	130	Exp	68373	0.06743898	0.9992989	0.996823
Aug-19	7	190	Exp	30000	0.1381628	0.9993879	0.997451
Aug-19	11	55	Gau	14000	0.9445475	0.9966731	0.984168
Aug-19	12	195	Sph	60000	0.09754664	0.9995642	0.998271
Aug-19	13	212	Exp	30000	0.1267444	0.9996429	0.997096
Aug-19	14	119	Sph	50000	0.06734281	0.9993009	0.998306
Aug-19	18	150	Exp	30000	0.110598	0.9991279	0.998189
Aug-19	20	151	Gau	20000	0.7251088	0.9842682	0.997315
Aug-19	26	216	Sph	90000	0.05764895	0.9996373	0.998624

Date	Tile number	Psill	Model	Range(m)	MAE	CC	CH
May-20	0	57	Gau	20000	188.8907000	0.9840368	0.9684758
May-20	7	169	Sph	50000	0.1435454	0.99814	0.9979729
May-20	11	-	-	-	-	-	-
May-20	12	40	Exp	40000	0.0344106	0.9995306	0.9972030
May-20	13	124	Gau	70000	1872.2390000	0.9905920	0.7830096
May-20	14	118	Sph	50000	0.0922951	0.9994461	0.9975481
May-20	16	95	Exp	40000	0.0609052	0.9988289	0.9992167
May-20	17	171	Sph	90000	0.1264647	0.9991068	0.9975914
May-20	18	892	Gau	60000	7911.9220000	0.9946848	0.8456572
May-20	19	92	Exp	130000	0.0411845	0.9992569	0.9978939
May-20	20	97	Exp	20000	0.0721603	0.9994404	0.9985475
May-20	23	38	Gau	10000	0.0543925	0.9906254	0.9930827
May-20	24	54	Gau	20000			0.9963973
May-20	26	-	-	-	-	-	-
May-20	27	31	Sph	30000	0.0299209	0.9992492	0.9965433
May-20	48	17760	Exp	9178263	0.0228196	0.9995208	0.9974496

Date	Tile number	Psill	Model	Range(m)	MAE	CC	CH
Mar-21	14	-	-	-	-	-	-
Mar-21	32	-	-	-	-	-	-
Mar-21	41	92	Sph	20000	0.03317563	0.9995346	0.993957
Mar-21	48	160	Exp	30000	0.1249264	0.9975884	0.997114

Date	Tile number	Psill	Model	Range(m)	MAE	CC	CH
May-21	16	70	Exp	20000	0.08962578	0.9987971	0.995576
May-21	17	70	Gau	13000	0.8377056	0.99551534	0.995131
May-21	46	-	-	-	-	-	-

Appendix 5. Rejected tiles for the month and year April 2019, May 2019, August 2019, May 2020.